STATE OF THE CLIMATE IN 2025

THE ARCTIC

T. A. Moon, M. L. Druckenmiller, and R. L. Thoman, Eds.

Special Online Supplement to the *Bulletin of the American Meteorological Society* Vol. 107, No. 8, August, 2026

https://doi.org/10.1175/BAMS-D-26-0123.1

Corresponding author: Twila A. Moon / Twila.Moon@colorado.edu

STATE OF THE CLIMATE IN 2025
The Arctic

Editors

Jessica Blunden
James Reagan

Chapter Editors

Anthony Arguez
Josh Blannin
Peter Bissolli
Kyle R. Clem
Howard J. Diamond
Matthew L. Druckenmiller
Robert J. H. Dunn
Catherine Ganter
Nadine Gobron
Rodney Martinez
Twila A. Moon
Gary A. Morris
Marilyn N. Raphael
Renellys C. Perez
Carl J. Schreck III
Zewdu Segele
Laura Stevens
Richard L. Thoman
Denis L. Volkov
Zhiwei Zhu

Technical Editors

Lukas Noguchi
Laura Ohlmann

BAMS Special Editor for Climate

Timothy DelSole

American Meteorological Society

Cover Credit:
Icebergs from the Greenland Ice Sheet shoal on the glacial outwash beach at Sermilik Station, on Ammassalik Island in East Greenland on 18 June 2025. Photo credit: Kristin Poinar

How to cite this document:
The Arctic is one chapter from the *State of the Climate in 2025* annual report and is available from https://doi.org/10.1175/BAMS-D-26-0123.1. Compiled by NOAA's National Centers for Environmental Information, *State of the Climate in 2025* is based on contributions from scientists from around the world. It provides a detailed update on global climate indicators, notable weather events, and other data collected by environmental monitoring stations and instruments located on land, water, ice, and in space. The full report is available from https://doi.org/10.1175/2026BAMSStateoftheClimate.1.

Citing the complete report:
Blunden, J. and J. Reagan, Eds., 2026: "State of the Climate in 2025". Bull. Amer. Meteor. Soc., 107 (8), Si–S512, https://doi.org/10.1175/2026BAMSStateoftheClimate.1.

Citing this chapter:
Moon, T. A., M. L. Druckenmiller, and R. L. Thoman, Eds., 2026: The Arctic [in "State of the Climate in 2025"]. Bull. Amer. Meteor. Soc., 107 (8), S296–S346, https://doi.org/10.1175/BAMS-D-26-0123.1.

Citing a section (example):
Ballinger, T. J., A. Crawford, A. H. Butler, M. C. Serreze, S. Bigalke, J. E. Walsh, B. Brettschneider, R. L. Thoman, U. S. Bhatt, E. Hanna, H. Motrøen Gjelten, S.-J. Kim, J. E. Overland, and M. Wang, 2026: Surface air temperature [in "State of the Climate in 2025"]. Bull. Amer. Meteor. Soc., 107 (8), S307–S309, https://doi.org/10.1175/BAMS-D-26-0123.1.

Editor and Author Affiliations (alphabetical by name)

Andreassen, Liss Marie, Section for Glaciers, Ice and Snow, Norwegian Water Resources and Energy Directorate, Oslo, Norway

Askjaer, Thomas G., Danish Meteorological Institute, Copenhagen, Denmark

Ballinger, Thomas J., International Arctic Research Center, University of Alaska Fairbanks, Fairbanks, Alaska

Berner, Logan T., School of Informatics, Computing, and Cyber Systems, Northern Arizona University, Flagstaff, Arizona

Bernhard, Germar H., Biospherical Instruments Inc., San Diego, California

Bhatt, Uma S., Geophysical Institute, University of Alaska Fairbanks, Fairbanks, Alaska

Bigalke, Siiri, Department of Geography, Portland State University, Portland, Oregon

Bjerke, Jarle W., FRAM – High North Research Centre for Climate and the Environment, Tromsø, Norway; Norwegian Institute for Nature Research, Trondheim, Norway

Bliss, Angela, NASA Goddard Space Flight Center, Greenbelt, Maryland

Box, Jason E., Geological Survey of Denmark and Greenland (GEUS), Copenhagen, Denmark

Brettschneider, Brian, NOAA/NWS Alaska Region, Anchorage, Alaska

Burgess, D., Geological Survey of Canada, Ottawa, Ontario, Canada

Butler, Amy H., NOAA Chemical Sciences Laboratory, Boulder, Colorado

Christiansen, Hanne H., University of the Arctic, Aarhus University, Aarhus, Denmark

Crawford, Alex, Department of Environment and Geography, University of Manitoba, Winnipeg, Manitoba, Canada

Decharme, Bertrand, Centre National de Recherches Météorologiques, Météo-France/CNRS, Toulouse, France

Derksen, Chris, Climate Research Division, Environment and Climate Change Canada, Toronto, Canada

Divine, Dmitry, Norwegian Polar Institute, Fram Centre, Tromsø, Norway

Druckenmiller, Matthew L., National Snow and Ice Data Center, Cooperative Institute for Research in Environmental Sciences, University of Colorado, Boulder, Colorado

Elias Chereque, Aleksandra, Department of Physics, University of Toronto, Toronto, Canada

Epstein, Howard E., Department of Environmental Sciences, University of Virginia, Charlottesville, Virginia

Farrell, Sinead, Department of Geographical Sciences, University of Maryland, College Park, Maryland

Fausto, Robert S., Geological Survey of Denmark and Greenland (GEUS), Copenhagen, Denmark

Fettweis, Xavier, SPHERES Research Unit, University of Liège, Liège, Belgium

Fioletov, Vitali E., Environment and Climate Change Canada, Toronto, Ontario, Canada

Florentine, Caitlyn, U.S. Geological Survey, Northern Rocky Mountain Science Center, Bozeman, Montana

Forbes, Bruce C., Arctic Centre, University of Lapland, Rovaniemi, Finland

Frost, Gerald V. (JJ), Alaska Biological Research, Inc., Fairbanks, Alaska

Gerland, Sebastian, Norwegian Polar Institute, Fram Centre, Tromsø, Norway

Grooß, Jens-Uwe, Forschungszentrum Jülich (ICE-4), Jülich, Germany

Hanna, Edward, Department of Geography and Lincoln Climate Research Group, Lincoln, United Kingdom

Hendricks, Stefan, Alfred Wegener Institute, Helmholtz Centre for Polar and Marine Research, Bremerhaven, Germany

Ialongo, Iolanda, Finnish Meteorological Institute, Helsinki, Finland

Isaksen, Ketil, Norwegian Meteorological Institute, Oslo, Norway

Jia, Gensuo, Institute of Atmospheric Physics, Chinese Academy of Sciences, Beijing, China

Johnsen, Bjørn, Norwegian Radiation and Nuclear Safety Authority, Østerås, Norway

Kaleschke, Lars, Alfred Wegener Institute, Helmholtz Centre for Polar and Marine Research, Bremerhaven, Germany

Kim, Seong-Joong, Korea Polar Research Institute, Incheon, South Korea

Kohler, J., Norwegian Polar Institute, Fram Centre, Tromsø, Norway

Labe, Zachary M., Climate Central, Princeton, New Jersey

Lader, Rick, International Arctic Research Center, University of Alaska Fairbanks, Fairbanks, Alaska

Lakkala, Kaisa, Finnish Meteorological Institute, Sodankylä, Finland

Lara, Mark J., Department of Plant Biology, University of Illinois, Urbana, Illinois; Department of Geography, University of Illinois, Urbana, Illinois

Lee, Simon H., School of Earth and Environmental Sciences, University of St Andrews, St Andrews, United Kingdom

Loomis, Bryant D., NASA Goddard Space Flight Center, Greenbelt, Maryland

Luks, B., Institute of Geophysics, Polish Academy of Sciences, Warsaw, Poland

Luojus, Kari, Arctic Research Centre, Finnish Meteorological Institute, Helsinki, Finland

López-Blanco, E., Department of Ecoscience, Arctic Research Center, Aarhus University, Roskilde, Denmark

Macander, Matthew J., Alaska Biological Research, Inc., Fairbanks, Alaska

Magnússon, Rúna Í., Plant Ecology and Nature Conservation Group, Wageningen University & Research, Wageningen, The Netherlands

Mankoff, Ken D., Business Integra, New York, New York; NASA Goddard Institute for Space Studies, New York, New York

Medley, Brooke, Cryospheric Sciences Laboratory, NASA Goddard Space Flight Center, Greenbelt, Maryland

Meier, Walter N., National Snow and Ice Data Center, Cooperative Institute for Research in Environmental Sciences, University of Colorado, Boulder, Colorado

Montesano, Paul M., NASA Goddard Space Flight Center, Greenbelt, Maryland

Moon, Twila A., National Snow and Ice Data Center, Cooperative Institute for Research in Environmental Sciences, University of Colorado, Boulder, Colorado

Mote, Thomas L., University of Georgia, Athens, Georgia

Motrøen Gjelten, Herdis, Norwegian Meteorological Institute, Oslo, Norway

Mudryk, Lawrence, Climate Research Division, Environment and Climate Change Canada, Toronto, Canada

Müller, Rolf, Forschungszentrum Jülich (ICE-4), Jülich, Germany

Natali, S. M., Woodwell Climate Research Center, Falmouth, Massachusetts

Neigh, Christopher S. R., NASA Goddard Space Flight Center, Greenbelt, Maryland

Nyland, Kelsey E., George Washington University, Washington, District of Columbia

Orndahl, K. M., School of Informatics, Computing, and Cyber Systems, Northern Arizona University, Flagstaff, Arizona

Overland, James E., NOAA/OAR Pacific Marine Environmental Laboratory, Seattle, Washington

Perovich, Donald K., Dartmouth College, Hanover, New Hampshire

Petty, Alek, NASA Goddard Space Flight Center, Greenbelt, Maryland

Phoenix, Gareth K., School of Biosciences, University of Sheffield, Sheffield, United Kingdom

Poinar, Kristin, University at Buffalo, Buffalo, New York

Pálsson, F., Institute of Earth Sciences, University of Iceland, Reykjavík, Iceland

Ricker, Robert, NORCE Norwegian Research Centre, Tromsø, Norway

Romanovsky, Vladimir E., Geophysical Institute, University of Alaska Fairbanks, Fairbanks, Alaska

Sass, L., U.S. Geological Survey, Alaska Science Center, Anchorage, Alaska

Schuur, E. A. G., Center for Ecosystem Science and Society, Northern Arizona University, Flagstaff, Arizona

Serreze, Mark C., National Snow and Ice Data Center, Cooperative Institute for Research in Environmental Sciences, University of Colorado, Boulder, Colorado

Smith, Benjamin E., Polar Science Center, Applied Physics Laboratory, University of Washington, Seattle, Washington

Editor and Author Affiliations (continued)

Smith, Sharon L., Geological Survey of Canada, Natural Resources Canada, Ottawa, Canada

Streletskiy, Dmitry A., George Washington University, Washington, District of Columbia

Svendby, Tove, The Climate and Environmental Research Institute NILU, Kjeller, Norway

Thoman, Richard L., International Arctic Research Center, University of Alaska Fairbanks, Fairbanks, Alaska

Thomson, L., Queen's University, Kingston, Ontario, Canada

Thorsteinsson, T., Icelandic Meteorological Office, Reykjavík, Iceland

Tian-Kunze, Xiangshan, Alfred Wegener Institute, Helmholtz Centre for Polar and Marine Research, Bremerhaven, Germany

Timmermans, Mary-Louise, Department of Earth and Planetary Sciences, Yale University, New Haven, Connecticut

Tømmervik, Hans, FRAM – High North Research Centre for Climate and the Environment, Tromsø, Norway; Norwegian Institute for Nature Research, Trondheim, Norway

Waigl, Christine F., Geophysical Institute, University of Alaska Fairbanks, Fairbanks, Alaska

Walker, Donald (Skip) A., Institute of Arctic Biology, University of Alaska Fairbanks, Fairbanks, Alaska

Walsh, John E., International Arctic Research Center, University of Alaska Fairbanks, Fairbanks, Alaska

Wang, Muyin, NOAA/OAR Pacific Marine Environmental Laboratory, Seattle, Washington; Cooperative Institute for Climate, Ocean, and Ecosystem Studies, University of Washington, Seattle, Washington

Webster, Melinda, Polar Science Center, Applied Physics Laboratory, University of Washington, Seattle, Washington

Wolken, G., University of Alaska Fairbanks, Fairbanks, Alaska; Alaska Division of Geological & Geophysical Surveys, Fairbanks, Alaska

Wouters, B., Department of Geoscience and Remote Sensing, TU Delft, Delft, The Netherlands

Yang, Dedi, Environmental Sciences Division, Oak Ridge National Laboratory, Oak Ridge, Tennessee

Editorial and Production Team

Allen, Jessicca, Graphics Support, Cooperative Institute for Satellite Earth System Studies, North Carolina State University, Asheville, North Carolina

Camper, Amy V., Graphics Support, Innovative Consulting and Management Services, LLC, NOAA/NESDIS National Centers for Environmental Information, Asheville, North Carolina

Carroll, Lauren, Content Team Lead, Communications and Outreach, NOAA/NESDIS National Centers for Environmental Information, Asheville, North Carolina

Crossman, Jacquelyn, NCEI Librarian, MPF-ZAI, NOAA/NESDIS National Centers for Environmental Information, Asheville, North Carolina

Haley, Bridgette O., Graphics Support, NOAA/NESDIS National Centers for Environmental Information, Asheville, North Carolina

Noguchi, Lukas, Technical Editor, Innovative Consulting and Management Services, LLC, NOAA/NESDIS National Centers for Environmental Information, Asheville, North Carolina

Ohlmann, Laura, Technical Editor, Innovative Consulting and Management Services, LLC, NOAA/NESDIS National Centers for Environmental Information, Asheville, North Carolina

Veasey, Sara W., Visual Communications Team Lead, Communications and Outreach, NOAA/NESDIS National Centers for Environmental Information, Asheville, North Carolina

5. Table of Contents

5. THE ARCTIC

T. A. Moon, M. L. Druckenmiller, and R. L. Thoman, Eds.

a. Overview

—T. A. Moon, M. L. Druckenmiller, and R. L. Thoman

Environmental conditions across the Arctic, a vast area above 60°N, look today remarkably different than one or two decades ago. Modern satellite era measurements of Arctic annual surface air temperature (1979–2025) show that the region has, on average, warmed roughly three times faster than the rest of the planet. Human emissions of heat-trapping gases are driving the change globally with additional processes in the Arctic amplifying the heating (section 5c). The impacts touch every corner of the terrestrial and marine landscape, including serious compounding hazards for people in the Arctic. This chapter delves into these long-term trends and details 2025 observations across the Arctic system, including a section on 2023/24 observations on glaciers and ice caps outside of Greenland (section 5h, which alternates yearly with a section on Arctic river discharge).

Examining surface temperature in the Arctic, 2025 was the second warmest year since the observational record began in 1900 (section 5c). The surface temperature anomaly for the year was 1.38°C above the 1991–2020 mean, a reflection of warmer-than-usual temperatures occurring across seasons. Autumn and winter continue to show the strongest increases in surface warming as compared to global trends, and 2025 marked the 12th consecutive year that Arctic temperature anomalies were higher than global surface temperature anomalies. Temperature changes also occur from the Earth's surface up through the troposphere and stratosphere. The Arctic troposphere has warmed 0.3°C decade^{-1} since 1958, while the stratosphere has cooled by a similar amount, an expected pattern with human-caused climate change (section 5b). In 2025, polar tropospheric air temperatures were the second highest on record.

Overall warming in the Arctic is accompanied by increases in precipitation, including the potential for bigger rain and snow events. During the period 1950–2025, there was an upward trend in annual precipitation totals, including significant upward trends in all seasons (section 5d). Examining annual records, 2025 had the third highest annual precipitation total on record, and the largest precipitation anomalies with respect to 1991–2020 were in winter (112%), spring (108%; the highest spring anomaly on record), and autumn (104%). Snow cover extent is connected to these coupled changes in precipitation and temperature, with patterns of snowpack buildup and melt shifting over the last several decades. In 2025, Arctic snow cover extent was roughly normal in Eurasia and North America in May but dropped below normal in June with early loss of snow cover, a now common occurrence (section 5i).

Arctic landscapes both respond to and influence temperature and precipitation changes. With vast areas of tundra as well as permafrost, the Arctic is home to a unique physical system that is responding rapidly to overall warming. Changes in Arctic tundra plants and productivity, such as increases in the abundance, distribution, and height of shrubs, result in Arctic "greening", which has been detected since the late 1990s. Beginning in 2020, the Arctic has experienced a sequence of record- or near-record-high greenness values, to which 2025 is now added as the third highest value (section 5k). Local and regional variation is notable, however, with, for example, both greening and "browning" in the Eurasian Arctic. Vegetation changes in the Arctic are intrinsically connected to changes in permafrost as well. Since the 1980s, permafrost across the Arctic has seen a long-term warming trend, with the strongest trends in high-latitude, cold permafrost (section 5j). The active layer thickness, or the maximum depth of surface ground that seasonally thaws and freezes, has also increased, though at different regional rates.

Permafrost thaw is also a key player in Arctic terrestrial carbon dioxide and methane storage, though other important processes are also at play, such as wildfire, wetland development or loss, and river and lake outgassing. Examining tundra and boreal forest ecosystems in Arctic permafrost regions suggests that together carbon dioxide from these sources made the region a small net carbon dioxide source during the period 2000–20 (Sidebar 5.2). This is a serious and potentially long-term shift from Arctic permafrost regions acting as a carbon dioxide sink that dampens warming to a source that can enhance warming. Subannual records also show that the seasonal cycle of carbon storage and release is amplifying, reflecting both stronger winter emissions and stronger summer uptake (Sidebar 5.2).

Dramatic change continues for other frozen components of the Arctic system. On land, the Greenland Ice Sheet, which holds the second largest reservoir of frozen fresh water on the planet, had yet another year of overall ice loss (129±50 Gt based on gravity measurements; section 5g). Sixty percent of the planet's glaciers and ice caps outside of Greenland and Antarctic are also found in the Arctic, and ice loss across these areas has tripled since the mid-1990s. During 2023/24, both Arctic Scandinavia and Svalbard had record years of ice loss with melt 1473% above the 1991–2020 mean in Arctic Scandinavia and 482% above in Svalbard (section 5h).

Arctic sea ice records also continue to show very low extent and predominantly first-year ice. The maximum sea ice extent in March 2025 was the lowest in the 47-year record, continuing a downward trend of –2.5% per decade, while September 2025 minimum extent was the 11th lowest on record, adding to a trend of –13.6% per decade extent loss (section 5f). Ice older than four years old is now nearly absent, with only 95,000 km^2 of older ice in September 2025 as compared to 1.5 million km^2 in the 1980s. Without sea ice cover, Arctic Ocean surface waters are exposed to heating from solar radiation and the atmosphere. Examined annually in August, the 2025 sea surface temperature in most Arctic Ocean regions was the highest in the 1982–2025 record and the pan-Arctic mean was the second highest on record (section 5e).

Pervasive environmental changes have direct and indirect impacts on people within and beyond the Arctic (e.g., Meng et al. 2023; Moon et al. 2019). In many instances, communities experience the combined impacts of multiple rapidly changing systems. For example, permafrost thaw and glacier retreat are increasing hazards such as glacial lake outburst floods, landslides, and the reliability of water supplies. Extreme weather hazards are also increasing. A prime example is the devastating ex-typhoon Halong that hit the Alaska west coast on 11–12 October 2025 (Sidebar 5.1). The storm traveled across anomalously warm ocean surface temperatures, and peak storm surge arrival on shore coincided with the daily high tide. Storm impacts were intense and widespread, including substantial inland and coastal flooding, ferocious winds, infrastructure loss, and loss of life.

The pace of change and the seriousness of impacts across plants, animals, and people highlight the importance of maintaining and strengthening our environmental intelligence regarding the Arctic region. Real threats to our scientific monitoring ability exist, such as the loss of a long-term Arctic vegetation monitoring dataset due to funding cuts (section 5k). This chapter's observations show that the Arctic today is vastly different than the past, requiring close attention and increased action for hazard preparedness and response.

b. Atmosphere

—A. H. Butler, S. H. Lee, G. H. Bernhard, V. E. Fioletov, J.-U. Grooß, I. Ialongo, B. Johnsen, K. Lakkala, R. Müller, and T. Svendby

The Arctic atmosphere is changing rapidly due to increasing greenhouse gases and associated melting sea ice. Since 1958, the Arctic troposphere has warmed ~0.3°C decade^{-1}, with amplified warming at the surface, while the Arctic stratosphere has cooled by roughly the same amount (Fig. 5.1)—a fingerprint of human-caused carbon dioxide (CO_2) increases (e.g., Santer et al. 2023). The magnitude of these temperature trends varies by season, altitude, and time period over which the trend is calculated (Fig. 5.1; Riviere et al. 2024), reflecting year-to-year variability associated with the downward influence from the stratosphere, tropical to extratropical teleconnections, and high-latitude weather systems that drive moisture and heat transport into and out of the region.

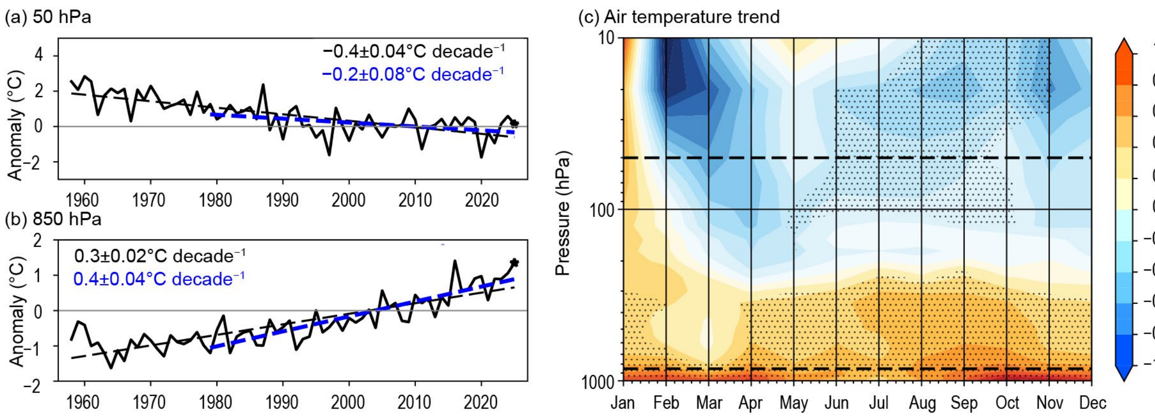

Fig. 5.1. Polar cap (60°N–90°N) air temperature trends from ERA5 reanalysis. Panels (a) and (b) show annual-mean temperature anomalies (°C; 1991–2020 climatology) at the 50-hPa and 850-hPa pressure level, respectively. Dashed black and blue lines in (a) and (b) show the least-squares linear fit to the data for the period 1958–2025 and 1979–2025 (satellite era), respectively, with corresponding trend values ± standard error. Panel (c) shows 1979–2025 linear trends in air temperature (°C decade^{-1}) by pressure level and month (adapted from Riviere et al. 2024). Stippling denotes p<0.025 significance (2-tailed Student's t-test). Horizontal dashed lines correspond to the pressure levels in (a) and (b).

In 2025, annual-mean polar tropospheric air temperatures at 850 hPa were the second highest on record (Fig. 5.1b; throughout this section, anomalies are defined relative to the 1991–2020 climatology over the 1958–2025 ERA5 reanalysis record, unless otherwise noted). Negative trends in lower polar stratospheric temperatures have slowed since the turn of the century, coincident with the recovery of the global ozone layer (Ferraro et al. 2015; Weber et al. 2022), and the 2025 value was near average (Fig. 5.1a). In addition to long-term changes, we highlight below the seasonal circulation and ozone variability in 2025.

1. WINTER (JANUARY–MARCH)

Winter Arctic tropospheric temperatures were above average, in agreement with widespread positive geopotential height anomalies at 500 hPa (Fig. 5.2a), with record warmth in February (Fig. 5.3b). In contrast, the Arctic lower stratosphere was

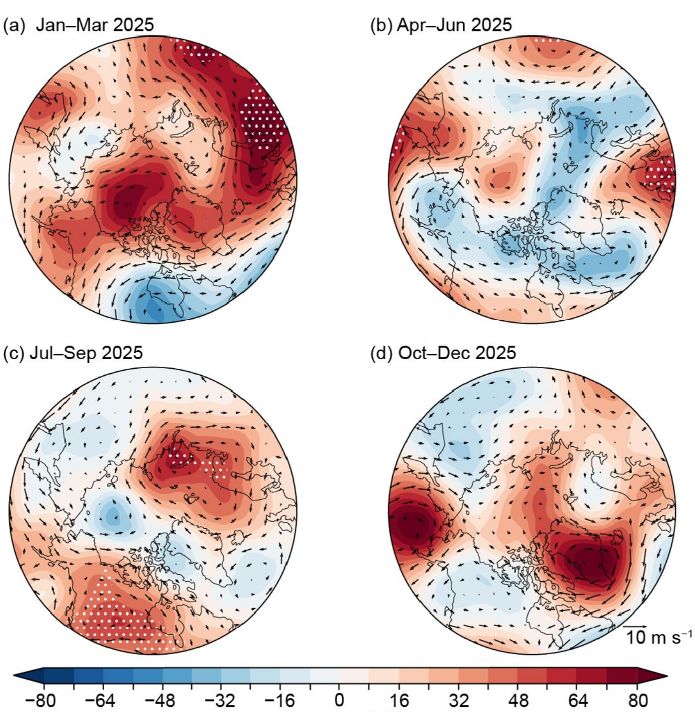

Fig. 5.2. Seasonal 500-hPa geopotential height (m; shading) and 200-hPa wind vector (m s^{-1}) anomalies for (a) winter (Jan–Mar; JFM), (b) spring (Apr–Jun; AMJ), (c) summer (Jul–Sep; JAS), and (d) autumn (Oct–Dec; OND). Higher geopotential heights generally indicate warmer air columns. Anomalies are relative to the 1991–2020 climatology; stippling denotes anomalies exceeding ±2 std. dev. (Source: ERA5 [Hersbach et al. 2020].)

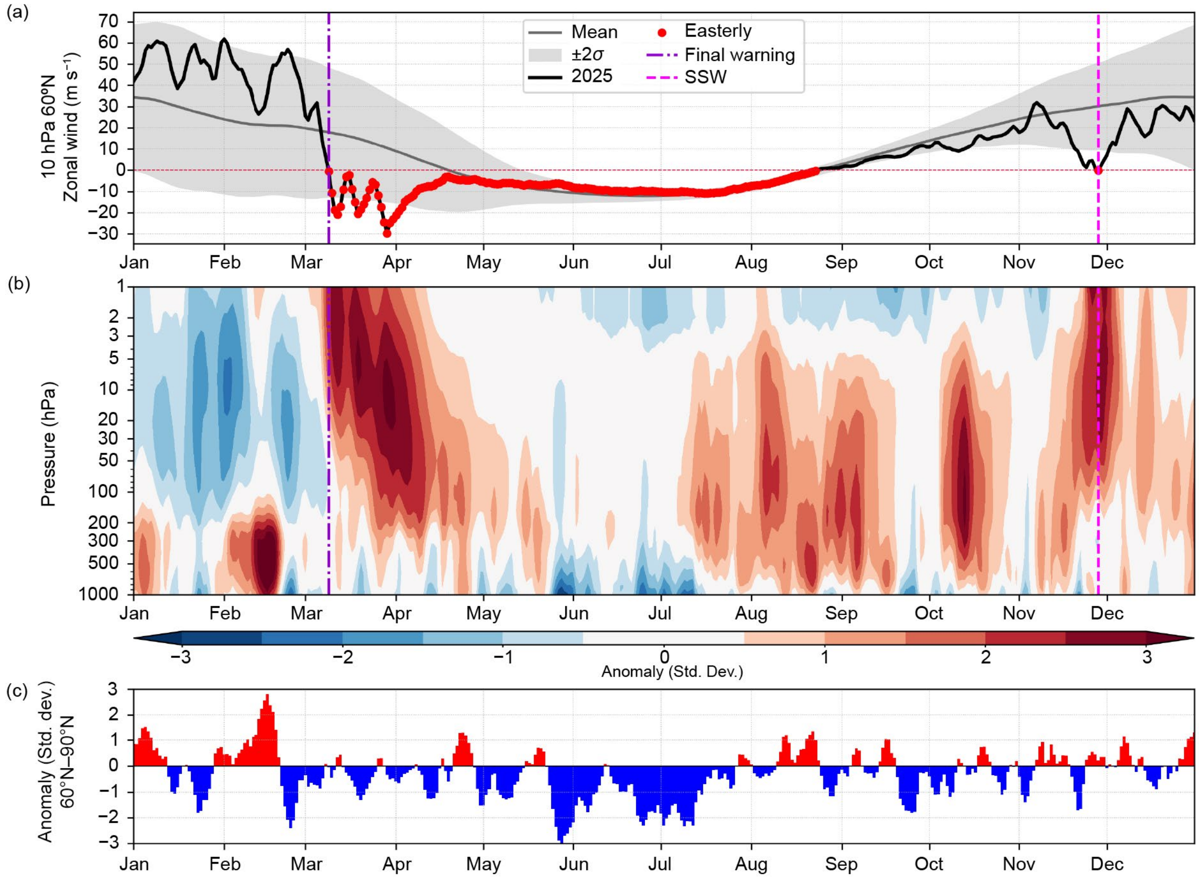

Fig. 5.3. 2025 Arctic atmosphere dynamics. (a) Daily stratospheric polar vortex winds (zonal-mean zonal winds at 10 hPa and 60°N) in black, with the 1991–2020 mean and ±2σ spread in gray. Red dots indicate easterly winds. (b) Vertical cross-section of daily polar cap-averaged (60°N–90°N) geopotential height anomalies in standard deviations. Purple dash-dot and pink dashed lines mark the 9 March final stratospheric warming and 28 November sudden stratospheric warming, respectively. (c) 1000-hPa polar cap-averaged (60°N–90°N) geopotential height anomalies. Anomalies are relative to 1991–2020. (Source: ERA5.)

extremely cold in January and February (the second coldest February on record at 50 hPa). This was associated with a stronger-than-normal polar vortex (Fig. 5.3a) and extremely low total column ozone anomalies stretching across the Arctic from eastern Canada to Asia (Fig. 5.4a). These regions of anomalously low ozone corresponded to broad increases (~30%) in ultraviolet (UV) radiation in February, according to satellite-based and ground-based measurements (though absolute values of UV in February are low due to partial polar darkness; Fig. 5.4c).

A strong Scandinavian anticyclone in February, concurrent with anomalously high pressure over Alaska, likely triggered a planetary-scale wave forcing that led to the second-earliest stratospheric final warming—the seasonal transition of the stratospheric polar vortex from a westerly to easterly state—on record, on 9 March 2025 (Fig. 5.3a). As the vortex broke down, it was displaced towards Europe, leading to a hemispheric dipole in the March total column ozone anomalies. Extremely low ozone remained in the vortex core; the minimum of March vortex total column ozone was 303 Dobson units (DU), which was the second lowest of the last four decades, after the year 2020. Conversely, strong positive anomalies formed over Alaska and the North Pacific, driven by accelerated stratospheric transport and enhanced mixing (Fig. 5.4b). Correspondingly, UV measurements showed strong surface UV radiation increases of ~30%–60% over Europe and Scandinavia but modest reductions over the Canadian archipelago and Canada (Fig. 5.4d). Some differences between ground- and satellite-based UV measurements are evident, particularly at Trondheim in March, which may be due to cloudiness conditions at that station, and climatologies used in the satellite retrievals, which do not always match the actual albedo (Bernhard et al. 2015).

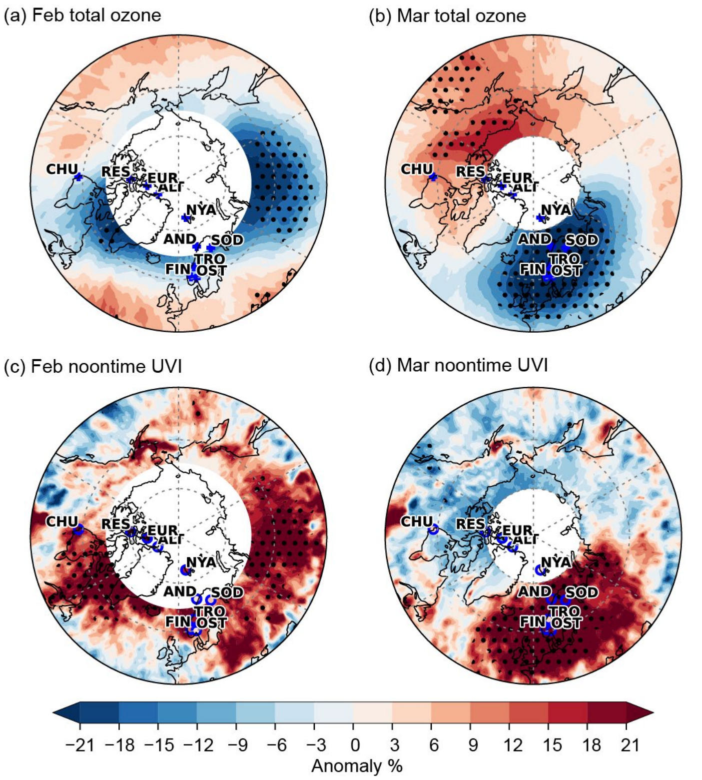

Base	Feb noontime UVI (satellite)	Feb noontime UVI (ground-based)	Mar noontime UVI (satellite)	Mar noontime UVI (ground-based)
ALT	N/A	N/A	N/A	–6%
EUR	N/A	28%	N/A	–11%
NYA	N/A	17%	N/A	4%
RES	N/A	31%	N/A	–6%
AND	N/A	3%	18%	19%
SOD	N/A	6%	27%	33%
TRO	20%	18%	29%	5%
FIN	15%	11%	44%	30%
OST	17%	3%	56%	40%
CHU	12%	25%	1%	5%

Fig. 5.4. Monthly ozone and ultraviolet (UV) anomalies. Panels (a),(b) show total ozone column (%) and (c),(d) noontime UV index (UVI; %) for Feb (a),(c) and Mar (b),(d) 2025 relative to 2005–24 means, using the Ozone Monitoring Instrument (OMI) Level-2 Total Column Ozone version 3 (OMTO3) product (Bhartia and Wellemeyer 2002). Stippling indicates anomalies exceeding ±2σ. Panels (c),(d) also show UVI anomalies (%) from ground-based measurements at 10 locations (shaded marker): Alert (ALT; 83°N); Eureka (EUR; 80°N); Ny-Ålesund (NYA; 79°N); Resolute (RES; 75°N); Andøya (AND; 69°N); Sodankylä (SOD; 67°N); Trondheim (TRO; 63°N); Finse (FIN; 61°N); Østerås (OST; 60°N); and Churchill (CHU; 59°N). White polar areas and values of N/A in the table indicate missing data due to polar darkness.

2. SPRING (APRIL–JUNE)

The early March dynamic final stratospheric warming led to a circulation perturbation that descended to the tropopause through June but only intermittently affected the troposphere (Figs. 5.3a,b). While an early final stratospheric warming tends to be followed by a negative Northern Annular Mode (NAM)/North Atlantic Oscillation (NAO)-like pattern—consisting of positive geopotential height anomalies over the polar cap—the mid-troposphere and surface instead showed broadly negative geopotential height anomalies across the polar region (Figs. 5.2b, 5.3b,c). Near the surface at 1000 hPa, polar cap-averaged height anomalies were persistently negative, especially in late May into June.

3. SUMMER (JULY–SEPTEMBER)

Summer featured cohesive positive polar geopotential height anomalies from the near-surface into the quiescent summer stratosphere (Fig. 5.3b). These positive height anomalies mainly arose due to two large anticyclones dominating the summertime mid-tropospheric flow: one over the Barents–Kara Sea region that peaked in strength in August and then retrograded towards Scandinavia in September, and another over Canada that was weakly present in August and amplified in September (Fig. 5.2c). This setup resulted in weak anomalous upper-tropospheric wind flow over the central Arctic and Baffin Bay.

4. AUTUMN (OCTOBER–DECEMBER)

The tropospheric circulation in autumn (Fig. 5.2d) showed two anticyclones over Greenland and the Bering Strait in the seasonal average, yet there was large month-to-month variability. For example, October was exceptionally warm in the troposphere, with record to near-record warmth from the surface (section 5c) to upper troposphere, potentially associated with two anticyclones over Canada and the Barents–Kara Seas region. On the other hand, December was extremely cold in eastern Alaska and the Yukon Territory, due to an exceptionally strong ridge over the Bering Strait supporting a downstream surface anticyclone, allowing for maximum surface cooling from northerly advection of Arctic air. In the stratosphere, the polar vortex was weaker than normal until November, when extended tropospheric wave forcing predominantly from the Greenland blocking high helped to displace the stratospheric polar vortex towards Asia, leading to one of the earliest major sudden stratospheric warmings in the ERA5 record (28 November, tied with 28 November 1968; Fig. 5.3a). The downward influence from this event just reached the Arctic troposphere by the end of December 2025 (Fig. 5.3b).

c. Surface air temperature

—T. J. Ballinger, A. Crawford, A. H. Butler, M. C. Serreze, S. Bigalke, J. E. Walsh, B. Brettschneider, R. L. Thoman, U. S. Bhatt, E. Hanna, H. Motrøen Gjelten, S.-J. Kim, J. E. Overland, and M. Wang

1. OVERVIEW

Arctic (60°N–90°N) surface air temperature (SAT) in 2025 continued to rise faster than the global (90°S–90°N) rate. Over the modern satellite era since 1979, the Arctic annual SAT has increased approximately three times faster than the global mean, a phenomenon often termed Arctic Amplification, due in large part to anthropogenic greenhouse gas emissions and amplifying feedbacks (Sweeney et al. 2023; Zhou et al. 2024).

Arctic Amplification has been linked to numerous physical and ecological changes that affect transportation, infrastructure, and subsistence livelihoods for people living in the North, with cascading impacts extending across lower latitudes (Moon et al. 2019; Walsh et al. 2020). Warming responses within the Arctic include increased annual precipitation (section 5d), persistent mass loss from the Greenland Ice Sheet (section 5g) and Arctic glaciers and ice caps (section 5h), and enhanced greening of tundra landscapes (section 5k). This section examines Arctic SAT in 2025 in historical context and highlights seasonal SAT and contemporaneous atmospheric circulation anomalies. Annual air temperatures follow the calendar year, with seasons defined as winter (January–March), spring (April–June), summer (July–September), and autumn (October–December).

2. HISTORICAL CONTEXT TO 2025 AIR TEMPERATURES

Time series of annual Arctic and global SAT anomalies from NASA's GISTEMP version 4 dataset (Lenssen et al. 2019) are shown in Fig. 5.5a. This past year was the second warmest on record since 1900 in the Arctic with an anomaly of 1.38°C above the 1991–2020 mean. This marks the 12th consecutive year that pan-Arctic temperature departures exceeded the global average (+0.58°C). Arctic and global seasonal anomalies over the past year were also above average (Figs. 5.5b–e). At both scales, all seasons ranked among their 10 warmest since 1900. However, annual and seasonal SAT anomalies and long-term trends continue to outpace global SAT trends, most notably in autumn and winter.

At the seasonal scale, Arctic Amplification is most pronounced during autumn and winter (Figs. 5.5b,e) when heat accumulated in the Arctic Ocean mixed layer from solar energy absorption in growing open water areas (section 5f) and northward advection of warm sub-Arctic water masses (e.g., Polyakov et al. 2025) is released to the overlying atmosphere. Arctic Amplification is strongest in the lower troposphere because the atmosphere is more stable in the Arctic than in lower latitudes, which inhibits vertical mixing and confines heating near the surface (Serreze et al. 2026). Spatial patterns of Arctic SAT anomalies, shown and discussed below, align with some of these processes.

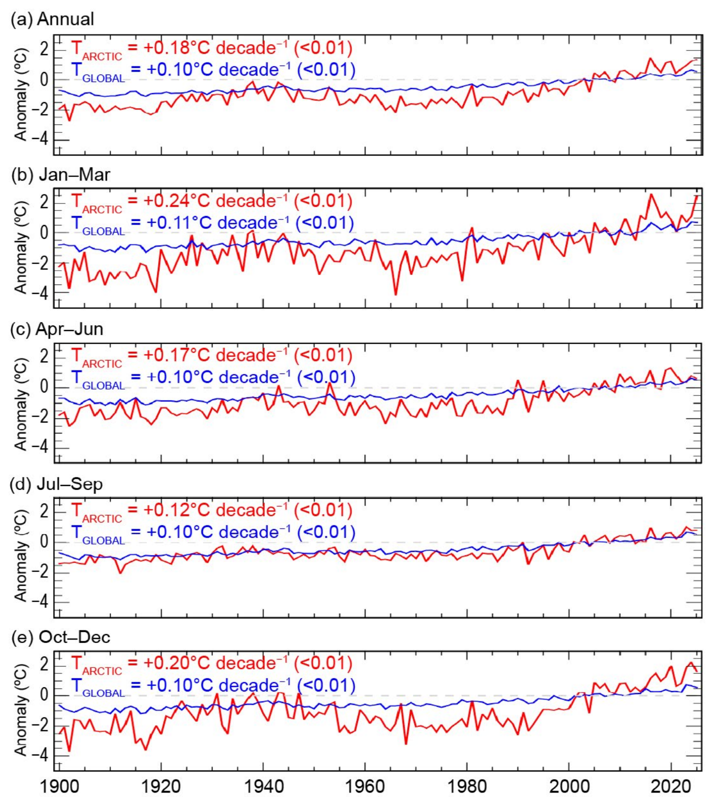

Fig. 5.5. Time series of (a) annual, (b) winter (Jan–Mar), (c) spring (Apr–Jun), (d) summer (Jul–Sep), and (e) autumn (Oct–Dec) surface air temperature anomalies (°C) averaged across Arctic (60°N–90°N) and global (90°S–90°N) land and ocean areas. The Arctic (T_{ARCTIC}) and global (T_{GLOBAL}) air temperature trends (°C decade^{-1}) for the 1900–2025 period are shown in each panel. All trends, based on linear least squares regression, are statistically significant ($p<0.01$). (Source: NASA GISTEMP v4.)

3. SEASONAL AIR TEMPERATURE ANOMALY PATTERNS IN 2025

Seasonal Arctic SAT anomaly patterns from ERA5 (Hersbach et al. 2020) are shown in Fig. 5.6. During winter (Fig. 5.6a), record-high temperatures were found over the Canadian Arctic Archipelago and the southern Barents Sea, with more modest anomalies over Alaska, the Bering Sea, Baffin Bay, the Lincoln Sea, the central Arctic Ocean, and east central Eurasia. The lone areas of below-average temperatures were eastern Siberia and north central Canada. Positive SAT anomalies in the North Atlantic Arctic sector are consistent with a relatively strong sea level pressure (SLP) dipole (Fig. 5.7a). This was characterized by below-average SLP (6 hPa–7 hPa below the 1991–2020 mean) indicative of an active storm track over eastern Canada promoting warm air advection west of Greenland.

During spring, near-average SAT characterized much of the Arctic Ocean and landmasses. Exceptions included record-high seasonal SATs over eastern Siberia and the Sea of Okhotsk, central Russia, and the Norwegian Sea (Fig. 5.6b). Central Greenland and the Kara Sea also saw above-average spring temperatures. Weak SLP anomalies covered much of the Arctic Ocean, except over the Kara Sea and the Canadian Arctic Archipelago. Below-average SLP also characterized Greenland and the Icelandic Low region to the south, which, along with slightly elevated SLP over western Europe, helped transport unseasonably warm air across the southern Norwegian Sea and drive record-high surface air temperatures in the region (Fig. 5.7b).

Summer saw average to above-average air temperatures over much of the Arctic with the exception of record warmth located over the North Atlantic Arctic, including central and eastern Greenland, the Norwegian Sea, northern Scandinavia, and areas northeast of Svalbard (Fig. 5.6c), associated with a large, blocking high pattern over the Barents Sea and Kara Sea (see Fig. 5.2c). Small anomalies over the Arctic Ocean are consistent with the cooling effects of a melting sea ice surface. Elevated SAT spanned much of the Kara Sea coastline and areas extending southward into central Eurasia, while on the North American side, north central Canada saw above-average SAT under anticyclonic conditions associated with higher-than-average SLP (Fig. 5.7c).

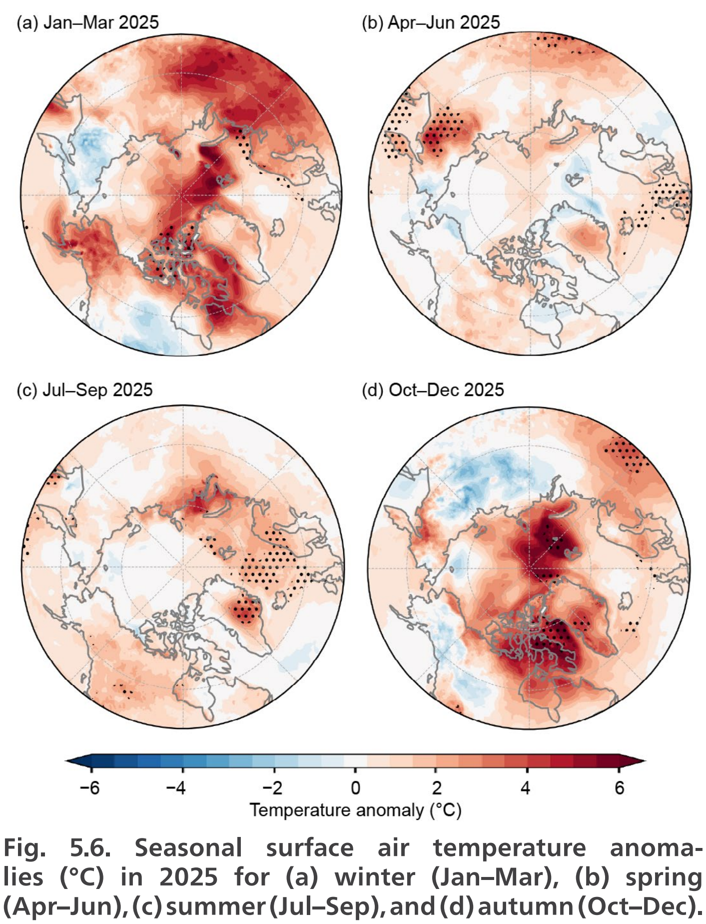

Fig. 5.6. Seasonal surface air temperature anomalies (°C) in 2025 for (a) winter (Jan–Mar), (b) spring (Apr–Jun), (c) summer (Jul–Sep), and (d) autumn (Oct–Dec). Temperature anomalies are shown relative to their 1991–2020 means. Stippled areas indicate record-high seasonal temperatures since 1940. (Source: ERA5.)

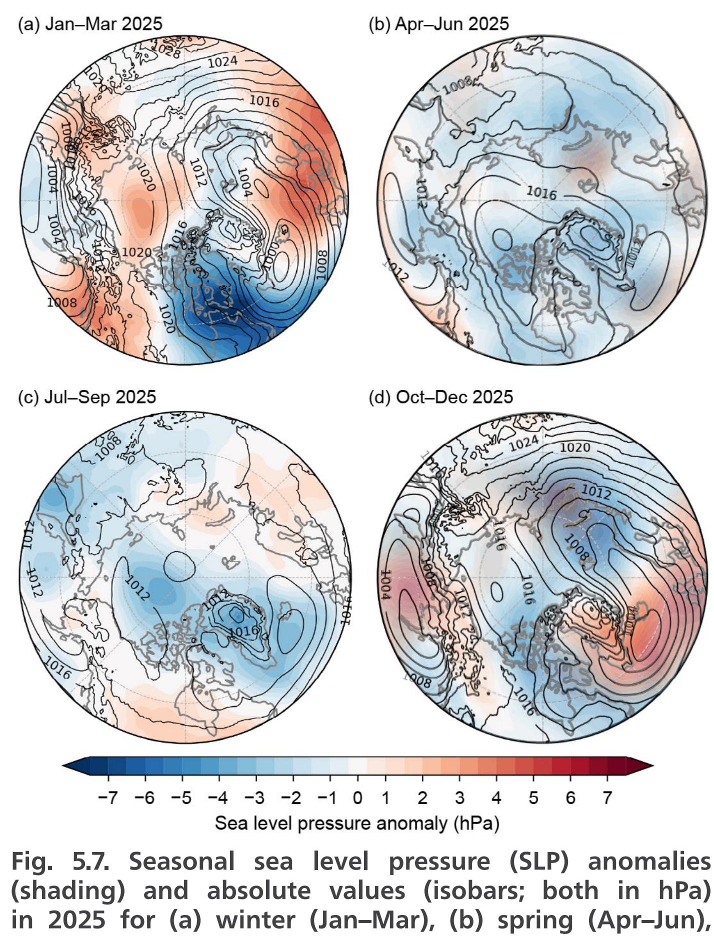

Fig. 5.7. Seasonal sea level pressure (SLP) anomalies (shading) and absolute values (isobars; both in hPa) in 2025 for (a) winter (Jan–Mar), (b) spring (Apr–Jun), (c) summer (Jul–Sep), and (d) autumn (Oct–Dec). SLP anomalies are shown relative to their 1991–2020 means. (Source: ERA5.)

Much of the North Atlantic Arctic was anomalously warm in autumn 2025 (Fig. 5.6d), with the magnitude of the anomalies relatively greater compared to other seasons across the calendar year. Record-high temperature anomalies of up to +6°C covered much of Baffin Bay, Baffin Island, and the Barents Sea while records were also set in the eastern Lincoln Sea and central Arctic Ocean. Portions of central Greenland, the Denmark Strait, and western Eurasia also saw record warmth, albeit with smaller SAT anomalies. Positive SLP anomalies around Greenland (Fig. 5.7d) coincided with a strong anticyclone aloft that produced flow from the southeast across Baffin Bay (see Fig. 5.2d). This pattern likely stunted sea ice advance across the region thereby shaping the pattern of record warmth west of Greenland. The two positive SLP anomaly centers over Greenland and the Bering Strait (Fig. 5.7d) were amplified at upper levels of the troposphere, suggesting a wavenumber-2 wave forcing may have contributed to one of the earliest sudden stratospheric warmings on record (section 5b).

d. Precipitation

—M. C. Serreze, S. Bigalke, R. Lader, A. Crawford, and T. J. Ballinger

1. INTRODUCTION

Annual precipitation over the Arctic region is characterized by high totals over the Atlantic sector (locally >2000 mm) due to open water and the frequent passage of storm systems, contrasting with polar desert (250 mm or less) over much of the Canadian Arctic Archipelago and central Arctic Ocean. Within these patterns, there is strong seasonality and local-to-regional variability. Obtaining accurate measurements of Arctic precipitation to assess anomalies and change is challenged by the sparse observation network—notably over the Arctic Ocean—and observation errors due to factors such as gauge undercatch of solid precipitation (Serreze et al. 2003).

To assess 2025 Arctic precipitation anomalies and historical trends, data from the ERA5 atmospheric reanalysis are utilized (Hersbach et al. 2020), which performs slightly better than other atmospheric reanalyses at matching observed precipitation (Barrett et al. 2020; Loeb et al. 2022), along with the gauge-based Global Precipitation Climatology Centre (GPCC) dataset (land-only measurements; Becker et al. 2013; Schneider et al. 2022). The Arctic is taken as the region poleward of 60°N. Winter, spring, summer, and autumn are defined as January–March, April–June, July–September, and October–December, respectively.

2. ANNUAL AND SEASONAL ARCTIC PRECIPITATION

For the Arctic as a whole, annual precipitation for 2025 based on ERA5 was 106.0% of the 1991–2020 average, the third highest total on record, reinforcing an upward trend as assessed over the period 1950–2025. Percent anomalies with respect to 1991–2020 by season were 111.8% (fourth highest on record) for winter, 108.3% for spring (record high), 99.7% for summer, and 104.3% for autumn (ninth highest). Summer was near the long-term average.

3. REGIONAL ANOMALIES

Figure 5.8 shows the spatial pattern of seasonal precipitation anomalies for 2025 based on ERA5. Regionally, above-to-slightly-above average precipitation over the Atlantic sector in winter contrasted with below-average precipitation over northern Europe and along the west coast of Canada. The dominant features of spring were above-average precipitation over coastal Alaska and the southeast coast of Greenland, both pointing to the effects of orographic uplift. Precipitation was somewhat low over most of Canada and northern Europe (with northern Norway as an exception), the latter continuing the pattern from winter. Summer dryness over most of Canada stands out, as does dry conditions over much of northern Eurasia. In autumn, the pattern shifted to above-average precipitation over Canada, while much of Arctic Eurasia remained dry.

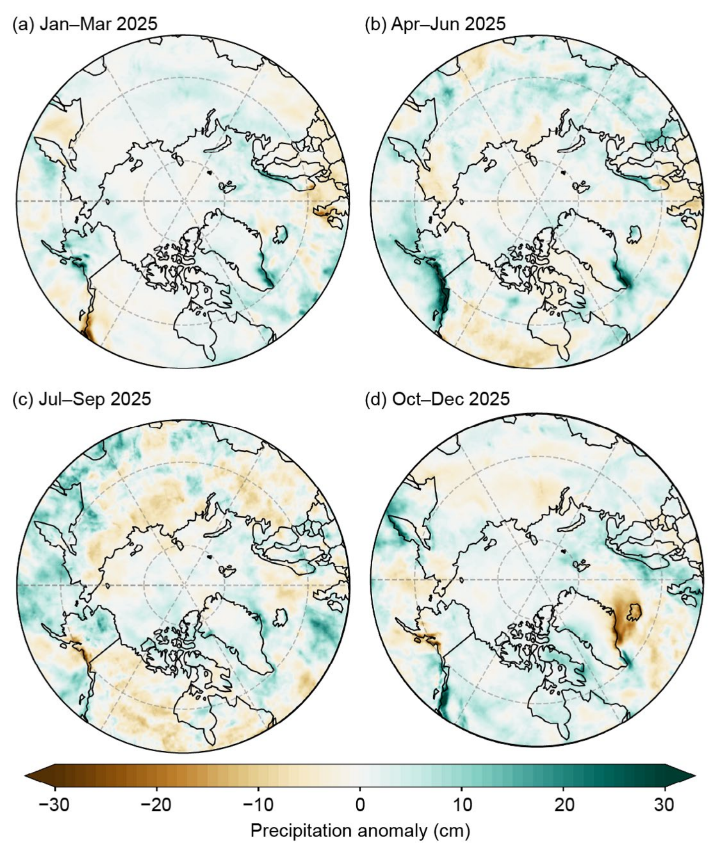

Fig. 5.8. Seasonal precipitation anomalies (cm; 1991–2020 baseline) in 2025 for (a) winter (Jan–Mar), (b) spring (Apr–Jun), (c) summer (Jul–Sep), and (d) autumn (Oct–Dec). Green shades denote above-average precipitation and brown shades denote below-average precipitation. (Source: ERA5.)

4. HEAVY PRECIPITATION EVENTS

Regionally heavy precipitation events in any year can approach or exceed previous records, even in a stable climate. Such events are important to track as they can result in flooding, loss of life, and damage to infrastructure. Figure 5.9 shows the pattern of heavy precipitation events by season in terms of ranks of the maximum five-day precipitation events (Rx5) in each season (relative to the 1950–2024 period). The standout feature is the comparatively higher density of heavy precipitation events across the Arctic in winter compared with the other seasons. Note especially the band of heavy precipitation events in winter stretching northward from south of the Aleutian Islands across Alaska. Much of that precipitation was related to a large northward pulse of moisture (an "atmospheric river") during 22–25 January. The associated southerly winds also contributed to above-average surface air temperatures across these areas (section 5c). As the water cycle intensifies and extreme precipitation events become more common (Yu and Zhong 2021; Dou et al. 2022), disruption to ecosystems (e.g., Christensen et al. 2020; Serreze et al. 2021) and human infrastructure (e.g., Hansen et al. 2014; Fox et al. 2023) will further impact Arctic communities.

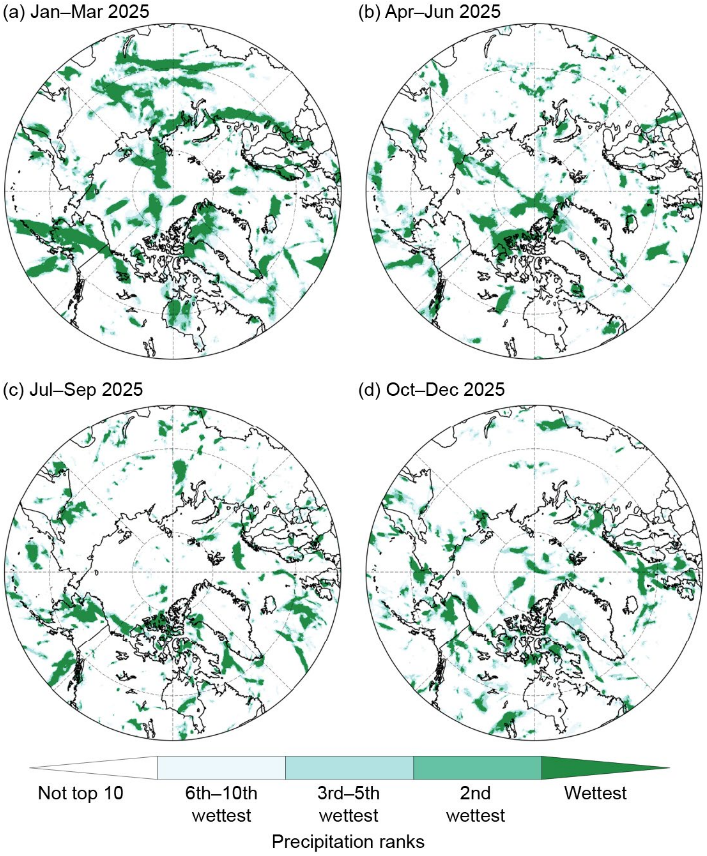

Fig. 5.9. Ranks of maximum five-day precipitation in 2025 for (a) winter (Jan–Mar), (b) spring (Apr–Jun), (c) summer (Jul–Sep), and (d) autumn (Oct–Dec) relative to the 1950–2024 period. (Source: ERA5.)

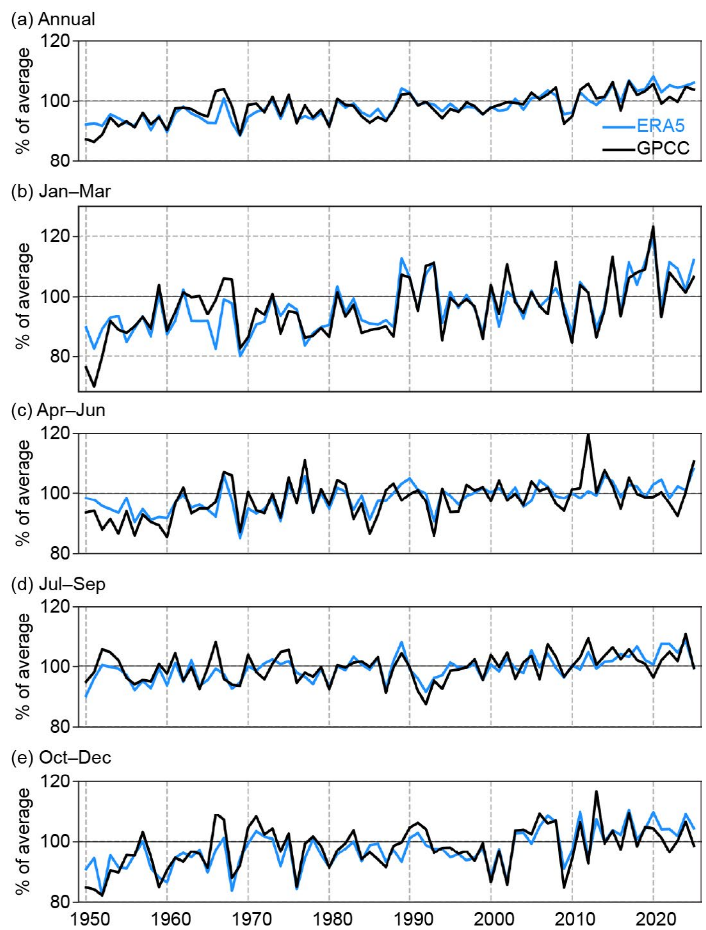

Fig. 5.10. Time series of Arctic (60°N–90°N) precipitation from 1950 through 2025 expressed as a percentage of the 1991–2020 average (%; shown by the horizontal black lines at 100%). (Source: ERA5 [blue lines] and Global Precipitation Climatology Centre [GPCC] 1.0° data [black lines].) GPCC values are for land only; ERA5 values are for land plus ocean.

5. HISTORICAL PERSPECTIVE

Climate models project increased Arctic precipitation and more frequent heavy precipitation events as the climate warms, as well as an increase in the proportion of precipitation falling as rain. Previous studies addressing trends (Box et al. 2021; Yeh et al. 2021; Yu and Zhong 2021; Walsh et al. 2022a) emphasize interannual and multiyear variability and large regional variations in trends, as well as evidence of a transition from solid to liquid precipitation in the warmer parts of the Arctic (Box et al. 2021). However, as discussed in the Arctic precipitation section of the 2023 and 2024 *State of the Climate* reports and presented here with updates, pan-Arctic precipitation now has detectable upward trends in all seasons, as well as in the annual average.

Arctic precipitation time series from ERA5 (as a percentage of 1991–2020 averages for the region poleward of 60°N) are plotted in Fig. 5.10 along with the corresponding time series from the station-based GPCC dataset. While the percent anomaly time series from the two sources are generally similar, there are substantial differences for individual years due to the absence of coverage over the Arctic Ocean in GPCC and inherent uncertainties in each data source. The updated time series nevertheless reinforces the conclusion that precipitation for the Arctic region overall is increasing. Based on the ERA5 data from 1950–2025, the trend in annual mean precipitation stands at 0.75 cm decade^{-1}. Corresponding seasonal trends are 0.23 cm decade^{-1} for winter, 0.13 cm decade^{-1} for spring, 0.17 cm decade^{-1} for summer, and 0.23 cm decade^{-1} for autumn. Autumn and winter hence show the strongest seasonal trends. In terms of percent change relative to the 1991–2020 average, winter is strongest (2.25% decade^{-1}). Autumn is 1.7% decade^{-1}, summer is 1.01% decade^{-1}, spring is 1.11% decade^{-1}, and the year as a whole is 1.52% decade^{-1}.

The spatial pattern of annual trends for 1950–2025 is quite revealing (Fig. 5.11). Positive trends of up to 0.3 cm yr^{-1} are apparent over the North Atlantic sector of the Arctic and extending into the Barents Sea. The strong, positive trends along the Norwegian coast and parts of the southeast coast of Greenland point to orographic effects—forced uplift and cooling of moist air. Strong, positive trends along the Alaska coast are also consistent with orographic uplift. Pointing further to the spatial heterogeneity of trends, reductions in precipitation are seen in other areas, such as parts of Eurasia and Canada.

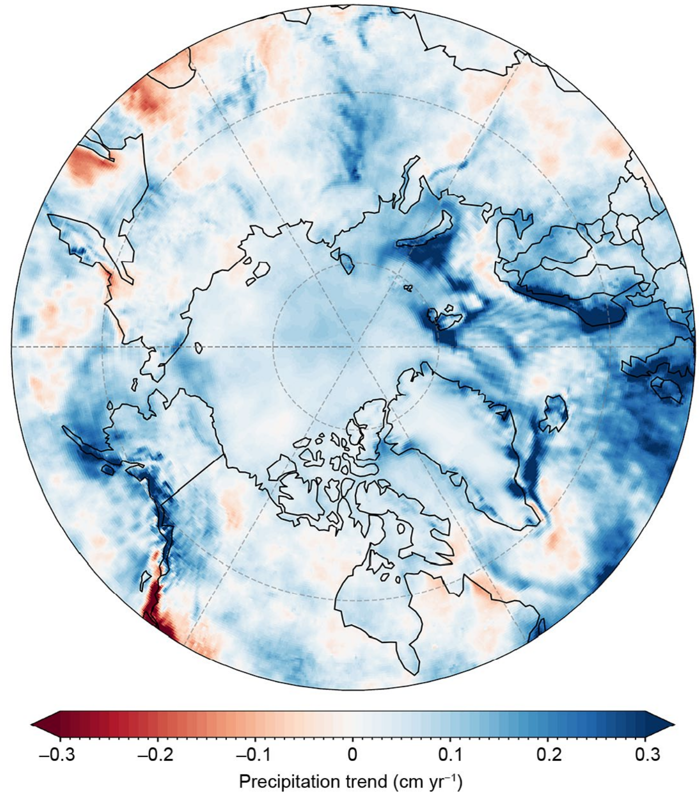

Fig. 5.11. Linear trends in annual precipitation (cm yr^{-1}) for the period 1950–2025. (Source: ERA5.)

Sidebar 5.1: **Ex-typhoon Halong**
—R. L. THOMAN

Southwest Alaska suffered widespread severe coastal flooding and wind damage during 11–12 October 2025 as ex-typhoon Halong tracked from the north-central Pacific Ocean northward through the eastern Bering Sea before moving into the Beaufort Sea north of Alaska. Dozens of primarily Yupik communities were adversely affected by the storm, with two communities almost entirely evacuated after the storm and over 1500 people relocated from across the region. Both the State of Alaska and the federal government issued disaster declarations in the aftermath of the storm. This was the latest in a series of high impact extreme weather events in Alaska in recent years, with the number of state-declared disasters about double since 2020 compared to 2014–19 (Thoman and McFarland 2024).

Hardest hit was the north shore of Kuskokwim Bay, a low-lying tundra region where thousands of square kilometers of land are at an elevation of five meters or less above mean sea level. The communities of Kipnuk (Fig. SB5.1) and Kwigillingok, located along rivers a few kilometers inland, suffered catastrophic flooding that damaged nearly all buildings and disabled most infrastructure, including electrical power and fresh and waste water systems. Homes with people inside were lifted off their foundations in the dead of night and floated several kilometers upriver, requiring helicopter rescue of those inside. One person from Kwigillingok died as a result of the storm, and two others remain unaccounted for. It was "the worst flooding in living memory", according to community members who have lived in the region for generations. The return timeline for both Kipnuk and Kwigillingok residents remains uncertain due to the extent of the damage, with many evacuees residing in the cities of Anchorage and Bethel, Alaska, many for an indefinite period of time.

Fig. SB5.1. Aerial view of Kipnuk, Alaska, on 12 October 2025 showing almost total inundation of the community. (Source: Alaska Air National Guard.)

Impacts from ex-Halong were not confined to coastal flooding. Strong winds caused municipal, tribal, and residential building and infrastructure damage and prolonged power outages in many coastal communities that were spared from storm surge. Additionally, communities as far as 200 kilometers inland experienced strong winds that downed many trees and caused power outages.

Typhoon Halong formed southeast of Japan on 5 October 2025 and rapidly intensified to a severe typhoon near Izu Island on 8 October (see section 4g4 for further detail on storm development). Thereafter, the storm turned northeast and transitioned to an extratropical cyclone (i.e., the primary energy for the storm changed from latent heat release to the horizontal temperature gradient) on 10 October. Ocean surface temperatures were above the 1991–2020 baseline average across virtually the entire track of Halong (Fig. SB5.2), from typhoon development southeast of Japan through the extratropical transition (ET) and across the eastern Bering Sea. After weakening rapidly prior to the ET, the lowest pressures in ex-Halong dropped significantly as the storm crossed the eastern Bering Sea, reaching a minimum pressure of 960 hPa at 1200 UTC on 12 October located between St. Lawrence Island and the Yukon River delta, whereafter the forward speed increased dramatically. Just 18 hours after reaching its minimum pressure, Halong was centered more than 1200 km to the northeast over the Beaufort Sea ice pack.

As the storm tracked northeastward, winds in the southeast quadrant of the storm were sustained at ~40 kt to 50 kt (21 m s^{-1} to 26 m s^{-1}), blowing onshore into the Kuskokwim delta coast. This produced a significant storm surge that unfortunately coincided in time with the daily high tide, making this a "worse-case" scenario. Had the timing of the storm surge corresponded with the daily low tide (e.g., 11 October evening instead of 12 October early morning), there would have been a prolonged "high tide" but little or no inundation (though wind damage would still have occurred).

Historical Context

Strong storms in the northern Bering Sea are common in the late summer and autumn. Based on the Crawford et al. (2021) storm track database, in the northern Bering Sea (north of 58°N, east of 180° longitude) between August and November during the 30-yr period of 1996–2025, there were 163 separate storms with a minimum pressure of 980 hPa or lower: only four were storms that originated as typhoons in the western Pacific. While Alaska's Aleutian Islands are occasionally impacted by ex-typhoons, historically it has been rare for such storms to track from the North Pacific through the Bering Sea and into the Arctic prior to dissipating. Based on the Joint Typhoon Warning Center (JTWC) Western North Pacific Ocean Best Track Data and supplemented with MERRA-2 and ERA5 reanalysis when needed, between 1970 and 2021, only ex-Typhoon Carlo, in October 1996, followed such a path. Ex-Carlo produced stormy weather in the Bering Strait region but no significant coastal flooding was documented. Since 2022, three ex-typhoons followed such a path: ex-Merbok in September 2022, which caused widespread devastation on the northeast Bering Sea coast, ex-Amphil in August 2024, which caused wind damage in the Bering Strait region but did not cause coastal flooding, and now ex-Halong in October 2025.

The path of ex-Halong in the eastern Bering Sea was also unusual for storms of this intensity. Based on the Crawford et al. (2021) storm track database, since 1950, only one other autumn storm with a minimum pressure of 970 hPa or lower followed a track such that the center passed between St. Lawrence and the Yukon River delta. That storm occurred in October 1987 and produced some flooding in the Kuskokwim delta, though nothing comparable to ex-Halong.

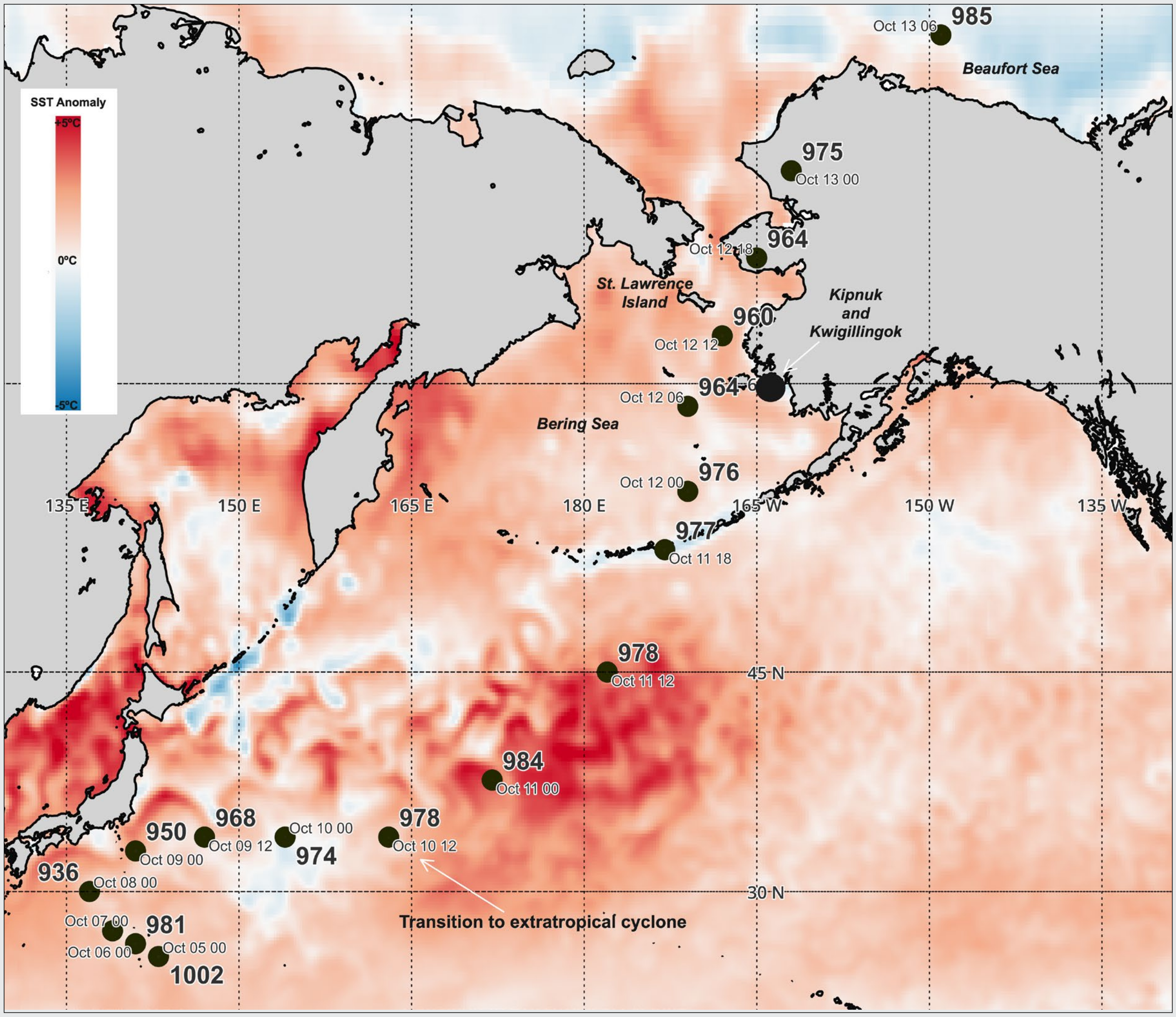

Fig. SB5.2. Track and intensity of ex-typhoon Halong during 5–13 October 2025. Positions (bold circle and date/time [UTC]) and minimum pressure (hPa) from the Joint Typhoon Warning Center (5–10 October) and the NWS Ocean Prediction Center (11–13 October) analyses. Color field is the 5–12 October 2025 average sea surface temperature anomalies (°C) relative to the 1991–2020 baseline based on NOAA Optimum Interpolated Sea Surface Temperature version 2.1 (OISSTv2.1).

e. Sea surface temperature

—M.-L. Timmermans and Z. M. Labe

Arctic Ocean sea surface temperatures (SSTs) in the summer are primarily influenced by the amount of incoming solar radiation absorbed by the sea surface and by the flow of warm waters into the Arctic from the North Atlantic and North Pacific Oceans. Solar warming of the Arctic Ocean surface is influenced by the sea ice distribution (with greater warming occurring in ice-free regions), cloud cover, and upper-ocean stratification. Inflows of relatively warm Arctic river waters can provide an additional heat source in coastal regions.

The SST data presented here are from the 0.25° × 0.25° NOAA Optimum Interpolation Sea Surface Temperature (OISST) Version 2.1 product (Huang et al. 2021). The analysis period spans June 1982 through September 2025, with 1991–2020 used as the climatological reference period. The analysis focuses most closely on August 2025 mean SSTs in context with the climatological record. August mean SSTs provide the most appropriate representation of Arctic Ocean summer SSTs because sea ice extent is near a seasonal low at this time of year, prior to the onset of surface cooling and subsequent sea ice growth that would otherwise influence SSTs later in September.

August 2025 mean SSTs were as high as ~12°C in parts of the Barents and Kara Seas (within the Arctic Ocean's Atlantic sector) with lower values of about –1°C to 7°C in other Arctic basin marginal regions (Figs. 5.12a,b). August 2025 mean SSTs were anomalously warm compared to the 1991–2020 August mean in the Barents, Kara, and Laptev Seas, with SST anomalies around +1°C to +4°C, and local SST anomalies as high as ~+7°C in the Kara Sea (Fig. 5.12c). In the Arctic's Pacific sector, the Beaufort and northern Chukchi Seas had anomalously cold SSTs (August 2025 mean values ~1°C–2°C lower than the 1991–2020 mean), while the southern Chukchi Sea and the Bering Sea were anomalously warm (SSTs ~1°C–2°C higher). This general pattern of August 2025 SST anomalies is consistent with regional patterns of anomalously warm surface air temperatures in the Kara and Laptev Sea regions and cold surface air temperatures in the Beaufort Sea region in summer 2025 (section 5c).

In most Arctic regions, August 2025 SSTs ranked among the warmest recorded in the 1982–2025 period (70th to 100th percentile; Fig. 5.12d), although regional SST anomalies differ significantly from year to year. The Kara and Chukchi Seas had considerably higher SSTs in August 2025 compared to August 2024, with differences of up to 9°C (Fig. 5.12e). By contrast, August 2025 SSTs were as much as a few degrees lower than 2024 SSTs in the Barents and southern Beaufort Seas.

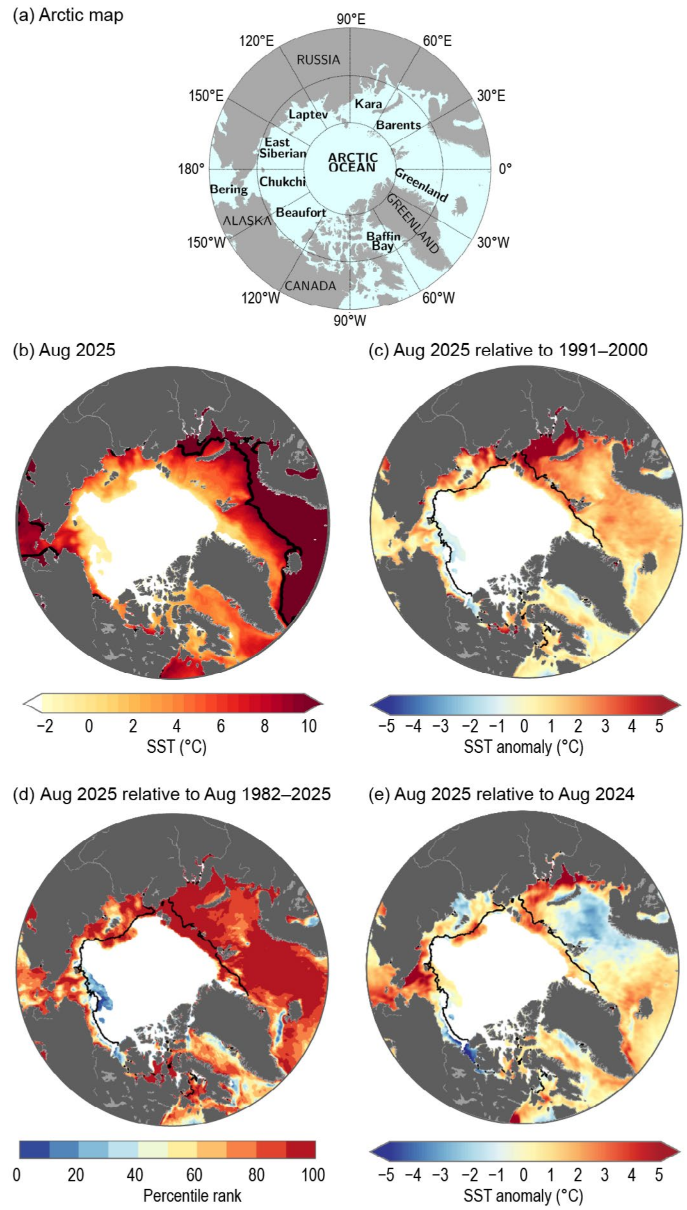

Fig. 5.12. (a) Arctic Ocean map showing relevant marginal sea locations and geographic features. (b) Mean sea surface temperature (SST; °C) in Aug 2025. Black contours indicate the 10°C-SST isotherm. (c) SST anomalies (°C) in Aug 2025 relative to the Aug 1991–2020 mean. (d) Aug 2025 SST percentile rank relative to the Aug values in 1982–2025. (e) Difference between Aug 2025 SSTs and Aug 2024 SSTs (negative values indicate where 2025 was cooler). White shading in all panels is the Aug 2025 mean sea ice extent. Black lines in (c)–(e) indicate the Aug 1991–2020 median ice edge. Sea ice concentration data are the (near-real-time) NOAA National Snow and Ice Data Center Climate Data Record of Passive Microwave Sea Ice Concentration, (version 4) version 6 (Meier et al. 2026a,b).

SST patterns in August 2025 followed developments in June and July. Above-normal SSTs in most of the Arctic's Atlantic sector were also observed in June and July 2025 (Figs. 5.13a,b). This is consistent with relatively warm summer 2025 surface air temperatures in the region (section 5c). Below-normal SSTs in the Bering Sea in June and July (Figs. 5.13a,b) were consistent with the relatively late sea ice retreat from the Pacific sector (section 5f). The transition from below-normal to above-normal SSTs from June to August in the Bering Strait region corresponded with the transition from anomalously cool surface air temperatures in spring to warm conditions in summer (section 5c). Anomalously cool SSTs across the Beaufort Sea sector in September (Fig. 5.13d) were consistent with the anomalously late ice retreat from the region (section 5f) and, consequently, a shorter duration of solar absorption by the surface ocean; surface air temperatures in September were near-normal or marginally above normal in the region (section 5c).

The Arctic Ocean has experienced significant mean August SST warming from 1982 to 2025, with statistically significant linear trends (95% confidence interval) in most regions (Fig. 5.14a). Mean August SSTs

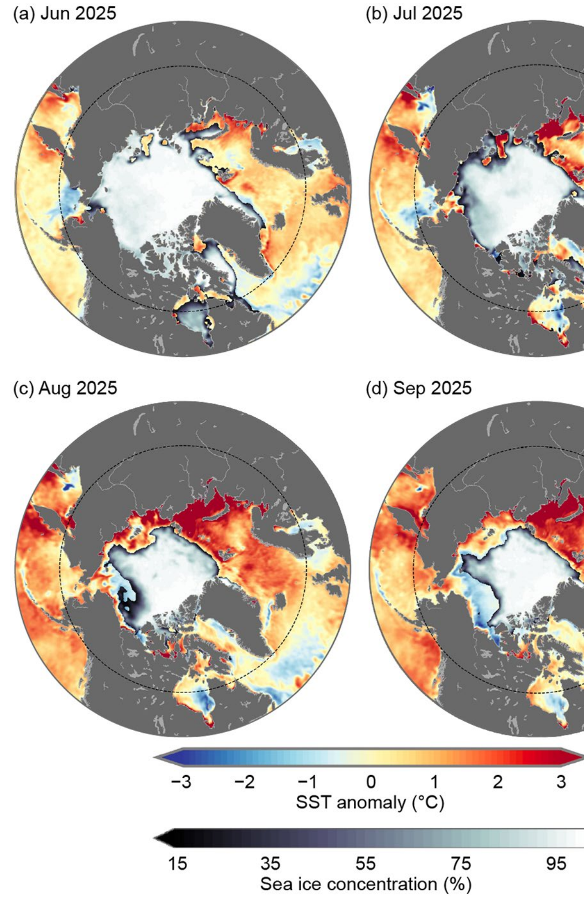

Fig. 5.13. Sea surface temperature (SST) anomalies (°C) in 2025 for (a) Jun, (b) Jul, (c) Aug, and (d) Sep relative to the 1991–2020 mean for their respective months. The dashed circle indicates the latitudinal bound of the maps in Fig. 5.12. Note a difference in the color bar scale compared to Figs. 5.12c,e. The mean sea ice concentration for the corresponding month is also shown. See Fig. 5.12 caption for sea ice dataset information.

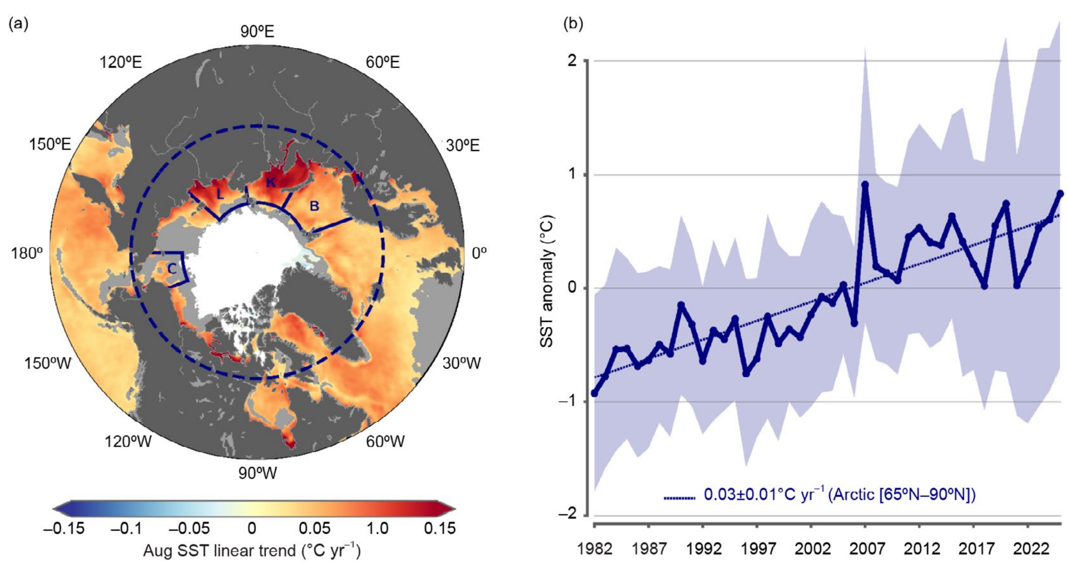

Fig. 5.14. (a) Linear sea surface temperature (SST) trend (°C yr^{-1}) for Aug of each year (1982–2025). The trend is only shown for values that are statistically significant at the 95% confidence interval; the region is shaded light gray otherwise. White shading indicates regions that are ice covered (>15% sea ice concentration) in all years. The dashed blue circle marks 65°N (the Arctic Ocean region), and solid blue line boundaries delineate the Barents (B; 66.5°N–80°N, 20°E–60°E), Kara (K; 70°N–80°N, 50°E–100°E), Laptev (L; 70°N–80°N, 100°E–139°E) and Chukchi (C; 65°N–75°N, 180°–202°E) Seas. (b) Area-averaged SST anomalies (°C) for Aug of each year from 1982 through 2025 relative to the 1991–2020 Aug mean for the Arctic Ocean north of 65°N (shading indicates ±1 std. dev. of the regional mean SST anomaly field). The dotted line shows the corresponding linear SST anomaly trend over the period 1982–2025, and numbers in the legend indicate the trend and 95% confidence interval.

for the entire Arctic Ocean region north of 65°N exhibit a linear warming trend of 0.3±0.1°C decade^{-1} (Fig. 5.14b). Within the long-term warming trend, the August 2025 mean Arctic Ocean SST was the second warmest on record, exceeded only by August 2007. Regionally, the Kara and Laptev Seas show the strongest warming trends in the Arctic Ocean (Fig. 5.14a), with August SST linear trends of 0.12±0.03°C yr^{-1} and 0.08±0.02°C yr^{-1}, respectively (Figs. 5.15a,b). In the Kara Sea, August 2025 mean SSTs were the highest on record. Statistically significant linear trends (0.06±0.02°C yr^{-1}) in August SST are also observed in the Barents Sea (Fig. 5.15c). On the other hand, there is no statistically significant trend in the Chukchi Sea (Fig. 5.15d). These regional differences in warming trends likely reflect varying sea ice loss patterns, ocean circulation, and atmospheric forcing across the Arctic basin.

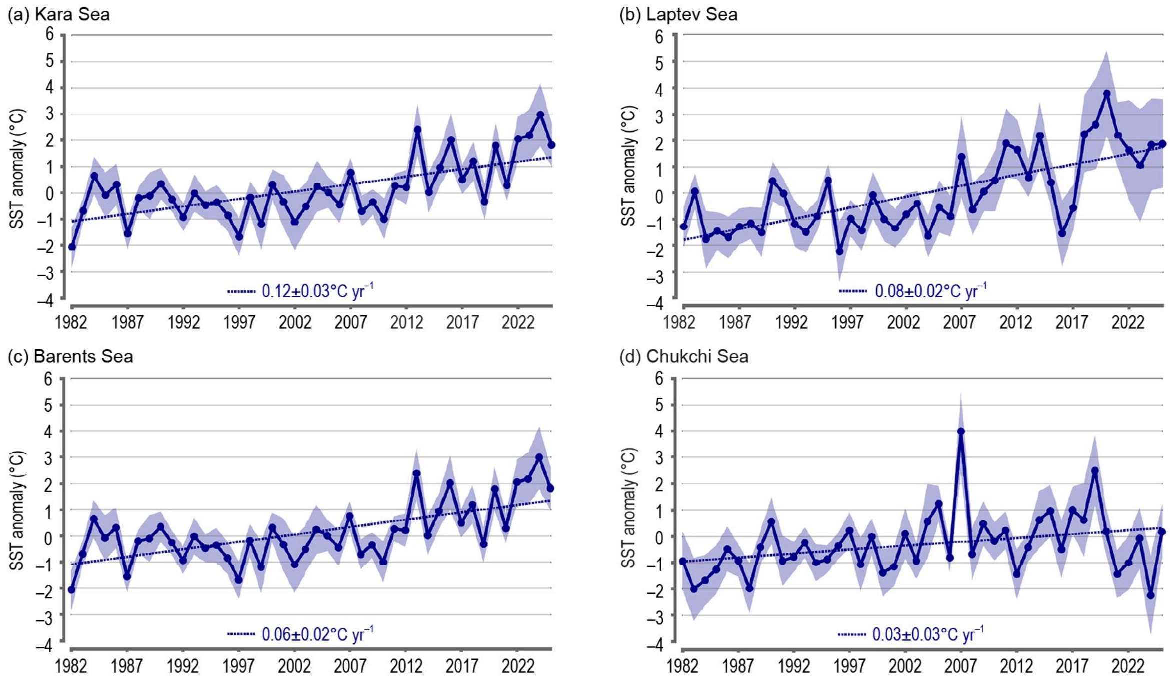

Fig. 5.15. Area averaged sea surface temperature (SST) anomalies (°C) for Aug of each year (1982–2025) relative to the 1991–2020 Aug mean for the (a) Kara Sea, (b) Laptev Sea, (c) Barents Sea, and (d) Chukchi Sea regions shown by the blue boundaries in Fig. 5.14a. The dotted lines show the linear SST anomaly trends over 1982–2025, and numbers in the legends indicate the trends in °C yr^{-1} (with 95% confidence intervals; trends that are not statistically significant are labeled in gray). Blue shading indicates ±1 std. dev. of the regional mean SST anomaly fields.

f. Sea ice cover

—W. N. Meier, S. Hendricks, A. Petty, D. Perovich, S. Farrell, M. Webster, D. Divine, S. Gerland, L. Kaleschke, R. Ricker, X. Tian-Kunze, and A. Bliss

Sea ice is the frozen interface between the ocean and atmosphere in the Arctic. It limits ocean–atmosphere exchanges of energy and moisture and plays a critical role in Arctic ecosystems and Earth's climate. The presence of sea ice affects human activities in the Arctic, including transportation, marine navigation, and Indigenous hunting. Arctic sea ice reached record monthly low extents during February, March, and December 2025. September sea ice extent, when the annual minimum usually occurs, has declined 46% over 1979–2025, though the trend over the past 20 years has been insignificant due to natural variability (England et al. 2025).

1. SEA ICE EXTENT AND CONCENTRATION

Arctic sea ice extent (defined as the total area covered by at least 15% ice concentration) in 2025 was generally on par with extents of the last 20 years but much lower than earlier decades within the observational record. For comparisons in this section, a climatological period of 1991–2020 is used. Extents during winter (January–March) 2025 were at record- or near-record-low levels (Fig. 5.16). Extent values are from the National Snow and Ice Data Center's Sea Ice Index (Fetterer et al. 2025), one of several extent products (Ivanova et al. 2014; Lavergne et al. 2019) derived from satellite-borne passive microwave sensors operating since 1979. Regionally, winter concentration was particularly below average in Hudson Bay (after a very slow freeze-up) and the Barents Sea, Bering Sea, Labrador Sea, and Sea of Okhotsk (Fig. 5.17).

By March, the month with the most extensive coverage, the total sea ice extent of 14.12×10^6 km^2 was 0.91×10^6 km^2 (6.1%) lower than average and the lowest March extent in the 47-year record. The March 2025 pan-Arctic extent continued the statistically significant downward trend of –2.5 % decade^{-1} over the 1979–2025 record.

After the record-low March extent, the seasonal retreat of sea ice began with much slower-than-normal ice loss through April. After April, ice loss increased and remained rapid through the rest of spring and early summer (mid-July). But after the beginning of August, the rate of sea ice loss slowed relative to 2024 and 2023 and was on par with the 1991–2010 average. As in 2024, Hudson Bay opened early in 2025, but it was not as extreme as in 2024. Summer ice loss was also particularly rapid in the Barents and Kara Seas.

In August, the Northern Sea Route, along the northern Russian coast, opened (<15% concentration in passive microwave data indicating the potential for safe navigation). Extent in the East Siberian Sea was near average, in contrast to the late opening that occurred in 2024. The Beaufort and Chukchi Seas were slow to open relative to 2024, but melted out

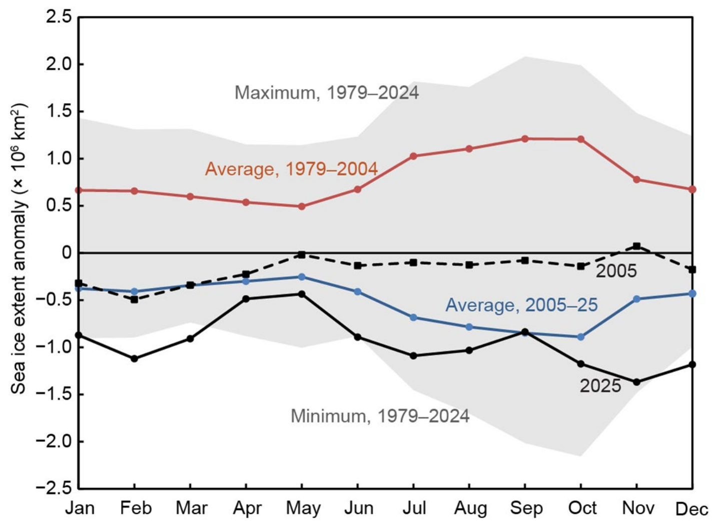

Fig. 5.16. Monthly average sea ice extent anomalies ($\times 10^6$ km^2) relative to 1991–2020 for: 2025 (black solid line), 2005 (black dashed line), 2005–24 average (blue), 1979–2004 average (red), and the maximum and minimum range (gray shading) for the period 1979–2024.

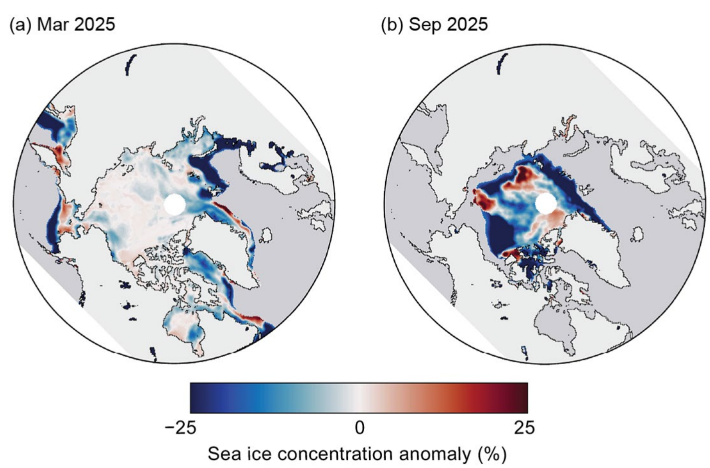

Fig. 5.17. Sea ice concentration anomalies (%) in 2025 for (a) Mar and (b) Sep relative to their 1991–2020 average. The extreme negative anomalies (darkest blue color, less than –25%) indicate regions where there is ice in the climatology, but no ice was present in 2025.

rapidly during August and September, yielding substantial open water that has been typical in nearly all years since 2007.

September, the month of the annual minimum sea ice extent, was characterized by below-average coverage in the Pacific sector with open water extending far northward from the coast in the Beaufort, Chukchi, and Siberian Seas (Fig. 5.17). The September 2025 sea ice extent of 4.75×10^6 km^2 was 0.83×10^6 km^2 (14.9%) lower than the 1991–2020 average and the 11th lowest September extent on record (Fig. 5.16). The September trend from 1979 through 2025 is –13.6% decade^{-1}, and like all other months, is statistically significant. The 19 lowest September extents in the satellite record have all occurred in the last 19 years (2007–25). The 2025 freeze-up period (October–December) was similar to 2024, with much lower-than-average extent in Hudson Bay and the Barents and Kara Seas.

2. SEA ICE AGE, THICKNESS, AND VOLUME

Sea ice drifts with winds and ocean currents while growing and melting thermodynamically. Ice divergence creates leads where, in freezing conditions, new ice forms while ice convergence leads to dynamic thickening. Sea ice thickness provides a record of the cumulative effect of dynamic and thermodynamic processes and thus is an important indicator of overall ice conditions. Sea ice age is a rough proxy for thickness as multiyear ice (ice that survives at least one summer melt season) grows thicker over successive winters. Age based on Tschudi et al. (2019a,b) covers the period 1984–2025, which is substantially longer than basin-wide thickness estimates, and shows that the amount of multiyear ice remaining in the Arctic continued to be far less than during the 1980s, with a substantial change even since 2005 (Fig. 5.18). Since 2012, the Arctic has been nearly devoid of the oldest ice (more than four years old); this continued in 2025, with an end-of-summer old ice extent of 95,000 km^2 compared to ~1.5×10^6 km^2 in the 1980s, a 95% reduction. In the 41 years since ice-age records began in 1984, the Arctic has changed from a region dominated by multiyear sea ice to one where first-year (seasonal) sea ice prevails. This much younger ice cover implies a thinner, less voluminous ice pack that is more sensitive to atmospheric and oceanic changes. For thickness estimates, the European Space Administration's (ESA) CryoSat-2/Soil Moisture Ocean Salinity (SMOS) satellites, in combination with the Copernicus Sentinel-3A/B satellites, have provided a record of seasonal (October–April) ice thickness and volume (Ricker et al. 2017; ESA 2023) since the 2010/11 winter. At the end of the winter growth season, the April 2025 thickness (Fig. 5.19a) in the Arctic had the typical pattern of thicker ice along the northern coast of Greenland and the Canadian Archipelago due to deformation and advection across the pole; this also corresponds to the region of older ice noted above. The thickness anomaly pattern for April 2025 shows a substantial amount of spatial variability (Fig. 5.19b). The 2024/25 sea ice growth season began with the Laptev, Kara, and Barents Seas having thicker ice than the 2010–21 average and other regions being thinner than average (Fig. 5.19c). Ice growth through the winter was robust, and by April 2025 all regions were either

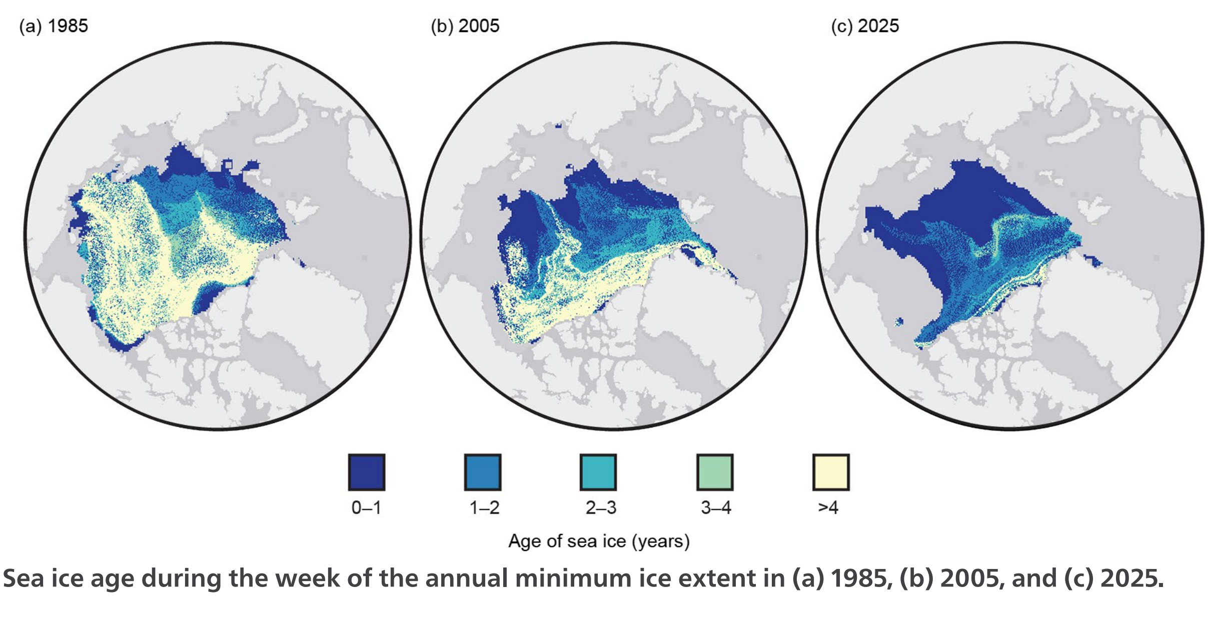

Fig. 5.18. Sea ice age during the week of the annual minimum ice extent in (a) 1985, (b) 2005, and (c) 2025.

average or thicker than the 2011–21 average; however, there were locations within some regions with thinner-than-average ice. By the start of the autumn freeze-up in October 2025, below-average thickness was prevalent in most regions, but by December 2025, most areas had thicker-than-average ice. Sea ice thickness from CryoSat-2/Sentinel-3/SMOS integrated with ice concentration shows no substantial trend in winter ice volume over the 15-year time series.

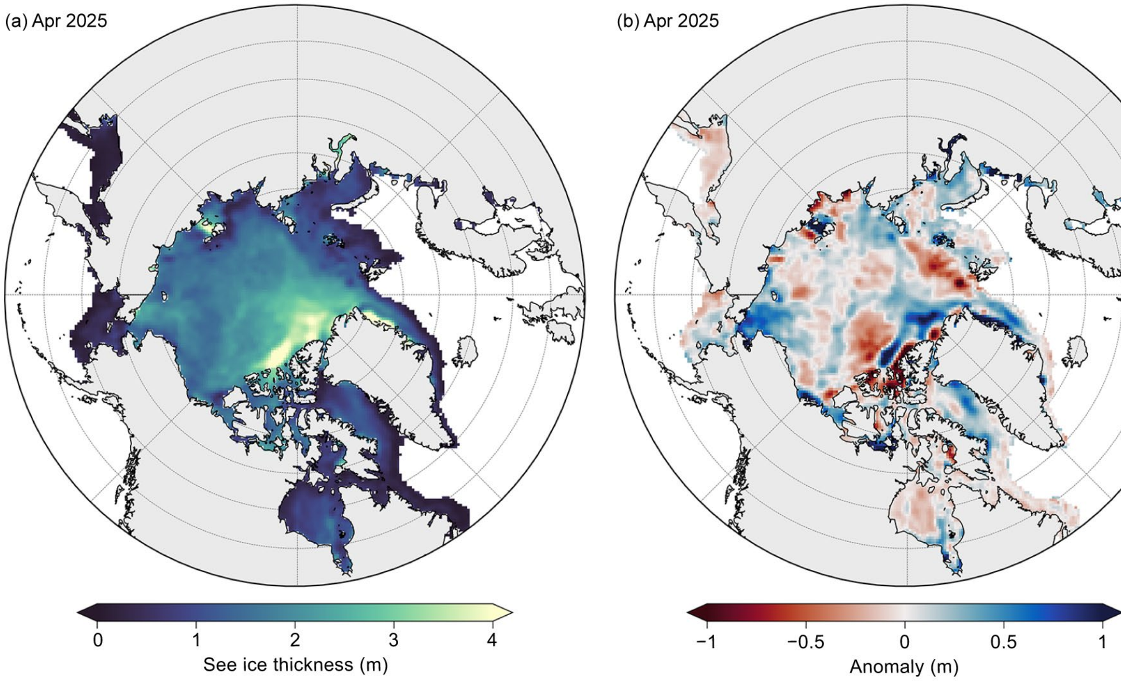

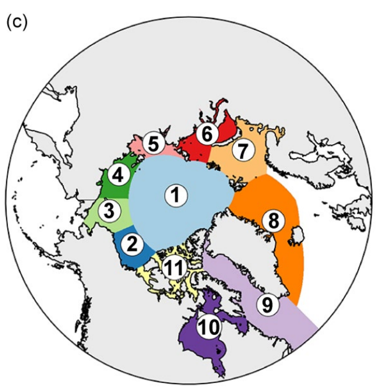

Location	Jan 2025	Feb 2025	Mar 2025	Apr 2025	Oct 2025	Nov 2025	Dec 2025
Central Arctic (1)	0.01 m	0.04 m	0.08 m	0.02 m	−0.06 m	−0.01 m	−0.04 m
Braufort Sea (2)	0.02 m	0.23 m	0.02 m	0.07 m	0.00 m	−0.01 m	0.07 m
Chukchi Sea (3)	0.06 m	0.30 m	0.45 m	0.32 m	0.17 m	0.14 m	0.13 m
East Siberian Sea (4)	−0.07 m	0.00 m	0.05 m	0.07 m	0.12 m	0.20 m	0.13 m
Laptev Sea (5)	0.00 m	0.08 m	0.11 m	0.03 m	0.02 m	0.03 m	0.11 m
Kara Sea (6)	0.09 m	0.18 m	0.21 m	0.28 m	0.22 m	0.08 m	0.07 m
Barents Sea (7)	0.21 m	0.27 m	0.29 m	0.20 m	0.42 m	0.44 m	0.33 m
East Greenland Sea (8)	−0.03 m	0.05 m	0.23 m	0.28 m	−0.05 m	0.03 m	0.13 m
Baffin Bay and Labrador Sea (9)	0.02 m	0.01 m	0.03 m	0.10 m	0.18 m	−0.03 m	−0.07 m
Hudson Bay (10)	−0.12 m	−0.05 m	0.00 m	0.00 m	0.02 m	−0.02 m	−0.03 m
Canadian Archipelago (11)	−0.10 m	−0.04 m	−0.02 m	0.00 m	−0.14 m	−0.11 m	−0.06 m

Fig. 5.19. Arctic sea ice in Apr 2025: (a) sea ice thickness (m), (b) sea ice thickness anomaly (m) relative to the Apr 2011–Apr 2021 average, and (c) regional monthly mean sea ice thickness anomalies (m) in 2025 relative to the Oct 2010–Apr 2021 average. (Source: European Space Administration's [ESA] CryoSat-2/Sentinel-3/Soil Moisture Ocean Salinity [SMOS].)

g. Greenland Ice Sheet

—K. Poinar, J. E. Box, T. L. Mote, X. Fettweis, B. D. Loomis, B. E. Smith, B. C. Medley, T. G. Askjaer, K. D. Mankoff, and R. S. Fausto

Net loss of ice from the Greenland Ice Sheet has occurred every year since the late 1990s (Mouginot et al. 2019; Mankoff et al. 2021), contributing to global sea level rise (see section 3f for details). Over the 2025 mass balance year (1 September 2024 to 31 August 2025), three independent estimates find that the ice sheet again lost mass, but at a rate ~30% less than the 1991–2020 average of roughly −200 Gt annually. These estimates are from input–output (−146±72 Gt), gravity (−129±50 Gt), and elevation (−143±36 Gt) methods; the values agree within measurement uncertainties.

The ice loss can be partitioned into ice discharge (iceberg calving) and surface mass balance (SMB). SMB is the sum of gain from snowfall and refrozen rainfall and loss from runoff, sublimation, and evaporation. Observations of air temperature, precipitation, snow cover, and albedo—key factors that influence SMB—over the 2025 mass balance year are summarized here.

Air temperatures were generally higher than the 1991–2020 average, especially in northern Greenland (Fig. 5.20a). Autumn (September–November 2024) and winter (December–February 2024/25) temperatures were above average, and spring (March–May 2025) brought pronounced warmth across Greenland, with record monthly highs set at 6 out of 34 stations. Summer (June–August 2025) was slightly cooler than average, except in mid-August, when a heatwave raised temperatures, primarily along the west coast.

Observations of rain and snowfall (hereafter, "precipitation") are reported for 11 coastal stations operated by the Danish Meteorological Institute (DMI) and 10 inland ice sheet stations operated by the Programme for Monitoring of the Greenland Ice Sheet (PROMICE). Precipitation at coastal stations was generally above the 1991–2020 average. Autumn 2024 precipitation was slightly below average at most stations, while winter precipitation was significantly above average at coastal stations but near-average at inland stations. Spring precipitation was close to average. Summer precipitation was above average, including notable snowfall at several inland

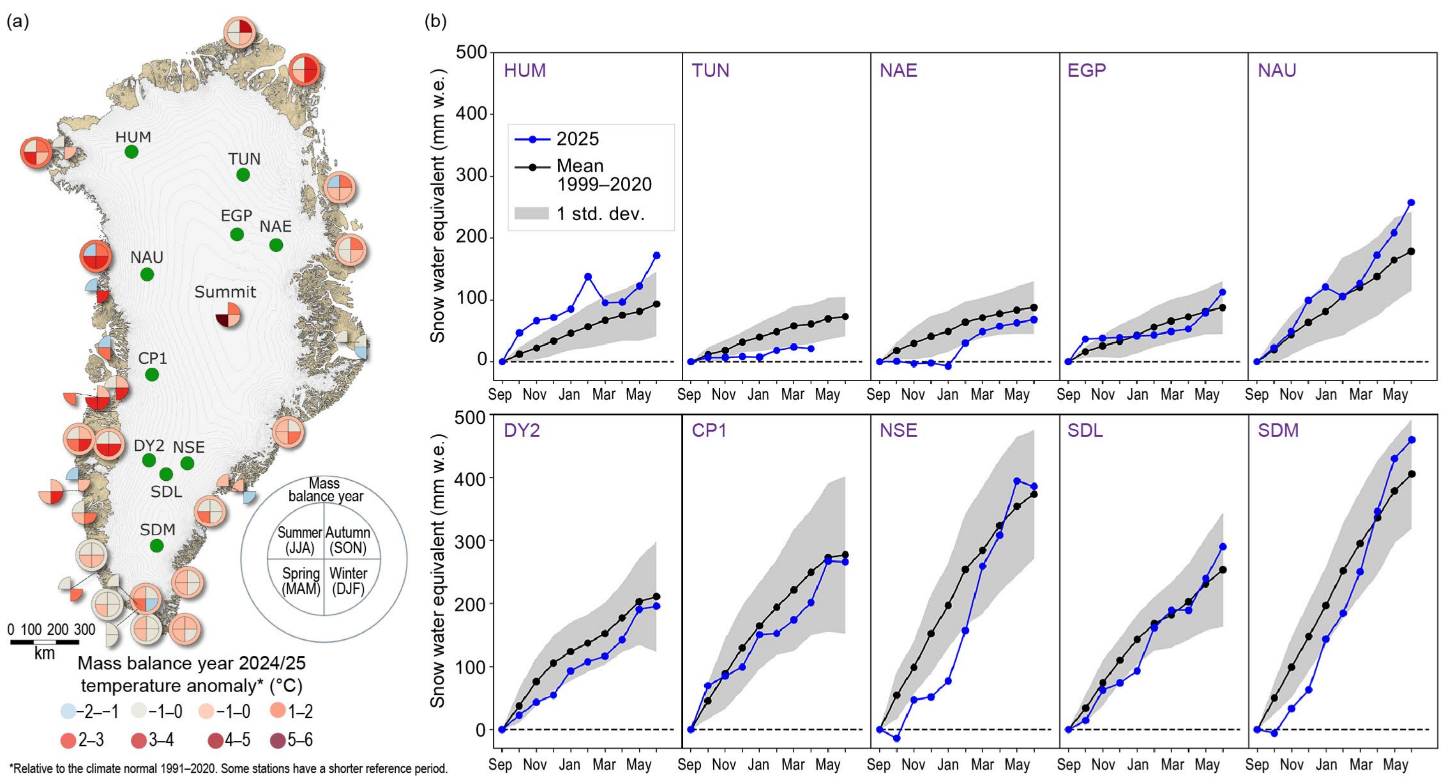

Fig. 5.20. (a) Map of Danish Meteorological Institute (DMI) coastal weather stations, colored by the temperature anomaly (°C) for each season (pie charts) and the full 2025 mass balance year (surrounding circles). Locations of inland weather stations operated by the Programme for Monitoring of the Greenland Ice Sheet (PROMICE) are indicated by green dots. (b) Snowfall (mm w.e.) at PROMICE stations from Sep 2024 through Jun 2025 (blue lines), compared to the 1991–2020 mean (black lines).

stations in June, July, and early August (Fig. 5.20b). Snow cover raises the albedo (surface reflectivity) of the ice sheet surface, so these events likely reduced ice melt by reflecting away sunlight.

Ice ablation (melt) was recorded across eight weather transects from PROMICE (Fausto et al. 2021) and also derived from daily Special Sensor Microwave Imager/Sounder (SSMIS) passive microwave radiometer satellite data (Mote 2007). Surface melt area was above average in mid-June and mid-July, and the 14–21 August heatwave caused widespread melt (Fig. 5.21a). While the number of observed melt days was slightly above average (Fig. 5.21b), the total mass of ice melt was below average, especially along the west coast, due to higher-than-normal albedo and cooler air temperatures there (Fig. 5.20).

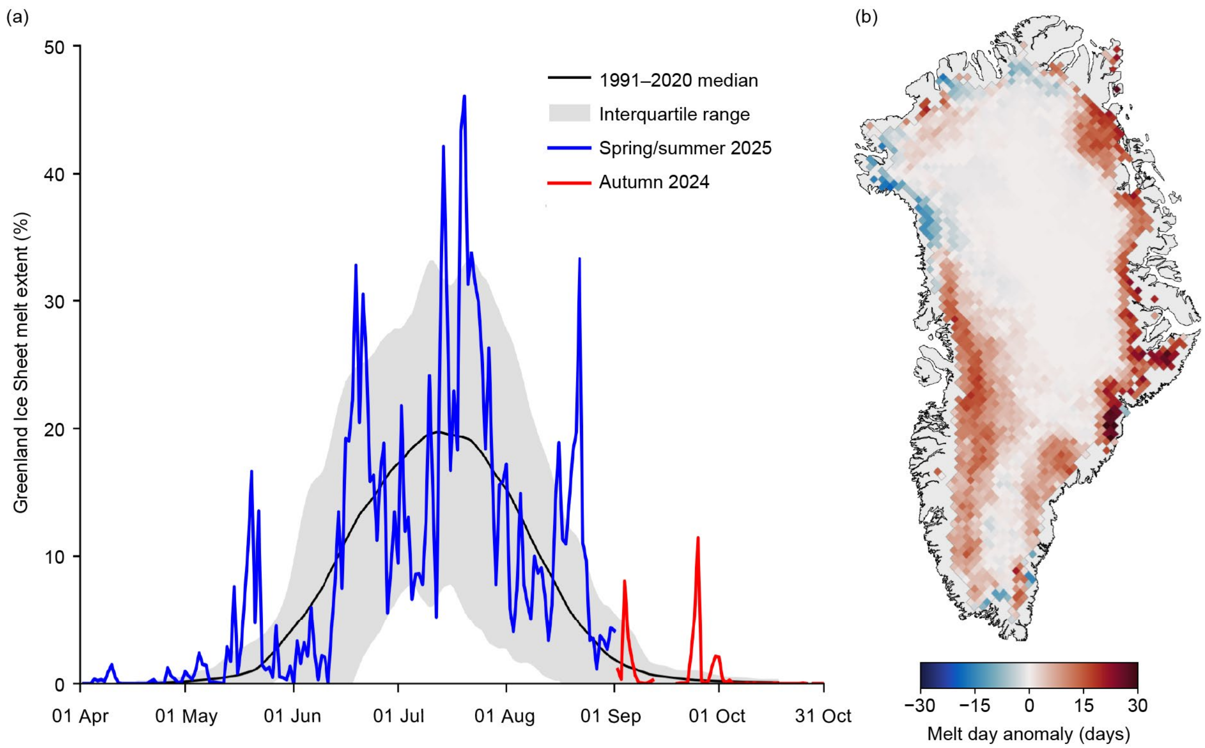

Fig. 5.21. (a) Daily surface melt extent as a percentage (%) of ice sheet area over the 2025 mass balance year, including autumn 2024 (red) and spring/summer 2025 (blue) but omitting Nov 2024–Mar 2025. (b) Number of surface melt days from 1 Apr to 31 Aug 2025 as an anomaly with respect to 1991–2020.

The ice-sheet-wide total SMB over the 2025 mass balance year was 365±55 Gt, which is consistent with the 1991–2020 annual mean of 366±106 Gt (mean ±1 st. dev), from the Modèle Atmosphérique Régionale version 3.14.1 regional climate model (MAR; Fettweis et al. 2020) forced by ERA5 (Hersbach et al. 2020), which provides SMB values at 5-km horizontal resolution.

The other term in ice-sheet mass balance is ice discharge, which is the mass flow rate out of glaciers at the ice–ocean boundary, where it calves off as icebergs or melts directly into the ocean. PROMICE estimates ice discharge from mass flow rate measurements collected near glacier fronts around the ice sheet (Mankoff et al. 2020). Total ice discharge over the 2025 mass balance year was 488±46 Gt, approximately 1 std. dev. above the 1991–2020 annual mean of 458±27 Gt (mean ±1 std. dev).

Ice discharge (488±46 Gt output) and basal melt (23±6 Gt output; Karlsson et al. 2021) are subtracted from the net SMB (365±55 Gt input) to obtain an input–output mass balance of –146±72 Gt over the 2025 mass balance year (Fig. 5.22). This is consistent with the average input–output-derived annual mass balance over 1991–2020 of –156±80 Gt (mean ±1 std. dev). While the input–output figure is close to the climatologic average, the other two methods find below-average mass loss in 2025.

The Gravity Recovery and Climate Experiment Follow-on (GRACE-FO) satellite mission detects gravity anomalies over time to measure changes in total ice mass (Tapley et al. 2019). After eliminating peripheral ice from these observations (Colgan et al. 2015), this gravity-based method measures a 2025 mass balance of –129±50 Gt (Fig. 5.22). This is 50% less than the average annual mass balance measured by GRACE/GRACE-FO over 2002–24 of –256±135 Gt yr^{-1} (mean ±1 std. dev.).

The Ice, Cloud, and land Elevation Satellite-2 (ICESat-2) mission measures the surface elevation change of the ice sheet over time, which is converted to mass change (Smith et al. 2023; Medley et al. 2022; Smith 2023). This elevation-based method measured a 2025 mass balance of –143±36 Gt (Fig. 5.22), consistent with the ICESat-2 annual average over 2020–24 of –143±51 Gt (mean ±1 std. dev.).

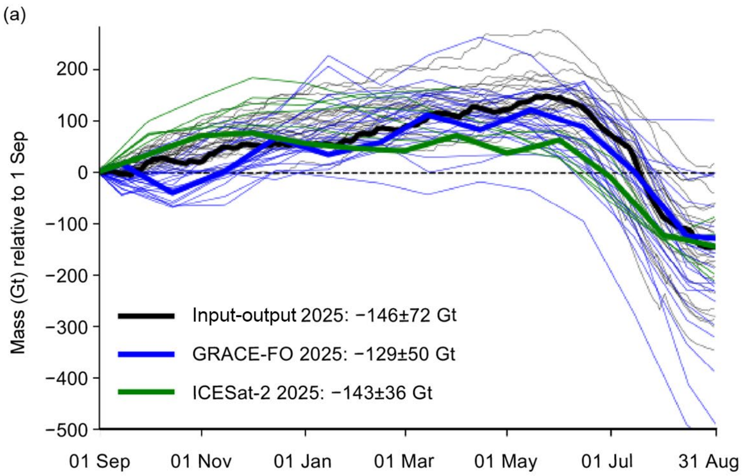

Fig. 5.22. (a) Mass balance (Gt) of the Greenland Ice Sheet over the 2025 mass balance year from the input–output method (thick black line), the Gravity Recovery and Climate Experiment Follow-On (GRACE-FO; thick blue line), and Ice, Cloud, and land Elevation Satellite-2 (ICESat-2; thick green line), with previous years (2003–24) in lighter thin lines. (b) Histogram of multi-method annual average mass balance in years from 2003 to 2024, with 2025 results from each method (by color) horizontally offset for visibility.

h. Glaciers and ice caps outside Greenland

—G. Wolken, D. Burgess, B. Wouters, L. M. Andreassen, C. Florentine, J. Kohler, B. Luks, F. Pálsson, L. Sass, L. Thomson, and T. Thorsteinsson

The Arctic represents approximately 60% of the global mountain glacier and ice cap area, excluding the Greenland and Antarctic ice sheets (RGI Consortium 2023; Fig. 5.23). Although their long-term sea level rise potential is smaller than that of the Greenland and Antarctic ice sheets, Arctic glaciers and ice caps respond more rapidly to climate variability and have been major contributors to recent sea level rise under sustained atmospheric warming (The GlaMBIE Team 2025).

Amid amplified warming at high northern latitudes (section 5c), annual mass loss from Arctic glaciers and ice caps has tripled since the mid-1990s (Zemp et al. 2019). While in situ data for the balance year 2024/25 (October 2024 to September 2025) are not yet available, observations from 2022/23 and 2023/24 reveal pronounced regional and interannual variability, even as the long-term trend continues with widespread and substantial ice loss.

Mass change in glaciers and ice caps reflects the balance between inputs, primarily snow accumulation, and outputs, including surface melt and runoff, as well as iceberg calving from tidewater- or lake-terminating glaciers. The net (total) mass balance is the difference between these processes. This assessment of 27 monitored Arctic glaciers excludes calving losses, which occur only at Kongsvegen, Hansbreen, and Devon Ice Cap (Table 5.1; Fig. 5.23). We therefore report climatic mass balance (B_{clim}): the difference between annual snow accumulation and annual runoff, expressed as mean annual thickness change (mm water equivalent, w.e.) averaged over the glacier or ice cap surface.

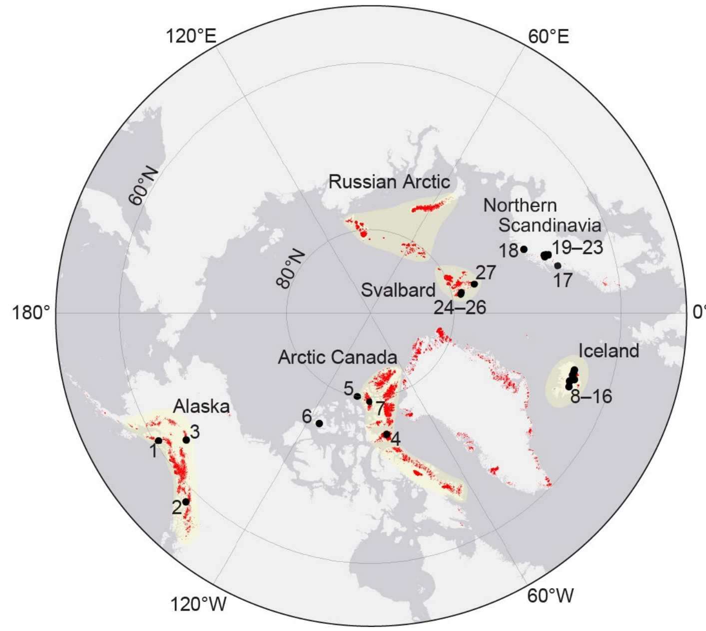

Fig. 5.23. Arctic glaciers and ice caps (red), including ice caps in Greenland that are separate from the ice sheet. Yellow shaded regions delineate the Gravity Recovery and Climate Experiment (GRACE)- and GRACE-Follow On (GRACE-FO)-derived mass anomaly domains used to estimate changes in annual glacier mass balance for heavily glacierized Arctic regions (Watkins et al. 2015; Landerer et al. 2020). Black dots indicate the 27 long-term Arctic glacier monitoring sites, with numbers linked to the glacier/ice cap names in Table 5.1. (Source: ESRI 2026.)

In balance year 2023/24, all 25 glaciers with available data (2 of the 27 lacked observations) registered negative mass balances, consistent with 2022/23 (Table 5.1; WGMS 2025). Although Alaska, Arctic Canada, and Iceland experienced negative anomalies in 2022/23, with melt increases of 27%, 112%, and 115%, respectively, melt was lower (positive anomalies) in 2023/24 relative to the 1991–2020 mean.

Losses were most extreme in Arctic Scandinavia and Svalbard, where land ice has declined sharply since 2021. Both regions recorded their most negative mass balance year on record in 2023/24 (Kjøllmoen et al. 2025; Schuler et al. 2025), with melt averaging 1473% above the 1991–2020 mean in Arctic Scandinavia and 472% above in Svalbard. This enhanced melt coincided with a persistent warm air mass over northern Scandinavia and the Barents Sea that produced record-high seasonal temperatures since the start of the record in 1950 (Ballinger et al. 2024).

The substantial scale of thinning is evident in individual glacier records. In Arctic Scandinavia, Langfjordjøkelen, and Engabreen saw their climatic mass balances decline from –1651 mm w.e. and –1101 mm w.e. in 2022/23 to –4060 mm w.e. and –3900 mm w.e. in 2023/24, respectively. In Svalbard, Midtre Lovénbreen and Austre Brøggerbreen shifted from –975 mm w.e. and –948 mm w.e. to –1968 mm w.e. and –2042 mm w.e. over the same period.

Table 5.1. Measured climatic mass balance (B_{clim}) for 27 glaciers in Alaska (3), Arctic Canada (4), Iceland (9), Arctic Scandinavia (7), and Svalbard (4): 1991–2020 mean value and standard deviation, 2022/23 value, and 2023/24 value, for each of the monitored glaciers (* indicates one or more years of data missing from the record; – indicates no data reported). Negative (positive) values for B_{clim} indicate mass loss (gain). Numbers listed in the Region column correspond to glacier locations in Fig. 5.23. Data were obtained from the World Glacier Monitoring Service (WGMS 2025) with updates from the Norwegian Water Resources and Energy Directorate (NVE) and Geological Survey of Canada. Bias corrections were applied to B_{clim} for Hofsjökull glaciers (N, E, and SW), Iceland using methods outlined in Jóhannesson et al. (2013). Regional climatic mass balances were derived as arithmetic means for all monitored glaciers within each region for each year, and these means were summed over the period of record and interpreted as cumulative mass balance changes in mm w.e.

Region	Glacier (record length, years)	B_{clim} Mean (w.e. yr^{-1}) *1991–2020*	B_{clim} Std. dev. (w.e. yr^{-1}) *1991–2020*	B_{clim} (w.e. yr^{-1}) *2022/23*	B_{clim} (w.e. yr^{-1}) *2023/24*
(1) Alaska	Wolverine (59)	–766	984	–1050	–650
(2) Alaska	Lemon Creek (72)	–1196	839	–2310	–1070
(3) Alaska	Gulkana (59)	–769	816	–400	–400
(4) Arctic Canada	Devon Ice Cap (64)	–257	215	–377	–290
(5) Arctic Canada	Meighen Ice Cap (65)	–326	432	–615	–198
(6) Arctic Canada	Melville S. Ice Cap (62)	–458	484	–1482	–300
(7) Arctic Canada	White (62)	–355	323	–653	–321
(8) Iceland	Langjökull S. Dome (28)	–1248	842*	–1430	–1005
(9) Iceland	Hofsjökull E (36)	–980	840	–1210	–580
(10) Iceland	Hofsjökull N (37)	–824	706	–1070	–730
(11) Iceland	Hofsjökull SW (36)	–956	951	–690	30
(12) Iceland	Köldukvislarjökull (33)	–467	708	–740	–80
(13) Iceland	Tungnaarjökull (33)	–1142	781*	–1529	–1370
(14) Iceland	Dyngjujökill (27)	–44	792*	–308	–50
(15) Iceland	Brúarjökull (32)	–238	622	–713	–60
(16) Iceland	Eyjabakkajökull (33)	–700	766*	–1417	–510
(17) Arctic Scandinavia	Engabreen (55)	–62	972	–1101	–3900
(18) Arctic Scandinavia	Langfjordjøkelen (34)	–953	771*	–1651	–4060
(19) Arctic Scandinavia	Marmaglaciaren (34)	–494	568*	–1256	–2573
(20) Arctic Scandinavia	Rabots (41)	–533	648*	–1565	–2804
(21) Arctic Scandinavia	Riukojietna (36)	–701	734*	–1347	–3458
(22) Arctic Scandinavia	Storglaciaren (79)	–235	747	–812	–2846
(23) Svalbard	Tarfalaglaciaren (20)	–331	1170*	–	–
(24) Svalbard	Midtre Lovénbreen (57)	–495	406	–975	–1968
(25) Svalbard	Austre Brøggerbreen (58)	–612	444	–948	–2042
(26) Svalbard	Kongsvegen (38)	–143	397	–673	–1410
(27) Svalbard	Hansbreen (33)	–419	470*	–	–

Data from 2023/24 further confirm the sustained, multi-decadal pattern of surface mass loss across the Arctic (Fig. 5.24). Since 1953, Alaska has seen the most significant cumulative thinning, with an area-averaged loss of −38 m w.e. It is followed by Arctic Scandinavia (1946) at −32 m w.e., while Iceland (1988) and Svalbard (1967) recorded losses of −29 m w.e and −27 m w.e., respectively. Arctic Canada (1960) follows with −16 m w.e. The persistence and scale of these mass losses emphasize the strong sensitivity of Arctic glaciers to climate warming and their ongoing contribution to sea level rise (Box et al. 2018).

Arctic glaciers and ice caps have been increasingly important contributors to global sea level rise since the early 1990s, but preliminary data for the 2024/25 balance year indicate that some Arctic glaciers may have shifted into net mass gain during that balance year (Fig. 5.25). Gravity anomalies from the combined The Gravity Recovery and Climate Experiment (GRACE; 2002–16) and GRACE Follow-On (GRACE-FO; 2018–25) missions indicate that Pan-Arctic glaciers and ice caps have lost mass at a rate of −178±21 Gt yr^{-1} over the full 2002–25 observational period, but mass gains in 2024/25 of 114.13±19 Gt break the pattern of sustained loss observed since 2011/12. This positive anomaly is driven primarily by regional mass gains in Alaska, Iceland, and Arctic Canada, which together outweigh the ongoing mass losses from Arctic Russia and Svalbard.

Although these initial findings remain subject to revision, Alaska was a key contributor to the 2024/25 Pan-Arctic mass gain, accounting for 97.84±37 Gt (~52.6%). This was followed by Arctic Canada at 74.32±20 Gt (~40.0%), and Iceland at 13.69±9 Gt (~7.4%). In contrast, Arctic Russia lost 52.36±17 Gt of mass (~73.0% of the Pan-Arctic mass loss), while Svalbard lost 19.36±12 Gt (~27.0%). These regional totals indicate that even during a year of overall Pan-Arctic mass gain, certain regions remain in a state of sustained retreat, reflecting the heterogeneous response of Arctic glacier systems to climate forcing.

Despite regional variability, glaciers in the Arctic are experiencing a consistent trend of cumulative mass loss. The continued loss of glacier and ice cap mass across the Arctic can be a primary indicator of climate change and societal risk (Wolken et al. 2021). The impacts of ice loss extend far beyond the cryosphere, ranging from diminishing late-season water

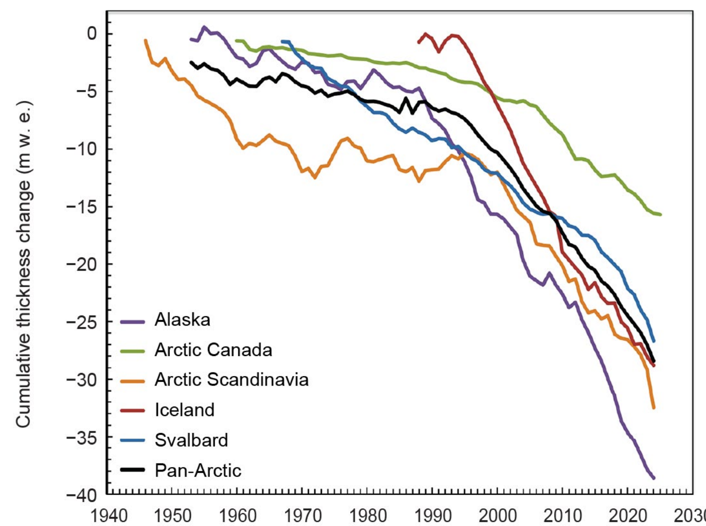

Fig. 5.24. Cumulative mass change (B_{clim}) expressed as thickness change in meters of water equivalent (m w.e.) for 27 monitored glaciers in five Arctic regions and for the Arctic as a whole (Pan-Arctic mean). Note the variable time periods over which cumulative changes are measured.

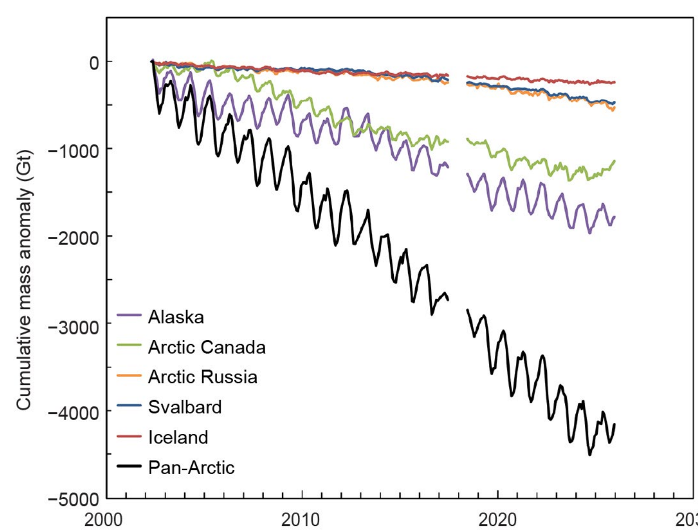

Fig. 5.25. Cumulative changes in regional total stored water (Gt) from 2002 to 2025 derived from Gravity Recovery and Climate Experiment (GRACE) and GRACE-Follow On (GRACE-FO) satellite gravimetry for the five regions shown in Fig. 5.23 and for the total of these five regions (Pan-Arctic). A Jul 2017–May 2018 data gap exists between retrieval periods. The data processing involved several steps. First, common post-corrections to the Level-2 data were applied, including the addition of degree-1 coefficients which are not directly observed by the satellites, and a correction for mass redistribution due to glacial isostatic adjustment (Wouters et al. 2019). A 150-km Gaussian smoothing filter was applied to the resulting Stokes coefficients for further noise reduction. Finally, to retrieve the mass changes for the glacier regions, the processed coefficients were converted into maps of equivalent water height anomalies using a mass concentration approach based on a global 0.5° × 0.5° grid.

supplies in communities like Ausuiktuq (Grise Fiord, Canada) to intensifying geohazards in Alaska. Examples of the latter include recurrent glacial lake outburst floods at Mendenhall Glacier and a large landslide at South Sawyer Glacier in Alaska's Tracy Arm fjord (Kienholz et al. 2020; USGS 2025). As Arctic warming persists, interconnected effects, from global sea level rise to local threats to infrastructure, public safety, and water security, highlight that these sustained observations can improve hazard assessment and support community-centered adaptation throughout the region.

i. Terrestrial snow

—L. Mudryk, A. Elias Chereque, C. Derksen, K. Luojus, and B. Decharme

Many components of the Arctic land surface are directly influenced by the presence and amount of snow cover. Reductions in snow cover directly contribute to amplified warming in the Arctic, while also affecting permafrost deterioration and ecosystem health (Brown et al. 2017; Meredith et al. 2019; Jones et al. 2011). Even following the snow cover season, the influence of spring snowmelt timing persists through impacts on river discharge timing and magnitude, surface water, soil moisture, vegetation phenology, and fire risk (Meredith et al. 2019).

Snow cover extent (SCE) anomalies from 1967 to 2025 are illustrated for both the North American and Eurasian sectors of the Arctic in Fig. 5.26 (relative to the 1991–2020 baseline; data from the NOAA Climate Data Record of Northern Hemisphere SCE; Robinson et al. 2012). In 2025, Arctic SCE was close to normal across both the Eurasian and North American sectors during May but dropped below normal by June (13th and 6th lowest by sector, respectively, in the 59-year record). Arctic snow cover extent during May and June has reduced by 15% and 50%, respectively, since 1967 (Mudryk et al. 2025), and these springtime reductions contribute substantially to an overall reduction in annual snow cover duration.

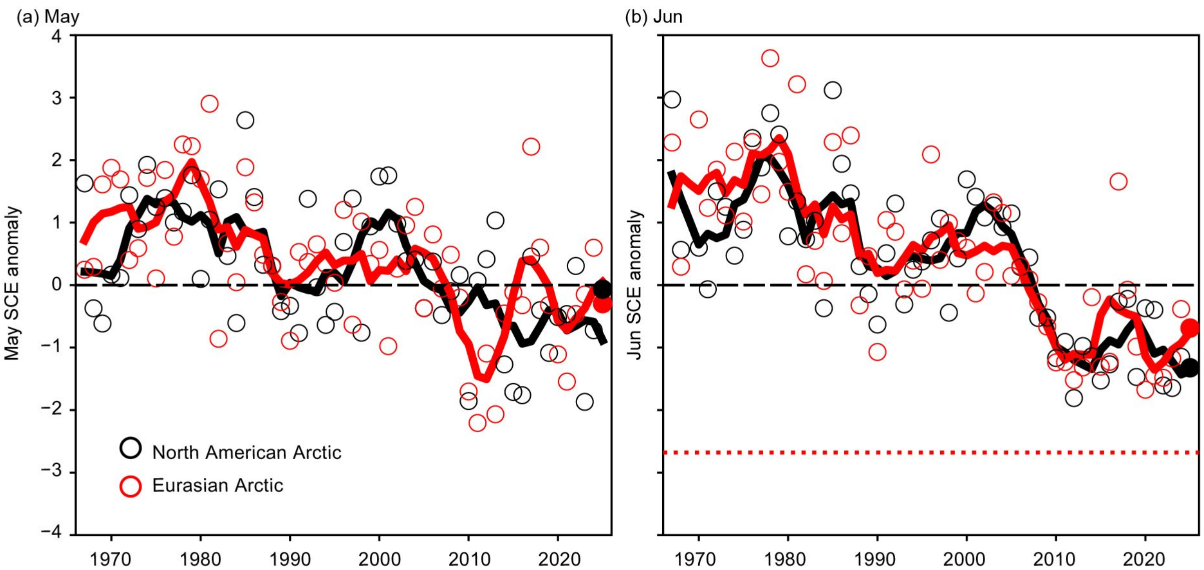

Fig. 5.26. Monthly Arctic snow cover extent anomalies for Arctic terrestrial land areas (poleward of 60°N) for (a) May and (b) Jun from 1967 to 2025 for the Eurasian (red circles) and North American (black circles) sectors. Filled circles highlight 2025 anomalies. Anomalies are relative to the 1991–2020 average and standardized (each observation differenced from the mean and divided by the standard deviation, and thus unitless). Solid black and red lines depict five-year running means for North America and Eurasia, respectively. The dotted red line illustrates the anomaly value representing zero SCE across Eurasia during Jun. The corresponding value for North America is below the plotted range at –5.4. (Source: Robinson et al. 2012.)

Snow cover duration (SCD) anomalies in 2025 are shown in Fig. 5.27 (data from the NOAA daily Interactive Multisensor Snow and Ice Mapping System [IMS] snow cover product; U.S. National Ice Center 2008). The maps illustrate the spring "melt period" at the end of the 2024/25 snow season (using data from February 2025 to July 2025; Fig. 5.27a) as well as the autumn "onset period" of the following 2025/26 snow season (using data from August 2025 to January 2026; Fig. 5.27b). Combining these periods describes the length of the snow-free period during summer 2025 (Fig. 5.27c). Snow melt timing in spring 2025 was earlier than normal over northern Europe and eastern Siberia, but later than normal over the intervening Arctic region (Ural and central Siberian regions). Across the North American Arctic, melt was later than normal over the western parts of the region but earlier than normal over the central and eastern parts. In autumn 2025, snow onset was later than normal in western Eurasia and earlier than normal in eastern Eurasia. Across North America, snow onset was earlier than normal in the northernmost Arctic and parts of Alaska but later than normal over the southern Canadian Arctic. For the regions of western Eurasia and the southern Canadian Arctic, earlier melt in spring and late onset in autumn combined to produce one of the longest summer snow-free periods in the available record (Fig. 5.27c).

Finally, snow water equivalent (SWE), a measure of snowpack amount, is used to characterize Arctic snow accumulation over the 2024/25 season. Maps of SWE anomalies are shown in Fig. 5.28 for April–June 2025. In April, the majority of Arctic land areas on both continents had positive SWE anomalies, indicating higher-than-normal snowfall accumulations since the preceding autumn (April is the approximate month that total snow mass across the terrestrial pan-Arctic region peaks before increasing temperatures in May and June lead to melt). The higher-than-normal SWE anomalies over much of the Arctic in May were aligned with near-normal SCE also seen during May. The exception to higher-than-normal SWE are the low values found in both April and May over parts of northern Europe and subarctic regions farther south, consistent with the earlier-than-normal spring melt timing across the same regions (Fig. 5.27a). By June, the SWE across much of the rest of Eurasia was also gone, consistent with lower-than-normal June SCE anomalies (Fig. 5.26). For North America during June, the western portion of the Canadian Arctic Archipelago had strongly above-normal SWE, while in the eastern portion and Baffin Island SWE was below normal.

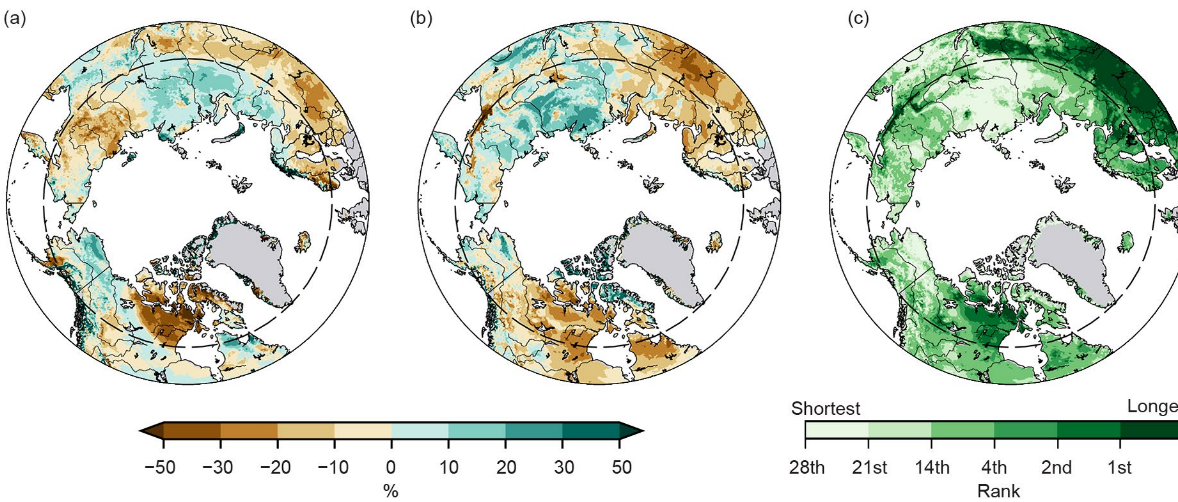

Fig. 5.27. Snow cover duration (SCD) anomalies (% difference relative to climatological number of snow-free days for the 1998/99–2022/23 baseline): (a) spring snow melt (Feb–Jul 2025) and (b) autumn snow onset (Aug 2025–Jan 2026). In both (a) and (b), brown (blue) indicates decreases (increases) in the number of days with snow cover. In (a) these changes are aligned with earlier (later) melt at the end of the snow season while in (b) these changes are aligned with a later (earlier) start to the snow season. Ranks in (c) illustrate how the duration of the summer 2025 snow-free period varied over the Arctic. The dashed circle marks the latitude 60°N. (Source: U.S. National Ice Center 2008.)

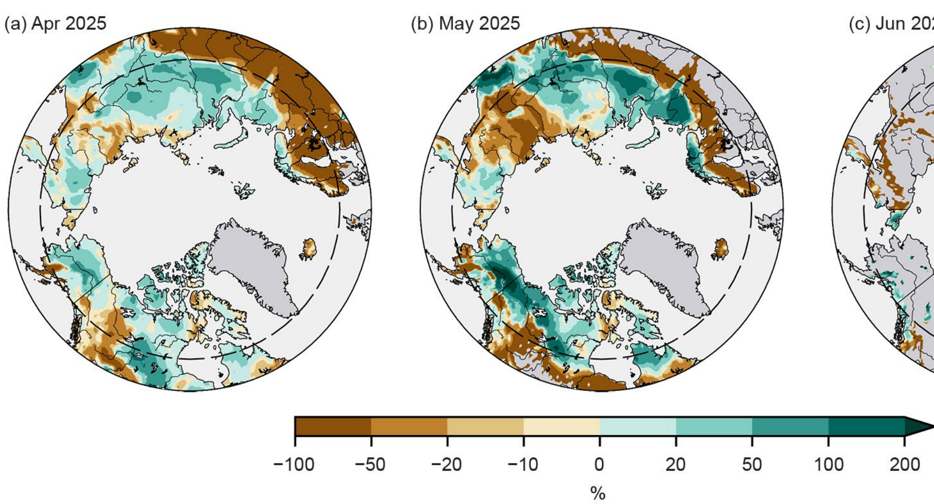

Fig. 5.28. Snow water equivalent (SWE) anomalies (% difference from the 1991–2020 baseline) in 2025 for (a) Apr, (b) May, and (c) Jun. Brown (green) indicates lower (higher) snow amounts than average. Latitude 60°N is marked by the black dashed circle. (Source: Selection of four SWE products from Snow Climate Change Initiative [CCI]; Luojus et al. 2022; MERRA-2 [GMAO 2015]; ERA5-Land [Muñoz Sabater 2019]; and Crocus-ERA5 [Decharme et al. 2024].)

j. Terrestrial permafrost

—S. L. Smith, V. E. Romanovsky, K. Isaksen, K. E. Nyland, D. A. Streletskiy, and H. H. Christiansen

Permafrost refers to earth materials (e.g., bedrock, mineral soil, organic matter) that remain at or below 0°C for at least two consecutive years, although most permafrost has existed for centuries to many millennia. Extensive regions of high-latitude landscapes are underlain by permafrost. The active layer, which thaws and refreezes annually, overlies the permafrost. Warming of permafrost, active layer thickening, and ground ice melt cause changes in surface topography, hydrology, and landscape stability, with implications for Arctic infrastructure, ecosystem integrity, and human livelihoods (Hjort et al. 2022; Smith et al. 2022; Burn et al. 2025). Changes in permafrost conditions also affect the rate of greenhouse gas release to the atmosphere, potentially accelerating global warming (Miner et al. 2022; Schuur et al. 2022).

Permafrost conditions respond to shifts in the surface energy balance through interrelated changes in ground temperature and active layer thickness (ALT). Ground temperatures fluctuate seasonally near the surface, while below the depth of seasonal temperature variation, they reflect longer-term climate. Long-term changes in permafrost temperatures are driven by changes in air temperature but also are influenced by local variability in snow cover, vegetation characteristics, and soil moisture (Romanovsky et al. 2017; Smith et al. 2022). Monitoring sites across the Arctic (Fig. 5.29) have recorded ground temperature in the upper 30 m for up to five decades, providing critical data on changes in permafrost conditions. Observed changes in ALT are more reflective of shorter-term (year-to-year) influences and are especially sensitive to changes in summer air temperature and precipitation.

Since the 1980s, permafrost temperatures have continued to increase on a decadal scale across the Arctic. Greater increases are generally observed in colder permafrost (temperature <–2°C) at higher latitudes (Smith et al. 2022, 2025; see also section 2c1), partly due to greater increases in air temperature (Figs. 5.29, 5.30). Positive ALT trends over the last 30 years (Fig. 5.31) are evident in all permafrost regions examined, but are more muted for the Alaskan North Slope, northwestern Canada, and East Siberia (Smith et al. 2025). However, the lack of permafrost temperature data and limited ALT measurements for the Russian Arctic since 2022 have resulted in a regional gap in the assessment of the current state and recent trends of Arctic permafrost.

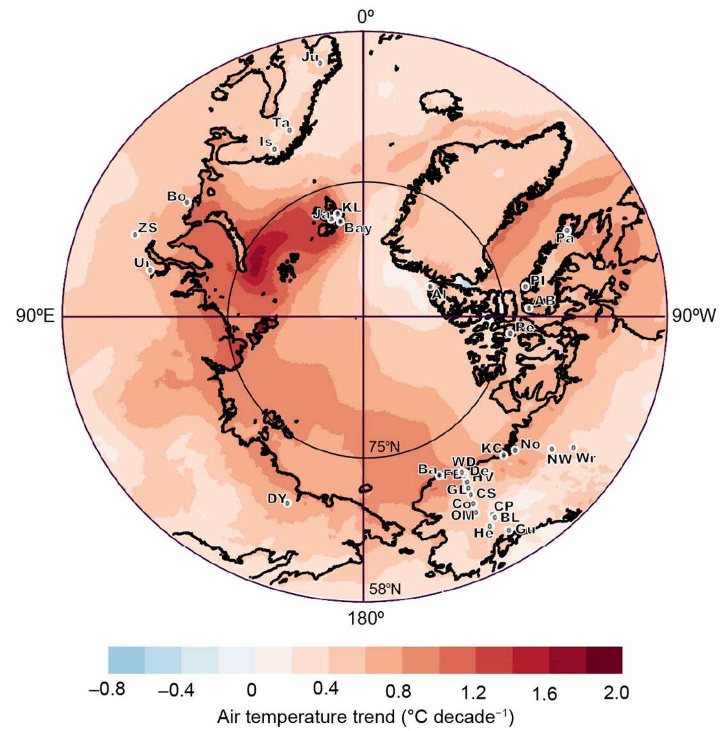

Fig. 5.29. Locations of the permafrost temperature monitoring sites (for which data are shown in Fig. 5.30) superimposed on annual average surface air temperature trends (°C decade^{-1}) for the period 1981–2025 from ERA5 (Hersbach et al. 2020; data available at https://cds.climate.copernicus.eu), which largely covers the period of record for permafrost monitoring. See Table 5.2 for site names. Information about these sites is available at http://gtnpdatabase.org/ and https://permafrost.gi.alaska.edu/sites_map.

1. PERMAFROST TEMPERATURE

Permafrost temperatures in 2025 were the highest on record at 15 of 24 sites reporting (Table 5.2). In North America, record temperatures were observed at 11 of 19 sites reporting. Seventeen of the North American sites, where there were sufficient data, had higher temperatures in 2025 compared to 2024, including all sites reporting for the Beaufort-Chukchi region, reflecting the higher air temperatures in 2023/24 following a short cooling period (Figs. 5.30a,b). For discontinuous permafrost in Alaska and northwestern Canada, permafrost in 2025 was warmer than in 2024 at all seven sites with sufficient data (Fig. 5.30b), with record temperatures at five sites. Record-high temperatures were observed at two of the four sites reporting in the eastern and high Canadian

Arctic (Fig. 5.30c). At the Nordic sites within the Barents region, permafrost temperatures in 2025 reached record highs at all reporting locations, except for one in southern Norway (Table 5.2; Fig. 5.30d).

Throughout the Arctic, warming of permafrost with temperatures near 0°C (temperatures >–2°C) is slower (generally <0.2°C decade^{-1}) than colder permafrost sites due to latent heat effects related to melting ground ice. At cold continuous permafrost sites in the Beaufort-Chukchi region, permafrost temperatures have increased by 0.4°C–0.8°C decade^{-1} with similar increases (up to 1°C decade^{-1}) for the four sites reporting in 2025 in the eastern and high Canadian Arctic (Figs. 5.30a,c; Table 5.2). In Svalbard, permafrost has warmed by up to 0.7°C decade^{-1} (Fig. 5.30d; Table 5.2) with significant warming detected down to a depth of 100 m (Isaksen et al. 2022). In Scandinavia's discontinuous permafrost regions, warming continues at rates of 0.2°C–0.5°C decade^{-1} (Fig. 5.30d; Table 5.2), with thawing observed to 22-m depth at Iskoras (Isaksen et al. 2022). Similar rates are observed in the discontinuous permafrost region of northwestern North America (Fig. 5.30b; Smith et al. 2024, 2025).

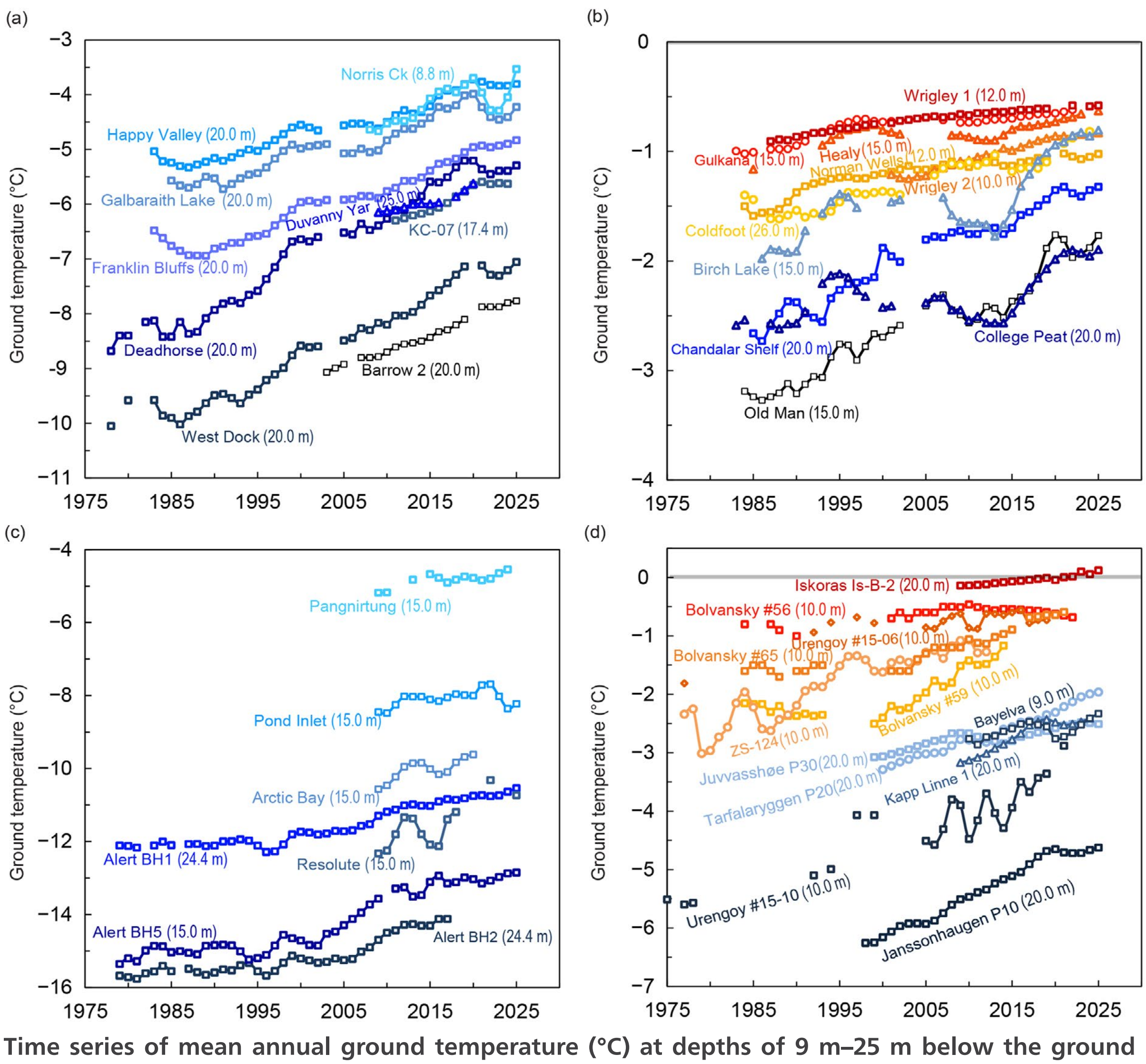

Fig. 5.30. Time series of mean annual ground temperature (°C) at depths of 9 m–25 m below the ground surface at selected measurement sites that fall roughly into the Adaptation Actions for a Changing Arctic priority regions (see Romanovsky et al. 2017): (a) cold continuous permafrost of northwestern North America and northeastern East Siberia (Beaufort–Chukchi region); (b) discontinuous permafrost in Alaska and northwestern Canada; (c) cold continuous permafrost in the eastern and high Arctic Canada (Baffin Davis Strait); and (d) continuous to discontinuous permafrost in Scandinavia, Svalbard, and Russia/Siberia (Barents regions). Temperatures are measured at or near the depth of zero annual amplitude, where the seasonal ground temperature variations are less than 0.1°C. Note differences in y-axis value ranges. Borehole locations are shown in Fig. 5.29 (data are updated from Smith et al. 2025).

Table 5.2. Rate of change in mean annual ground temperature (°C decade^{-1}) for permafrost monitoring sites shown in Fig. 5.29. The periods of record are shown in parentheses below the rates of change. For sites where measurements began prior to 2000, the rate of change for the entire available record and the period after 2000 are provided. Stations with record-high 2025 temperatures are indicated with a thermometer icon ( ) and are underlined. Asterisks denote sites not reporting in 2025. Regions correspond to those shown in Fig. 5.29.

Region	Site	Entire Record	Since 2000
Northeast Siberia *(Beaufort–Chukchi Region)*	Duvany Yar (DY)*	NA	+0.4 (2009–20)
Alaskan Arctic plain *(Beaufort–Chukchi Region)*	West Dock (WD), Deadhorse (De), Franklin Bluffs (FB), Barrow (Ba)	+0.5 to +0.8 (1978–2025)	+0.5 to +0.7 (2000–25)
Northern foothills of the Brooks Range, Alaska *(Beaufort–Chukchi Region)*	Happy Valley (HV), Galbraith Lake (GL)	+0.4 (1983–2025)	+0.4 (2000–25)
Northern Mackenzie Valley *(Beaufort–Chukchi Region)*	Norris Ck (No), KC-07 (KC)*	NA	+0.5 to +0.6 (2008–25)
Southern foothills of the Brooks Range, Alaska *(Discontinuous permafrost: Alaska and northwestern Canada)*	Coldfoot (Co)*, Chandalar Shelf (CS), Old Man (OM)	+0.2 to +0.4 (1983–2025)	+0.2 to +0.4 (2000–25)
Interior Alaska *(Discontinuous Permafrost: Alaska and northwestern Canada)*	College Peat (CP), Birch Lake (BL), Gulkana (Gu)*, Healy (He)	+0.1 to +0.2 (1983–2025)	<+0.05 to +0.4 (2000–25)
Central Mackenzie Valley *(Discontinuous Permafrost: Alaska and northwestern Canada)*	Norman Wells (NW), Wrigley (Wr1, Wr2)	+0.1 (1984–2025)	+0.1 to +0.2 (2000–25)
Baffin Island *(Baffin Davis Strait region)*	Pangnirtung (Pa)*, Pond Inlet (PI)	NA	+0.2 to +0.3 (2009–25)
High Canadian Arctic *(Baffin Davis Strait region)*	Resolute (Re)	NA	+1.0 (2009–25)
High Canadian Arctic *(Baffin Davis Strait region)*	Alert (Al) @ 15 m, Alert (Al) @ 24 m	+0.6, +0.4 (1979–2025)	+0.8, +0.5 (2000–25)
Northwest Siberia *(Barents region)*	Urengoy 15-06* and 15-08* (Ur)	+0.2 to +0.5 (1974–2021)	+0.1 to +0.8 (2005–21)
Russian European North *(Barents region)*	Bolvansky 56* and 65* (Bo)	+0.1 to +0.3 (1984–2022)	0 to +0.5 (2001–22)
Svalbard *(Barents region)*	Janssonhaugen (Ja), Bayelva (Bay), Kapp Linne 1 (KL)*	+0.7 (1998–2025)	+0.1 to +0.7 (2000–25)
Northern Scandinavia *(Barents region)*	Tarfalarggen (Ta), Iskoras Is-B-2 (Is)	NA	+0.1 to +0.5 (2000–25)
Southern Norway *(Barents region)*	Juvvasshøe (Ju)	+0.2 (1999–2025)	+0.2 (2000–25)

2. ACTIVE LAYER THICKNESS

Active layer thickness is measured directly using thaw tubes, inferred from mechanically probing at the end of the thaw season or by using interpolation of borehole temperatures to determine the maximum seasonal depth of the 0°C isotherm (Irrgang et al. 2025). Regional ALT trends presented (Fig. 5.31) are based primarily on spatially distributed mechanical probing across representative permafrost landscapes.

The highest long-term (1996–2025) rates of ALT increases are 0.19 m decade^{-1} and 0.15 m decade^{-1} observed in the Alaskan Interior and West Siberia, respectively. The 2025 data continue these trends with ALT values well above the 2009–18 mean for both regions. Record-high ALT anomalies were observed in 2025 in the Alaskan Interior and at bedrock sites in Svalbard.

ALT records from sites at the North Slope of Alaska, Greenland, northwest Canada, Russian European North, and East Siberia indicate no significant changes over the last five years. This can be partly attributed to subsidence associated with thaw propagation into ice-rich ground, therefore suggesting the underestimation of ice-rich permafrost thaw inferred from ALT records (O'Neill et al. 2023; Nyland et al. 2021; Streletskiy et al. 2025).

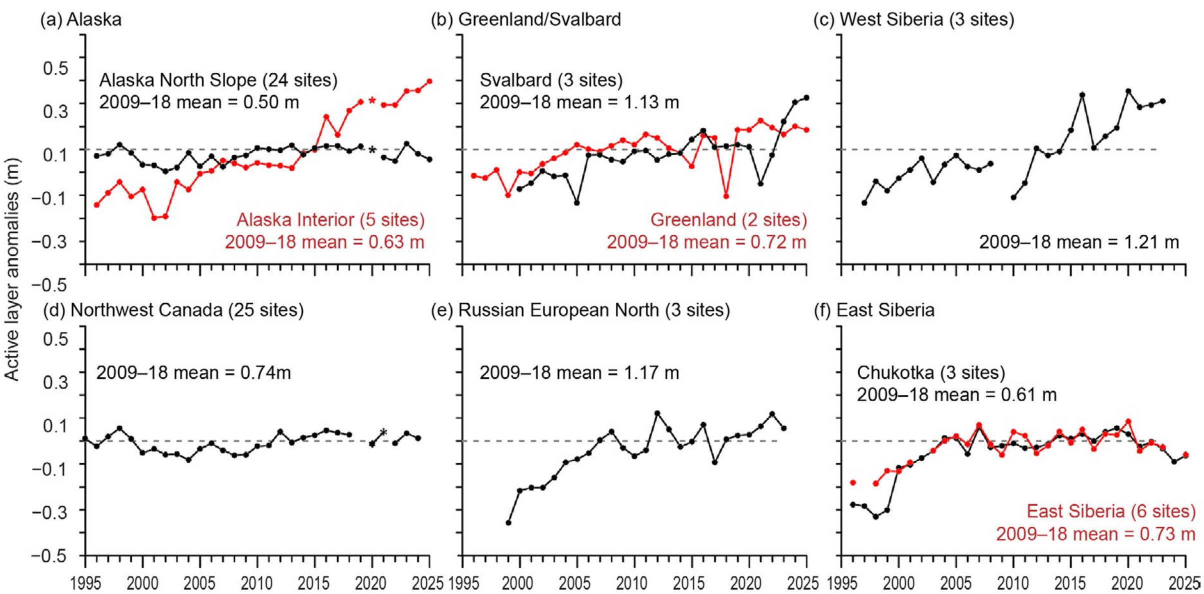

Fig. 5.31. Average annual active layer thickness (ALT) anomalies (m), relative to the 2009–18 mean, for six Arctic regions observed at the Circumpolar Active Layer Monitoring program sites with >20-years of continuous thaw depth observations from the end of the thaw season. Positive and negative anomalies indicate thicker or thinner ALT than the 10-yr reference, respectively. Asterisks represent atypical observations, for example, due to pandemic-related restrictions. Canadian ALT is derived from thaw tubes that record the maximum thaw depth over the previous year. Since Canadian sites were not visited in 2020 and 2021, the maximum thaw depth recorded during the 2022 visit could have occurred any summer from 2019 through 2021, although the data point is plotted in 2021. Only one site reported 2025 data from West and East Siberia, and none from the Russian European North. Additionally, 2023/24 measurements are based on only one Russian European North site. Site-specific data and metadata are available at www2.gwu.edu/~calm/.

Sidebar 5.2: **The Arctic carbon cycle**
—E. A. G. SCHUUR AND S. M. NATALI

The Arctic, in the broad sense of the term including the areas of northern continuous and discontinuous permafrost zones characterized by cryosphere elements (Meredith et al. 2019), has the potential to accelerate climate change by adding carbon dioxide (CO_2) and methane (CH_4) to the atmosphere in response to warming induced by human fossil fuel use and land use change (Schuur et al. 2015; Stroeve et al. 2025). A key research question is whether this climate feedback is already taking place and, if so, at what magnitude (Canadell et al. 2021). New evidence has been synthesized from networks of ground-based eddy covariance and chamber CO_2 and CH_4 exchange measurements (Vogt et al. 2025). Permafrost region soils contain organic carbon, the accumulated remains of past ecosystems that re-enters the modern carbon cycle when decomposed and emitted by microbes as CO_2 and CH_4 (Schuur et al. 2023). This can be offset, in part, by carbon uptake via increased plant growth that eventually ends up re-accumulating as surface soil organic matter (Frost et al. 2025a).

Carbon exchange measurements record the ecosystem carbon balance (net gain or loss of plant and soil carbon pools), which is the relatively small difference between large opposing fluxes: plant CO_2 uptake via plant photosynthesis and growth versus respiratory CO_2 loss via metabolism by most living organisms. In the case of net ecosystem CH_4 exchange, it is microbial CH_4 consumption in aerobic soil environments offsetting microbial CH_4 production in anaerobic environments typical of waterlogged soils, wetlands, and lake sediments (Parmentier et al. 2024; Saunois et al. 2025). Methane exchange is a much smaller amount by weight than CO_2 and consequently does not greatly alter ecosystem carbon balance at the landscape scale. But the larger warming potential of CH_4 means that changing emissions can affect climate at a similar magnitude as CO_2 (Schuur et al. 2022). While very few individual sites have monitored carbon exchange over long time periods, combining measurements across study sites has created a merged database and synthetic time series that can be analyzed for decadal-scale, site-based trends for CO_2 (See et al. 2024). Synthesized site-based carbon exchange measurements can also be scaled with environmental information to produce regional estimates for CO_2 and CH_4 (Ramage et al. 2024; Kuhn et al. 2025) and regional trends for CO_2 (Virkkala et al. 2025). When this is done, physical disturbances, such as fire and abrupt permafrost thaw that might occur away from carbon flux measurement sites, must also be considered as pathways of regional carbon exchange, as well as ecosystem types, such as inland waters that are sometimes less well represented by the ground-based measurement network.

New analyses of these merged databases suggest that tundra and boreal forest ecosystems in the northern permafrost region acted as an annual net CO_2 sink (–0.340 Pg C yr^{-1}; negative numbers indicate net ecosystem carbon accumulation), the balance of ecosystem carbon uptake and release averaged over the past several decades (2000–20) and scaled to the region (Ramage et al. 2024). When CO_2 outgassing from rivers and lakes are included into the budget along with fires, the region switches to a small net CO_2 source to the atmosphere (+0.012 Pg C yr^{-1}; positive numbers indicate net atmosphere carbon accumulation). This source strength is larger (+0.106 Pg C yr^{-1}) when lateral river carbon export is included, which is another source of carbon loss from the region. The effect of northern ecosystems on climate change is less about whether the region acts as a net carbon source/sink overall, but rather, on the change in source/sink strength over time that is induced by warming. At the same time, if this region was acting as a persistent net carbon source of CO_2 to the atmosphere over years to decades, it would be an unequivocal signal of departure from long-term patterns as a regional sink that served to accumulate and store permafrost carbon in the Arctic over the recent centuries to millennia (Lindgren et al. 2018).

A related analysis of the merged dataset supported the conclusion that tundra and boreal ecosystems scaled to the permafrost region acted as an annual net CO_2 sink (–0.249 Pg C yr^{-1}), and that this sink was almost entirely reversed when only fire emissions were added (–0.02 Pg C yr^{-1}), bringing these two components essentially to carbon neutral with respect to the atmosphere (Virkkala et al. 2025; Fig. SB5.3). Furthermore, the carbon sink trend over time of tundra and boreal forest that was shown to be increasing from 2000 to 2021 by an additional –0.009 Pg C yr^{-1} was erased when emissions by fires were included. This analysis also demonstrated a clear spatial pattern where the strongest net carbon sink ecosystems were farther south in the boreal biome whereas more than 30% of the tundra ecosystems to the north were acting as carbon sources, averaged over the 2001–20 period. The spatial covariance with fluxes means that the larger the northern land region considered, the larger the carbon sink strength as forests in the southern margin of the boreal biome responding to warming and CO_2 fertilization were masking carbon losses from tundra farther to the north. Indeed, the pattern of increasing growth and carbon sink strength in the summer growing season were found to be completely offset by increasing winter carbon emissions in ecosystems directly underlain by permafrost (See et al. 2024). This contrasted with non-permafrost ecosystems where trends of increasing annual net carbon sink over time matched summer patterns.

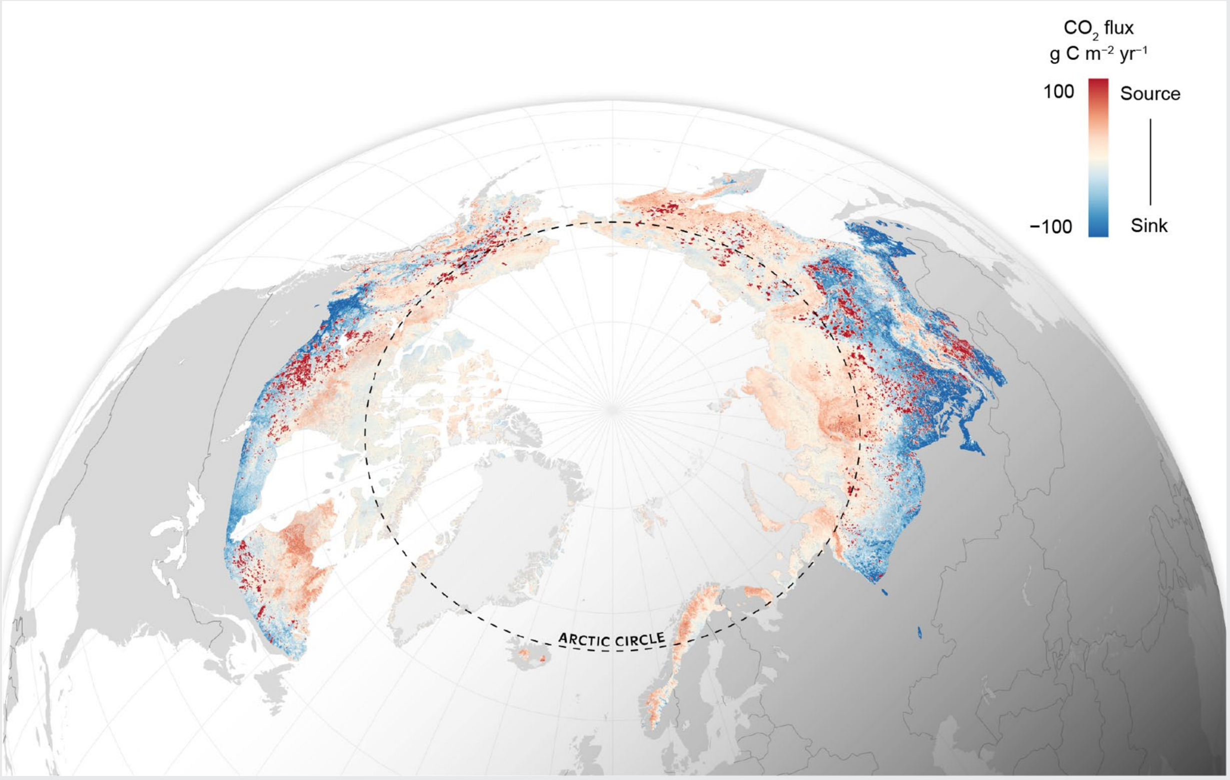

Fig. SB5.3. Terrestrial ecosystem carbon dioxide (CO_2) fluxes with direct fire emissions (red shading) for the northern permafrost region (2002–20 average). Areas that are CO_2 sources are shown in pink and red and CO_2 sinks are shown in blue (Natali et al. 2024).

These analyses have looked backwards at tundra and boreal ecosystem carbon fluxes over the past two decades. One of the grand challenges for Arctic carbon research has been to provide near real-time snapshots of carbon fluxes to understand how unprecedented environmental conditions observed right now in the region influence the carbon feedback to climate. Recent work has produced annual Arctic carbon updates for 2024 and 2025 by analyzing monthly carbon exchange across a snapshot of U.S. and European-based observatories that were able to provide near real-time carbon flux information in the year that it was collected (Falvo et al. 2025, 2026). Both 2024 and 2025 had record-warm winter conditions across the Arctic region, and dynamic patterns of precipitation. In 2024, a record number of monthly emission values were observed for CO_2 in the winter for both tundra and boreal sites, beyond the number expected by chance (Fig. SB5.4). CO_2 uptake was observed in the growing season for both tundra and boreal sites compensating for winter emissions, but uptake did not set more records than expected in 2024. The pattern of carbon cycle amplification, increased uptake and increased loss, has been observed in decadal-scale patterns from the merged dataset across the region (See et al. 2024). Methane observations from the near real-time analysis were from a more limited subset of sites as compared to CO_2 and there were more monthly emissions records than expected during winter in the 2024 analysis. Near real-time CO_2 and CH_4 measurements provide society immediate knowledge about the speed and strength of the Arctic carbon feedback to climate (Natali et al. 2021). Near real-time CO_2 and CH_4 measurements provide information about the speed and strength of Arctic carbon-cycle feedbacks to climate (Natali et al. 2021). These observations contribute to our understanding of how Arctic emissions affect the global carbon budget and influence projections associated with future temperature targets.

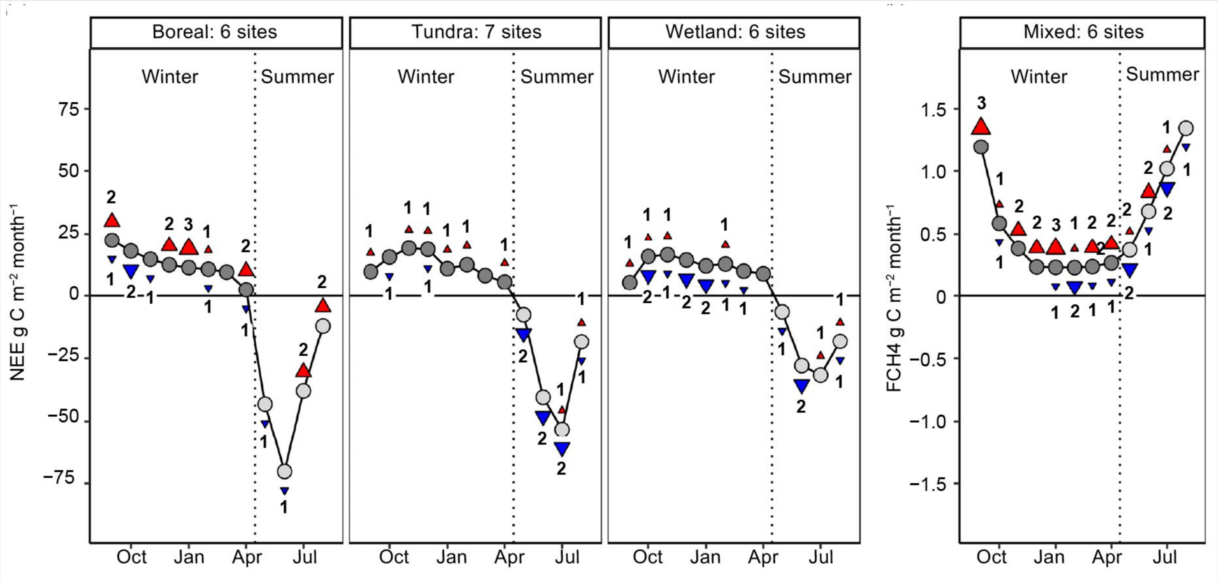

Fig. SB5.4. (a) Net carbon dioxide (NEE g C m^{-2} $month^{-1}$) and (b) methane fluxes (FCH_4 g C m^{-2} $month^{-1}$) and their records for Sep 2023–Aug 2024. Points denote the monthly mean flux grouped by ecosystem type (for carbon dioxide) or grouped across sites (for methane). Record-high and record-low observations of each month are highlighted with upward facing red triangles and downward facing blue triangles, respectively. The size of the triangles and the numbers denote the number of sites with a record flux observed in that month. Positive values indicate net release from the ecosystem to the atmosphere, and negative values indicate a net uptake from the atmosphere to the ecosystem (Falvo et al. 2026).

k. Tundra greenness

—G. V. Frost, M. J. Macander, U. S. Bhatt, L. T. Berner, J. W. Bjerke, H. E. Epstein, B. C. Forbes, G. Jia, M. J. Lara, E. López-Blanco, P. M. Montesano, R. Í. Magnússon, C. S. R. Neigh, K. M. Orndahl, G. K. Phoenix, H. Tømmervik, C. Waigl, D. A. Walker, and D. Yang

The Arctic tundra biome occupies Earth's northernmost lands, collectively encompassing a 5.1 million km^2 region bound by the Arctic Ocean to the north and the boreal forest biome to the south (Raynolds et al. 2019). While Arctic tundra ecosystems are treeless and lack the vertical structure of forests, they are very heterogeneous across multiple spatial scales, ranging from large-scale latitudinal climate gradients to local-scale gradients of soil, hydrological, and permafrost conditions (Fig. 5.32). In recent decades, the Arctic has warmed dramatically,

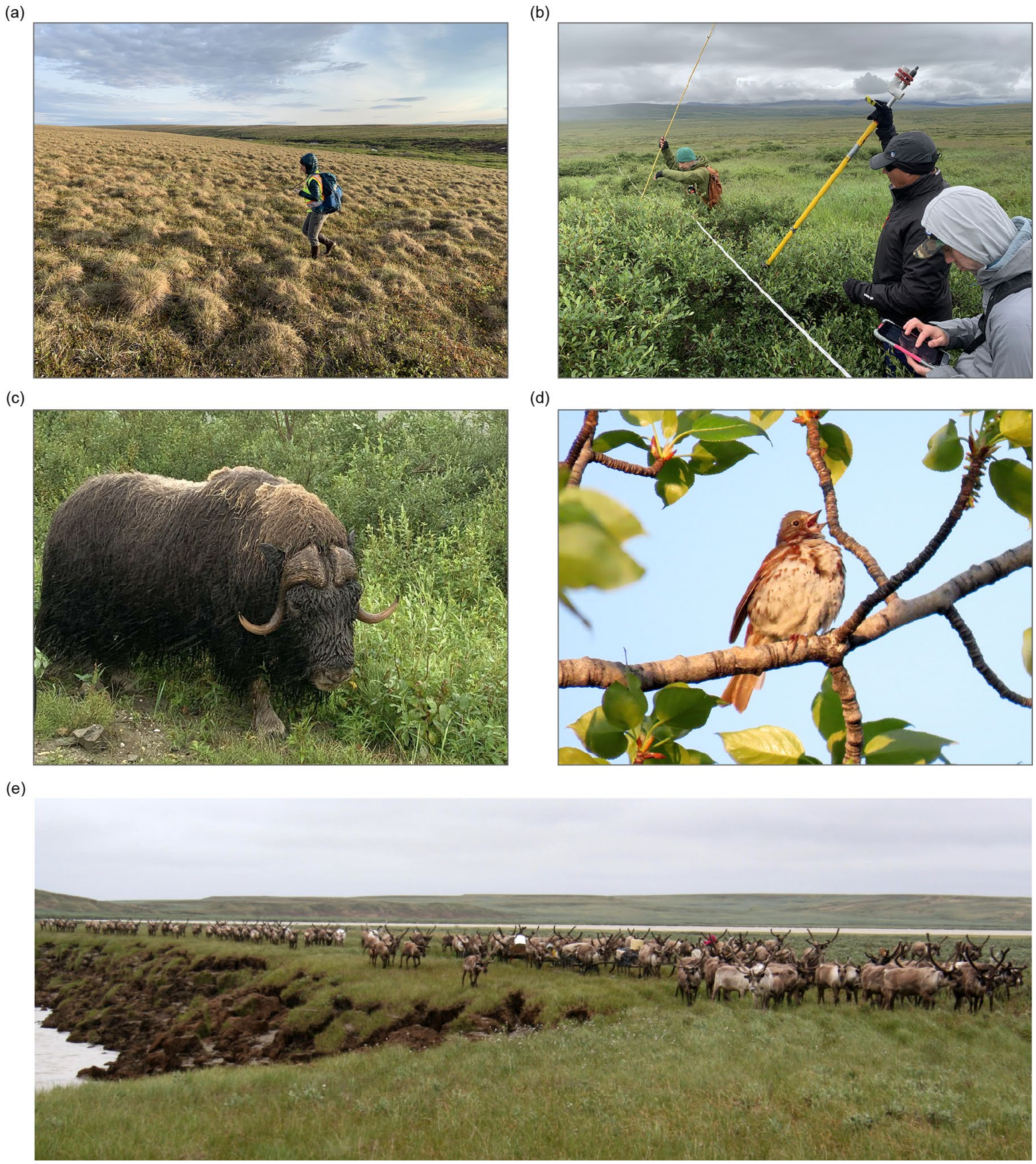

Fig. 5.32. Arctic tundra ecosystems are generally dominated by low-growing shrubs, herbs, and nonvascular plants, as seen in a tussock tundra community in northwestern Alaska (upper left). However, canopy-forming shrubs have been expanding in many Arctic regions and have become a focus of Arctic ecological research (upper right). Shrub increase has large implications for Arctic landscape processes, land–atmosphere interactions, permafrost dynamics, and wildlife including iconic Arctic mammals such as muskox (middle left). The increased vertical structure provided by shrubs has been a primary mechanism for "borealization," the northward expansion of boreal forest species such as Fox Sparrow (middle right). Interactions between changing Arctic ecosystems, traditional reindeer herding, and industrial development have led to complex changes in northwest Siberian tundra ecosystems (bottom).

far exceeding the global rate of warming (section 5c) and placing the circumpolar region at the forefront of global climate and environmental change (Rantanen et al. 2022). Today, the circumpolar region lies at the crossroads of multiple feedback mechanisms that connect the living Arctic with a warming climate, declining sea ice extent, changes in seasonal snow cover, permafrost thaw, and the global carbon cycle (Bartsch et al. 2025; Aalto et al. 2026; sections 5d,f,i,j; SB5.2). Some of the most compelling evidence of broad-scale changes in this expansive region comes from long-term satellite observations beginning in the early 1980s. By the late 1990s, Earth-observing satellites began to detect a sharp increase in the productivity of tundra vegetation, a phenomenon known today as “the greening of the Arctic.”

The era of global spaceborne monitoring of vegetation began in late 1981 with a series of satellites equipped with the Advanced Very High Resolution Radiometer (AVHRR). Beginning in 2000, the circumpolar AVHRR record has been complemented by more modern sensors with improved calibration and spatial resolution, including the Moderate Resolution Imaging Spectroradiometer (MODIS) and the long-running series of Landsat satellites. Although AVHRR remains operational, the raw data require extensive processing, and the AVHRR-derived Global Inventory Modeling and Mapping Studies 3g V1.2 dataset (GIMMS-3g+) that long underpinned Arctic vegetation monitoring is no longer funded. MODIS is nearing the end of service, but continuity of this important record will be maintained by the Visible Infrared Imaging Radiometer Suite (VIIRS) sensor, first launched in 2011. Data from all of these sensors support monitoring of global vegetation greenness using the Normalized Difference Vegetation Index (NDVI), a spectral metric that exploits the unique way in which green vegetation absorbs and reflects visible and infrared light. Here, the ongoing phenomenon of Arctic greening and its pan-Arctic spatial variability are reported based on all four satellite records, with emphasis on the MODIS dataset.

Although the legacy GIMMS-3g+ dataset is no longer maintained, we include it here because of its longevity (1982–2024) with a spatial resolution of approximately 8 km (Pinzon et al. 2023). For MODIS, trends were computed by combining 16-day NDVI products from the *Terra* (MOD13A1, version 6.1) and *Aqua* (MYD13A1, version 6.1) satellites (Didan 2021a,b), referred to as MODIS MCD13A1, at a spatial resolution of 500 m. For VIIRS, the recently reprocessed VNP13A1 dataset (version 2; Román et al. 2024) was used. Landsat provides observations at a much higher spatial resolution (30 m); greenness time series from Landsat Collection 2 (Crawford et al. 2023) were calculated following the methods of Berner and Goetz (2022). All data were masked to the extent of the Circumpolar Arctic Vegetation Map (Raynolds et al. 2019), excluding permanent ice and water. For all records, the trends of annual Maximum NDVI (MaxNDVI), the peak greenness value observed in midsummer, are summarized. MaxNDVI is a strong indicator of aboveground biomass and is sensitive to disturbance, successional processes, and long-term shifts in vegetation structure.

In 2025, the MODIS-observed circumpolar mean MaxNDVI was nearly identical to that in 2024 (−0.2%) and ranked as the third highest in the sensor’s 26-year record. This continued a sequence of record- or near-record-high values that began in 2020, with the five highest MaxNDVI values occurring since that year (Fig. 5.33). Tundra greenness was much higher

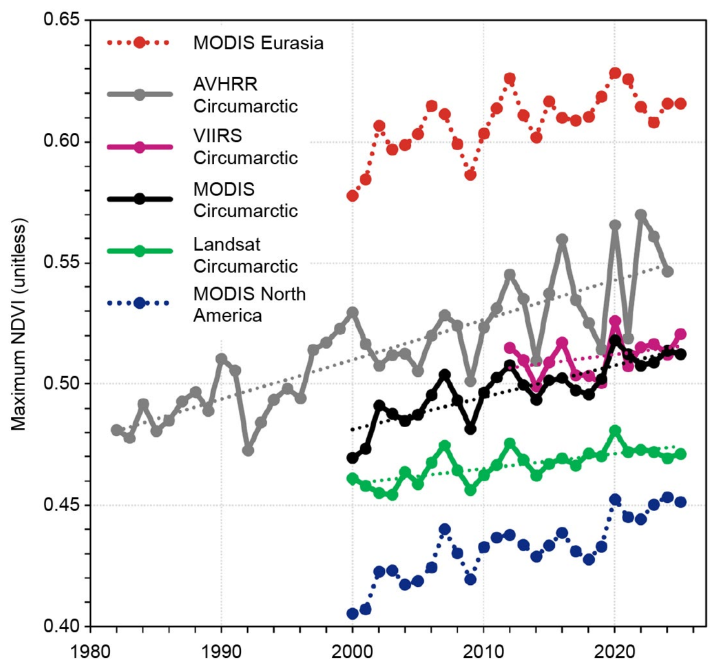

Fig. 5.33. Time series of circumpolar mean Maximum Normalized Difference Vegetation Index (MaxNDVI) from (now terminated) Advanced Very High-Resolution Radiometer (AVHRR) Global Inventory Modeling and Mapping Studies third generation (GIMMS-3g+; 1982–2024; gray), Moderate Resolution Imaging Spectroradiometer (MODIS) MCD13A1 (2000–25; black) Landsat Collection 2 (2000–25; green), and the Visible Infrared Imaging Radiometer Suite (VIIRS) VNP13A1 (2011–25; pink), with trendlines fitted using ordinary least squares linear regression. The MODIS record is further divided by continent for Arctic Eurasia (dotted red) and North America (dotted blue).

than the 2000–25 mean value across most of the North American Arctic, particularly in northern Alaska, Quebec, and Labrador (Fig. 5.34). The Eurasian Arctic, however, featured a much greater mixture of positive and negative anomalies, a pattern that has recurred for the last several years. Nonetheless, the long-term trend in MODIS-observed tundra greenness is strongly positive (greening) for most of the circumpolar region (Fig. 5.35). Although no longer maintained, the GIMMS-3g+ dataset provides one of the clearest signals of long-term Arctic greening, with four of the five highest MaxNDVI values in the 43-year record occurring since 2020. The much shorter VIIRS record is generally consistent with the other records, especially MODIS; the circumpolar mean greenness in 2025 was the second highest in the 14-year record. Greening is least pronounced in the Landsat record, with very little variation in greenness following the record high value in 2020. Variations among the satellite records likely reflect differences in sensor bandpasses, radiometric spatial resolution, calibration, and frequency of observation (Frost et al. 2025b). Going forward, spaceborne monitoring of tundra greenness will rely solely on the VIIRS and Landsat records; continuity of these records is therefore essential to sustain current

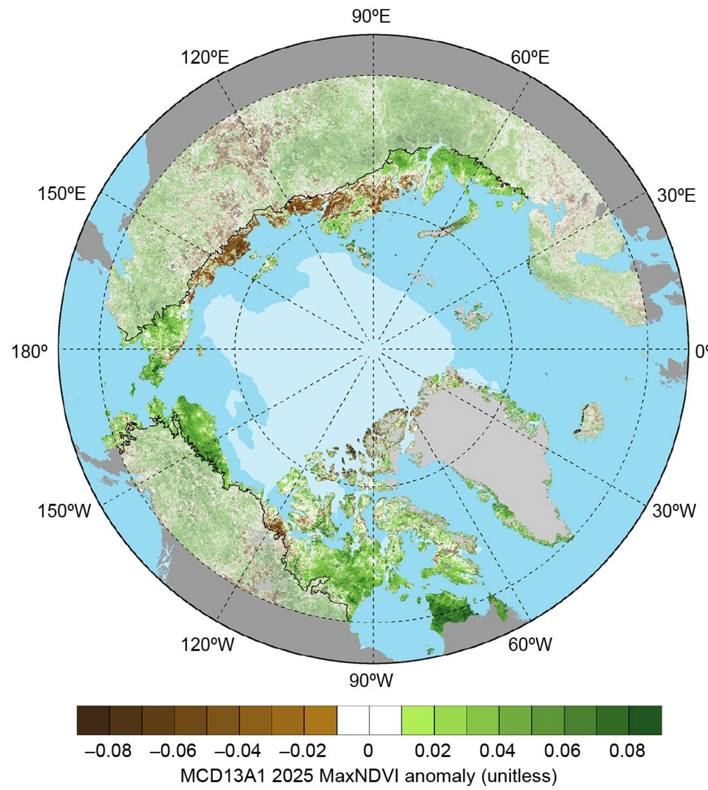

Fig. 5.34. Circumpolar Maximum Normalized Difference Vegetation Index (MaxNDVI) anomalies for the 2025 growing season relative to mean values (2000–25) for Arctic tundra (bold colors), and boreal forest (muted colors) north of 60° latitude from the Moderate Resolution Imaging Spectroradiometer (MODIS) MCD13A1 dataset. The circumpolar tree line is indicated by a black line, and the 2025 minimum sea ice extent is indicated by light shading.

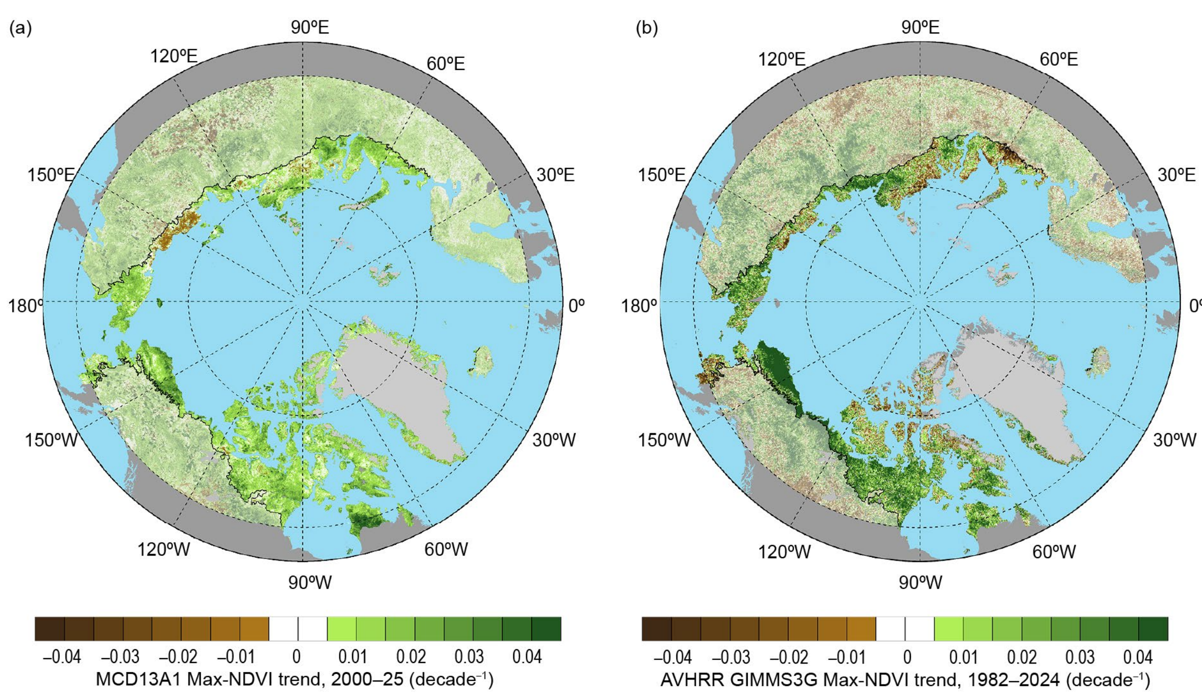

Fig. 5.35. Magnitude of the Maximum Normalized Difference Vegetation Index (MaxNDVI) trend calculated as the change decade^{-1} via ordinary least squares regression for Arctic tundra (bold colors), and boreal forest (muted colors) north of 60° latitude during (a) 2000–25 based on the Moderate Resolution Imaging Spectroradiometer (MODIS) MCD13A1 dataset, and (b) 1982–2024 based on the (now terminated) legacy Advanced Very High-Resolution Radiometer GIMMS 3-g+ dataset. The circumpolar tree line is indicated by a black line.

standards in monitoring Arctic vegetation dynamics and modeling their influence on the global carbon cycle.

Earth-observing satellites provide foundational datasets for monitoring Arctic changes and help overcome long-standing barriers to access posed by the remoteness of this region, and new ones arising from the cessation of international cooperation in the Russian Arctic and uncertainties in long-standing funding and logistical support for Arctic research in the United States and the European Union. Nonetheless, field studies provide crucial information needed to connect spaceborne observations with patterns of change (or stability) on the ground. Observed increases in the abundance, distribution, and height of Arctic shrubs are a major driver of Arctic greening, and have important impacts on biodiversity, wildlife habitat, surface energy balance, permafrost dynamics, and biogeochemical cycling, particularly in warmer, more southerly portions of the biome near the forest–tundra ecotone (Mekonnen et al. 2021; Fig. 5.32). However, trend attribution remains difficult in understudied regions, such as the Canadian Arctic Archipelago and much of the Russian Arctic. Furthermore, while changes to the Arctic climate have generally favored tundra greening, ecological disturbances, extreme events, and other causes of local declines in greenness ("browning") are increasing in frequency (Lechler et al. 2025; Phoenix et al. 2025), and major knowledge gaps remain concerning climate–carbon feedbacks in Arctic permafrost (Bao et al. 2025). Changes to Arctic land-use also contribute to the complexity in greening and browning trends. For example, the transition of nomadic reindeer herding from a non-monetary livelihood to a market economy has led to regional ecological changes in Eurasian tundra (Bjerke et al. 2024; Wallenius et al. 2025; Fig. 5.32). Understanding the regional variability of complex Arctic vegetation trends and determining their drivers continues to be an important focus of multi-disciplinary scientific research.

Acknowledgments

a. Overview

Authors/chapter editors appreciate support provided by NOAA's Global Ocean Monitoring & Observing Arctic Research Program, including content editing funded through the Cooperative Institute for Earth System Research and Data Science (CIESRDS) via NOAA Cooperative Agreement NA22OAR4320151 (M. Druckenmiller and T. Moon) and by the Cooperative Institute for Climate, Ocean, and Ecosystem Studies (CICOES) under NOAA Cooperative Agreement NA20OAR4320271 (R. Thoman).

e. Sea Surface Temperature

M.-L. Timmermans acknowledges support from the National Science Foundation Office of Polar Programs and the Office of Naval Research. We thank Dr. Kristina Dahl (Climate Central) for reviewing the section. NOAA OI SST V2 High Resolution Dataset data provided by the NOAA PSL, Boulder, Colorado, from their website at https://psl.noaa.gov.

Sidebar 5.2: The Arctic carbon cycle

This work was based on support provided by the following programs: The Arctic Carbon Warning Network (AWARE) funded by the Minderoo Foundation (EAGS, GF); Permafrost Pathways through TED Audacious (SMN).

Appendix 1: Acronyms

ALT	active layer thickness
AMAP	Arctic Monitoring and Assessment Programme
ATBD	Algorithm Theoretical Basis Document
AVHRR	Advanced Very High-Resolution Radiometer
CALM	Circumpolar Active Layer Monitoring
CAVM	Circumpolar Arctic Vegetation Map
CCI	Climate Change Initiative
CDR	Climate Data Record
CDS	Climate Data Store
CNECT	CEOS/NSIDC Extratropical Cyclone Tracking
CRDP	climate research data package
DMI	Danish Meteorological Institute
DOISST	Daily Optimum Interpolation Sea Surface Temperature
DU	Dobson units
ESA	European Space Administration
ET	extratropical transition
GIMMS-3g+	Global Inventory Modeling and Mapping Studies third generation
GPCC	Global Precipitation Climatology Centre
GRACE	Gravity Recovery and Climate Experiment
GRACE-FO	Gravity Recovery and Climate Experiment Follow-On
IMS	Interactive Multisensor Snow and Ice Mapping System
JTWC	Joint Typhoon Warning Center
MaxNDVI	Maximum Normalized Difference Vegetation Index
MODIS	Moderate Resolution Imaging Spectroradiometer
NAM	Northern Annular Mode
NAO	North Atlantic Oscillation
NDVI	Normalized Difference Vegetation Index
ODS	Ozone-Depleting Substance
OISST	Optimum Interpolation Sea Surface Temperature
OMI	Ozone Monitoring Instrument
OMTO3	Ozone Monitoring Instrument Level-2 Total Column Ozone version 3
PROMICE	Programme for Monitoring of the Greenland Ice Sheet
SAT	surface air temperature
SCD	snow cover duration
SCE	snow cover extent
SLP	sea level pressure
SMB	surface mass balance
SMOS	Soil Moisture Ocean Salinity
SSMIS	Special Sensor Microwave Imager/Sounder
SST	sea surface temperature
SWE	snow water equivalent
SWIPA	Snow Water Ice and Permafrost in the Arctic
UV	ultraviolet
VIIRS	Visible Infrared Imaging Radiometer Suite
WGMS	World Glacier Monitoring Service

Appendix 2: Datasets and sources

Section 5b Atmosphere

Sub-section	General Variable or Phenomenon	Specific Dataset or Variable	Source
5b	Geopotential Height	ERA5	https://www.ecmwf.int/en/forecasts/dataset/ecmwf-reanalysis-v5
5b	Temperature, Upper Atmosphere	ERA5	https://www.ecmwf.int/en/forecasts/dataset/ecmwf-reanalysis-v5
5b	Wind, Upper Atmosphere	ERA5	https://www.ecmwf.int/en/forecasts/dataset/ecmwf-reanalysis-v5
5b1	Ozone, Total Column and Stratospheric	Aura Ozone Monitoring Instrument (OMI)/Microwave Limb Sounder (MLS)	https://mls.jpl.nasa.gov/eos-aura-mls/data.php
5b1	Ozone, Total Column and Stratospheric	OMI/Aura Level-2 Total Column Ozone (OMTO3) Version 3	https://disc.gsfc.nasa.gov/datasets/OMTO3_003/summary

Section 5c Surface air temperature

Sub-section	General Variable or Phenomenon	Specific Dataset or Variable	Source
5c3	Pressure, Sea Level or Near-Surface	ERA5	https://www.ecmwf.int/en/forecasts/dataset/ecmwf-reanalysis-v5
5c2	Temperature, [Near] Surface	NASA GISTEMPv4	https://data.giss.nasa.gov/gistemp/
5c3	Temperature, [Near] Surface	ERA5	https://www.ecmwf.int/en/forecasts/dataset/ecmwf-reanalysis-v5

Section 5d Precipitation

Sub-section	General Variable or Phenomenon	Specific Dataset or Variable	Source
5d	Precipitation	ERA5	https://www.ecmwf.int/en/forecasts/dataset/ecmwf-reanalysis-v5
5d4	Precipitation	GPCC	https://opendata.dwd.de/climate_environment/GPCC/html/download_gate.html

Section 5e Sea surface temperature

Sub-section	General Variable or Phenomenon	Specific Dataset or Variable	Source
5e	Sea Ice Extent	National Snow and Ice Data Center (NSIDC) Sea Ice Extent	https://nsidc.org/data/g02135
5e	Sea Surface Temperature	OISSTv2.1	https://www.ncei.noaa.gov/products/optimum-interpolation-sst

Section 5f Sea ice

Sub-section	General Variable or Phenomenon	Specific Dataset or Variable	Source
5f1	Sea Ice Extent	National Snow and Ice Data Center (NSIDC) Sea Ice Extent	https://nsidc.org/data/g02135
5f2	Sea Ice Thickness	European Space Agency (ESA) Cryosat-2/ Soil Moisture and Ocean Salinity (SMOS)	https://earth.esa.int/eogateway/catalog/smos-cryosat-l4-sea-ice-thickness

Section 5g Greenland Ice Sheet

Sub-section	General Variable or Phenomenon	Specific Dataset or Variable	Source
5g	Air Temperature	Danish Meteorological Institute (DMI)/ Programme for Monitoring the Greenland Ice Sheet (PROMICE) Weather	https://eng.geus.dk/products-services-facilities/data-and-maps/glaciological-data-from-greenland-promice
5g	Glacier Ablation	PROMICE Glacier Front Line (Greenland)	https://doi.org/10.22008/promice/data/calving_front_lines
5g	Glacier Mass, Area or Volume	Gravity Recovery and Climate Experiment (GRACE) /GRACE Follow-On (GRACE-FO)	https://grace.jpl.nasa.gov/data/get-data/
5g	Ice Sheet Albedo	Sentinel-3 Snow and Ice Products (SICE)	https://eo4society.esa.int/projects/pre-operational-sentinel-3-snow-and-ice-products-sice/
5g	Ice Sheet Discharge	Ice Discharge (Greenland)	https://doi.org/10.22008/promice/data/ice_discharge/d/v02
5g	Ice Sheet Melt	Special Sensor Microwave Imager/ Sounder (SSMIS)	https://nsidc.org/data/nsidc-0001
5g	Ice Sheet Surface Height	Ice, Cloud, and land Elevation Satellite 2 (ICESat-2)	https://icesat-2.gsfc.nasa.gov/icesat-2-data

Sub-section	General Variable or Phenomenon	Specific Dataset or Variable	Source
5g	Surface Mass Balance	Modèle Atmosphérique Régionale version 3.14.1 regional climate model (MAR)	https://zenodo.org/records/13151275
5g	Surface Mass Balance	ERA5	https://www.ecmwf.int/en/forecasts/dataset/ecmwf-reanalysis-v5

Section 5h Glaciers and ice caps outside Greenland

Sub-section	General Variable or Phenomenon	Specific Dataset or Variable	Source
5h	Glacier Mass, Area or Volume	World Glacier Monitoring Service	http://dx.doi.org/10.5904/wgms-fog-2022-09
5h	Glacier Mass, Area or Volume	Gravity Recovery and Climate Experiment Follow-on (GRACE/GRACE-FO)	https://grace.jpl.nasa.gov/data/get-data/

Section 5i Terrestrial snow cover

Sub-section	General Variable or Phenomenon	Specific Dataset or Variable	Source
5i	Snow Properties	Crocus Snowpack Model	https://egusphere.copernicus.org/preprints/2025/egusphere-2025-4540/
5i	Snow Properties	ERA5	https://www.ecmwf.int/en/forecasts/dataset/ecmwf-reanalysis-v5
5i	Snow Properties	MERRA-2	http://gmao.gsfc.nasa.gov/reanalysis/MERRA-2/
5i	Snow Properties	European Space Agency Snow Climate Change Initiative Snow Water Equivalent	https://snow-cci.enveo.at/
5i	Snow Properties	NOAA Interactive Multi-sensor Snow and Ice Mapping System (Snow Cover Duration)	https://usicecenter.gov/Products/ImsHome
5i	Snow Properties	NOAA Snow Chart Climate Data Record	https://www.ncei.noaa.gov/products/climate-data-records/snow-cover-extent

Section 5j Permafrost

Sub-section	General Variable or Phenomenon	Specific Dataset or Variable	Source
5j1	Permafrost	Global Terrestrial Network for Permafrost (GTN-P)	http://gtnpdatabase.org/
5j1	Permafrost	Permafrost Site Map	http://permafrost.gi.alaska.edu/sites_map
5j1	Temperature, [Near] Surface	ERA5	https://www.ecmwf.int/en/forecasts/dataset/ecmwf-reanalysis-v5
5j2	Permafrost	Circumpolar Active Layer Monitoring Program (CALM) Active-Layer Thickness	www2.gwu.edu/~calm/

Section 5k Tundra greenness

Sub-section	General Variable or Phenomenon	Specific Dataset or Variable	Source
5k	Vegetative Index	Global Inventory Modeling and Mapping Studies third generation (GIMMS-3g+) Version 1	https://daac.ornl.gov/VEGETATION/guides/Global_Veg_Greenness_GIMMS_3G.html
5k	Vegetative Index	MODIS MCD13A1 and MYD13A1 Normalized Difference Vegetative Index (NDVI)	https://lpdaac.usgs.gov/products/mod13a1v006/
5k	Vegetative Index	Landsat Collection 2 Normalized Difference Vegetative Index (NDVI)	https://www.usgs.gov/landsat-missions/landsat-collection-2
5k	Vegetative Index	Visible Infrared Imaging Radiometer Suite (VIIRS) VNP13A1	https://www.earthdata.nasa.gov/topics/biosphere/vegetation-index

Sidebar 5.1: Ex-typhoon Halong

Sub-section	General Variable or Phenomenon	Specific Dataset or Variable	Source
SB5.1	Sea Surface Temperature	OISSTv2.1	https://www.ncei.noaa.gov/products/optimum-interpolation-sst

Sidebar 5.2: The Arctic carbon cycle

Sub-section	General Variable or Phenomenon	Specific Dataset or Variable	Source
SB5.2	Carbon	Carbon emissions	https://iopscience.iop.org/article/10.1088/1748-9326/ae09bb#erlae09bbs5
SB5.2	Carbon dioxide (CO2)	Arctic-Boreal Vulnerability Experiment CO_2 fluxes	https://www.earthdata.nasa.gov/data/catalog/ornl-cloud-co2fluxes-arctic-boreal-domain-2377-1

References

Aalto, J., M. Kämäräinen, M. Rantanen, P. Niittynen, G. K. Phoenix, J. Lenoir, I. Maclean, and M. Luoto, 2026: A new era of bioclimatic extremes in the terrestrial Arctic. *Sci. Adv.*, **12**, eadw5698, https://doi.org/10.1126/sciadv.adw5698.

Ballinger, T. J., and Coauthors, 2024: Surface air temperature. NOAA Tech. Rep. OAR ARC 24-0, 8 pp., https://doi.org/10.25923/4bb3-3f87.

Bao, T., X. Xu, G. Jia, X. Zhu, W. J. Riley, and Y. Yang, 2025: Climate-carbon feedback tradeoff between Arctic and alpine permafrost under warming. *Sci. Adv.*, **11**, eadt8366, https://doi.org/10.1126/sciadv.adt8366.

Barrett, A. P., J. C. Stroeve, and M. C. Serreze, 2020: Arctic Ocean precipitation from atmospheric reanalyses and comparisons with North Pole drifting station records. *J. Geophys. Res. Oceans*, **125**, 1, https://doi.org/10.1029/2019JC015415.

Bartsch, A., and Coauthors, 2025: Similarities between sea ice area variations and satellite-derived terrestrial biosphere and cryosphere parameters across the Arctic. *Cryosphere*, **19**, 4929–4967, https://doi.org/10.5194/tc-19-4929-2025.

Becker, A., P. Finger, A. Meyer-Christoffer, B. Rudolf, K. Schamm, U. Schneider, and M. Ziese, 2013: A description of the global land-surface precipitation data products of the Global Precipitation Climatology Centre with sample applications including centennial (trend) analysis from 1901–present. *Earth Syst. Sci. Data*, **5**, 71–99, https://doi.org/10.5194/essd-5-71-2013.

Berner, L. T., and S. J. Goetz, 2022: Satellite observations document trends consistent with a boreal forest biome shift. *Global Change Biol.*, **28**, 3275–3292, https://doi.org/10.1111/gcb.16121.

Bernhard, G., and Coauthors, 2015: Comparison of OMI UV observations with ground-based measurements at high northern latitudes. *Atmos. Chem. Phys.*, **15**, 7391–7412, https://doi.org/10.5194/acp-15-7391-2015.

Bhartia, P. K., and C. W. Wellemeyer, 2002: TOMS-V8 total O3 algorithm. OMI Algorithm Theoretical Basis Doc. Volume II. NASA Goddard Space Flight Center Tech. Doc. ATBD-OMI-02, 91 pp., https://ozoneaq.gsfc.nasa.gov/content/public/OMI/ATBDs/ATBD-OMI-02.pdf.

Bjerke, J. W., K. Magnussen, R. M. Bright, S. Navrud, R. Erlandsson, E. A. Finne, and H. Tømmervik, 2024: Synergies and trade-offs between provisioning and climate-regulating ecosystem services in reindeer herding ecosystems. *Sci. Total Environ.*, **927**, 171914, https://doi.org/10.1016/j.scitotenv.2024.171914.

Box, J. E., W. Colgan, B. Wouters, D. Burgess, S. O'Neel, L. Thomson, and S. Mernild, 2018: Global sea-level contribution from Arctic land ice: 1971–2017. *Environ. Res. Lett.*, **13**, 125012, https://doi.org/10.1088/1748-9326/aaf2ed.

——, and Coauthors, 2021: Recent developments in Arctic climate observation indicators. AMAP Arctic Climate Change Update 2021: Key Trends and Impacts, Arctic Monitoring and Assessment Programme, 148 pp., https://www.amap.no/documents/doc/amap-arctic-climate-change-update-2021-key-trends-and-impacts/3594.

Brown, R., and Coauthors, 2017: Arctic terrestrial snow cover. *Snow, Water, Ice and Permafrost in the Arctic (SWIPA) 2017,* Arctic Monitoring and Assessment Programme, 25–64.

Burn, C. R., and Coauthors, 2025: Developments in permafrost science and engineering in response to climate warming in circumpolar and high mountain regions, 2019–2024. *Permafrost & Periglacial*, **36**, 167–188, https://doi.org/10.1002/ppp.2261.

Canadell, J. G., and Coauthors, 2021: Global carbon and other biogeochemical cycles and feedbacks. *Climate Change 2021: The Physical Science Basis*, V. Masson-Delmotte et al., Eds., Cambridge University Press, 673–816, https://doi.org/10.1017/9781009157896.007.

Christensen, T. R., and Coauthors, 2020: Multiple ecosystem effects of extreme weather events in the Arctic. *Ecosystems*, **24**, 122–136, https://doi.org/10.1007/s10021-020-00507-6.

Colgan, W., and Coauthors, 2015: Hybrid glacier Inventory, Gravimetry and Altimetry (HIGA) mass balance product for Greenland and the Canadian Arctic. *Remote Sens. Environ.*, **168**, 24–39, https://doi.org/10.1016/j.rse.2015.06.016.

Crawford, C. J., and Coauthors, 2023: The 50-year Landsat collection 2 archive. *Sci. Remote Sens.*, **8**, 100103, https://doi.org/10.1016/j.srs.2023.100103.

Crawford, A. D, M. C. Serreze, D. Barber, D. Dahl-Jensen, and J. Stroeve, 2021: "CEOS/NSIDC Extratropical Cyclone Tracking (CNECT)", 10.34992/ebnw-s681, CanWIN, Version 13.2, accessed 17 January 2026. https://doi.org/10.34992/ebnw-s681.

Decharme, B., A. Barbu, and S. Ramos Buarque, 2024: Crocus-ERA5 daily snow product over the Northern Hemisphere at 0.25° resolution, 2023v2. Zenodo, accessed 29 September 2025, https://doi.org/10.5281/zenodo.14513248.

Didan, K., 2021a: MODIS/Terra vegetation indices 16-day L3 global 500m SIN grid V061. NASA EOSDIS Land Processes Distributed Active Archive Center, accessed 20 March 2026, https://doi.org/10.5067/MODIS/MOD13A1.061.

——, 2021b: MODIS/Aqua vegetation indices 16-day L3 global 500m SIN grid V061. NASA EOSDIS Land Processes Distributed Active Archive Center, accessed 20 March 2026, https://doi.org/10.5067/MODIS/MYD13A1.061.

Dou, T. F., S. F. Pan, R. Bintanja, and C. D. Xiao, 2022: More frequent, intense, and extensive rainfall events in a strongly warming Arctic. *Earth's Future*, **10**, e2021EF002378, https://doi.org/10.1029/2021ef002378.

England, M. R., L. M. Polvani, J. Screen, and A. C. Chan, 2025: Minimal Arctic sea ice loss in the last 20 years, consistent with internal climate variability. *Geophys. Res. Lett.*, **52**, e2025GL116175, https://doi.org/10.1029/2025GL116175.

ESA, 2023: SMOS-CryoSat L4 sea ice thickness, version 206. ESA, accessed 1 September 2025, https://doi.org/10.57780/sm1-4f787c3.

ESRI, 2026: World Continents. Environmental Systems Research Institute, https://hub.arcgis.com/datasets/esri::world-continents/about.

Falvo, G., and Coauthors, 2025: Record 2024 winter carbon emissions coincide with record warmth across boreal forest, tundra, and wetland ecosystems. *Environ. Res. Lett.*, **20**, 114032, https://doi.org/10.1088/1748-9326/ae09bb.

——, and Coauthors, 2026: Reporting 2025 ecosystem CO_2 and CH_4 fluxes with near real-time data during back-to-back record warm Arctic-boreal winters. *Environ. Res. Lett*., https://doi.org/10.1088/1748-9326/ae8711, in press.

Fausto, R. S., and Coauthors, 2021: Programme for monitoring of the Greenland ice sheet (PROMICE) automatic weather station data. *Earth Syst. Sci. Data*, **13**, 3819–3845, https://doi.org/10.5194/essd-13-3819-2021.

Ferraro, A. J., M. Collins, and F. H. Lambert, 2015: A hiatus in the stratosphere? *Nat. Climate Change*, **5**, 497–498, https://doi.org/10.1038/nclimate2624.

Fetterer, F., K. Knowles, W. N. Meier, M. Savoie, and A. K. Windnagel, 2025: Sea Ice Index, Version 4 (updated daily). National Snow and Ice Data Center, accessed 2 October 2025, https://doi.org/10.7265/a98x-0f50.

Fettweis, X., and Coauthors, 2020: GrSMBMIP: intercomparison of the modelled 1980–2012 surface mass balance over the Greenland Ice Sheet. *Cryosphere*, **14**, 3935–3958, https://doi.org/10.5194/tc-14-3935-2020.

Fox, S., A. Crawford, M. McCrystall, J. Stroeve, J. Lukovich, N. Loeb, J. Natanine, and M. Serreze, 2023: Extreme Arctic weather and community impacts in Nunavut: A case study of one winter's storms and lessons for local climate change preparedness. *Wea. Climate Soc.*, **15**, 881–892, https://doi.org/10.1175/WCAS-D-23-0006.1.

Frost, G. V., and Coauthors, 2025a: Tundra greenness. NOAA Tech. Rep. OAR ARC 25-09, 9 pp., https://doi.org/10.25923/0k84-kn78.

——, and Coauthors, 2025b: The changing face of the Arctic: Four decades of greening and implications for tundra ecosystems. *Front. Environ. Sci.*, **13**, 1525574, https://doi.org/10.3389/fenvs.2025.1525574.

GMAO, 2015: MERRA-2tavg1_2d_lnd_Nx:2d, 1-hourly, time-averaged, single-level, assimilation, land surface diagnostics V5.12.4. Goddard Earth Sciences Data and Information Services Center, accessed 13 August 2025, https://doi.org/10.5067/RKPHT8KC1Y1T.

Hansen, B. B., and Coauthors, 2014: Warmer and wetter winters: Characteristics and implications of an extreme weather event in the high Arctic. *Environ. Res. Lett.*, **9**, 114021, https://doi.org/10.1088/1748-9326/9/11/114021.

Hersbach, H., and Coauthors, 2020: The ERA5 global reanalysis. *Quart. J. Roy. Meteor. Soc.*, **146**, 1999–2049, https://doi.org/10.1002/qj.3803.

Hjort, J., D. Streletskiy, G. Doré, Q. Wu, K. Bjella, and M. Luoto, 2022: Impacts of permafrost degradation on infrastructure. *Nat. Rev. Earth Environ.*, **3**, 24–38, https://doi.org/10.1038/s43017-021-00247-8.

Huang, B., C. Liu, V. Banzon, E. Freeman, G. Graham, B. Hankins, T. Smith, and H.-M. Zhang, 2021: Improvements of the Daily Optimum Interpolation Sea Surface Temperature (DOISST) version 2.1. *J. Climate*, **34**, 2923–2939, https://doi.org/10.1175/JCLI-D-20-0166.1.

Irrgang, A., and Coauthors, 2025: Measurement of permafrost. *Measurement of Cryospheric Variables*, Vol. 2, Guide to Instruments and Methods of Observation, WMO, 99–148, https://doi.org/10.59327/wmo/cimo/2.

Isaksen, K., J. Lutz, A. M. Sorensen, O. Godoy, L. Ferrighi, S. Eastwood, and S. Aaboe, 2022: Advances in operational permafrost monitoring on Svalbard and in Norway. *Environ. Res. Lett.*, **17**, 095012, https://doi.org/10.1088/1748-9326/ac8e1c.

Ivanova, N., O. M. Johannessen, L. T. Pedersen and R. T. Tonboe, 2014: Retrieval of Arctic sea ice parameters by satellite passive microwave sensors: A comparison of eleven sea ice concentration algorithms. *IEEE Trans. Geosci. and Rem. Sens.*, **52** (11), 7233-7246, https://doi.org/10.1109/TGRS.2014.2310136.

Jóhannesson, T., H. Björnsson, E. Magnússon, S. Guðmundsson, F. Pálsson, O. Sigurðsson, T. Thorsteinsson, and E. Berthier, 2013: Ice-volume changes, bias estimation of mass-balance measurements and changes in subglacial lakes derived by lidar mapping of the surface of Icelandic glaciers. *Ann. Glaciol.*, **54**, 63–74, https://doi.org/10.3189/2013AoG63A422.

Jones, H. G., J. W. Pomeroy, D. A. Walker, and R. W. Hoham, 2011: Snow ecology: An interdisciplinary examination of snow-covered ecosystems. Cambridge University Press, 400 pp., https://books.google.ca/books?id=7LhicgAACAAJ.

Karlsson, N. B., and Coauthors, 2021: A first constraint on basal melt-water production of the Greenland ice sheet. *Nat. Commun.*, **12**, 3461, https://doi.org/10.1038/s41467-021-23739-z.

Kienholz, C., and Coauthors, 2020: Deglacierization of a marginal basin and implications for outburst floods, Mendenhall Glacier, Alaska. *Front. Earth Sci.*, **8**, 137, https://doi.org/10.3389/feart.2020.00137.

Kjøllmoen, B., Ed., L. M. Andreassen, and H. Elvehøy, 2025: Glaciological investigations in Norway 2024, NVE Rapport 27-2025, 110 pp +app, Norwegian Water resources and Energy Directorate, Oslo, https://publikasjoner.nve.no/rapport/2025/rapport2025_27.pdf.

Kuhn, M., and Coauthors, 2025: Current and future methane emissions from boreal-Arctic wetlands and lakes. *Nat. Climate Change*, **15**, 986–991, https://doi.org/10.1038/s41558-025-02413-y.

Landerer, F. W., and Coauthors, 2020: Extending the global mass change data record: GRACE follow-on instrument and science data performance. *Geophys. Res. Lett.*, **47**, e2020GL088306, https://doi.org/10.1029/2020GL088306.

Lavergne, T., and Coauthors, 2019: Version 2 of the EUMETSAT OSI SAF and ESA CCI sea-ice concentration climate data records. *Cryosphere*, **13**, 49–78, https://doi.org/10.5194/tc-13-49-2019.

Lechler, L., Å. Ø. Pedersen, I. H. Myers-Smith, M. Le Moullec, L. E. Loe, B. B. Hansen, L. T. Beumer, and V. Ravolainen, 2025: Basal ice but not summer temperature affects land surface greenness in parts of the landscape in high Arctic tundra. *Environ. Res. Lett.*, **20**, 124058, https://doi.org/10.1088/1748-9326/ae2141.

Lenssen, N., G. Schmidt, J. Hansen, M. Menne, A. Persin, R. Ruedy, and D. Zyss, 2019: Improvements in the GISTEMP uncertainty model. *J. Geophys. Res. Atmos.*, **124**, 6307–6326, https://doi.org/10.1029/2018JD029522.

Lindgren, A., G. Hugelius, and P. Kuhry, 2018: Extensive loss of past permafrost carbon but a net accumulation into present-day soils. *Nature*, **560**, 219–222, https://doi.org/10.1038/s41586-018-0371-0.

Loeb, N. A., A. Crawford, J. C. Stroeve, and J. Hanesiak, 2022: Extreme precipitation in the eastern Canadian Arctic and Greenland: An evaluation of atmospheric reanalyses. *Front. Environ. Sci.*, **10**, 866929, https://doi.org/10.3389/fenvs.2022.866929.

Luojus, K., and Coauthors, 2022: ESA Snow Climate Change Initiative (Snow_cci): Snow Water Equivalent (SWE) level 3C daily global climate research data package (CRDP) (1979–2020), version 2.0. NERC EDS Centre for Environmental Data Analysis, accessed 13 August 2025, https://doi.org/10.5285/4647cc9ad3c044439d6c643208d3c494.

Mankoff, K. D., A. Solgaard, W. Colgan, A. P. Ahlstrøm, S. A. Khan, and R. S. Fausto, 2020: Greenland ice sheet solid ice discharge from 1986 through March 2020. *Earth Syst. Sci. Data*, **12**, 1367–1383, https://doi.org/10.5194/essd-12-1367-2020.

——, and Coauthors, 2021: Greenland ice sheet mass balance from 1840 through next week. *Earth Syst. Sci. Data*, **13**, 5001–5025, https://doi.org/10.5194/essd-13-5001-2021.

Medley, B., T. A. Neumann, H. J. Zwally, B. E. Smith, and C. M. Stevens, 2022: Simulations of firn processes over the Greenland and Antarctic ice sheets: 1980–2021. *Cryosphere*, **16**, 3971–4011, https://doi.org/10.5194/tc-16-3971-2022.

Meier, W. N., F. Fetterer, A. K. Windnagel, J. S. Stewart, and T. Stafford, 2026a: Near-real-time NOAA/NSIDC climate data record of passive microwave sea ice concentration (G10016, Version 4). National Snow and Ice Data Center, accessed 6 February 2026, https://doi.org/10.7265/tm2n-1m33.
——, ——, ——, ——, and ——, 2026b: NOAA/NSIDC climate data record of passive microwave sea ice concentration (G02202, Version 6). National Snow and Ice Data Center, accessed 6 February 2026, https://doi.org/10.7265/b18j-z797.
Mekonnen, Z. A., and Coauthors, 2021: Arctic tundra shrubification: A review of mechanisms and impacts on ecosystem carbon balance. *Environ. Res. Lett.*, **16**, 053001, https://doi.org/10.1088/1748-9326/abf28b.
Meng, J., J. Fan, U. S. Bhatt, and J. Kurths, 2023: Arctic weather variability and connectivity. *Nat. Commun.*, **14**, 6574, https://doi.org/10.1038/s41467-023-42351-x.
Meredith, M., and Coauthors, 2019: Polar regions. *The Ocean and Cryosphere in a Changing Climat*e, H.-O. Pörtner et al., Cambridge University Press, 203–320, https://doi.org/10.1017/9781009157964.005.
Miner, K. R., and Coauthors, 2022: Permafrost carbon emissions in a changing Arctic. *Nat. Rev. Earth Environ.*, **3**, 55–67, https://doi.org/10.1038/s43017-021-00230-3.
Moon, T. A., and Coauthors, 2019: The expanding footprint of rapid Arctic change. *Earth's Future*, **7**, 212–218, https://doi.org/10.1029/2018EF001088.
Mote, T., 2007: Greenland surface melt trends 1973–2007: Evidence of a large increase in 2007. *Geophys. Res. Lett.*, **34**, L22507, https://doi.org/10.1029/2007GL031976.
Mouginot, J., and Coauthors, 2019: Forty-six years of Greenland ice sheet mass balance from 1972 to 2018. *Proc. Natl. Acad. Sci. USA*, **116**, 9239–9244, https://doi.org/10.1073/pnas.1904242116.
Mudryk, L. R., A. Elias Chereque, C. Derksen, K. Luojus, and B. Decharme, 2025: Terrestrial snow cover. NOAA Tech. Rep. OAR ARC 25-04, 8 pp., https://doi.org/10.25923/cfhv-c239.
Muñoz Sabater, J., 2019: ERA5-Land hourly data from 1950 to present. Copernicus Climate Change Service Climate Data Store, accessed 18 July 2025, https://doi.org/10.24381/cds.e2161bac.
Natali, S. M., J. P. Holdren, B. M. Rogers, R. Treharne, P. B. Duffy, R. Pomerance, and E. MacDonald, 2021: Permafrost carbon feedbacks threaten global climate goals. *Proc. Natl. Acad. Sci. USA*, **118**, e2100163118, https://doi.org/10.1073/pnas.2100163118.
——, and Coauthors, 2024: Arctic terrestrial carbon cycling. NOAA Tech. Rep. OAR ARC 24-11, 8 pp., https://doi.org/10.25923/0gpp-mn10.
Nyland, K. E., N. I. Shiklomanov, D. A. Streletskiy, F. E. Nelson, A. E. Klene, and A. L. Kholodov, 2021: Long-term Circumpolar Active Layer Monitoring (CALM) program observations in northern Alaskan tundra. *Polar Geogr.*, **44**, 167–185, https://doi.org/10.1080/1088937X.2021.1988000.
O'Neill, H. B., S. L. Smith, C. R. Burn, C. Duchesne, and Y. Zhang, 2023: Widespread permafrost degradation and thaw subsidence in Northwest Canada. *J. Geophys. Res. Earth Surf.*, **128**, e2023JF007262, https://doi.org/10.1029/2023JF007262.
Parmentier, F.-J. W., B. F. Thornton, A. Silyakova, and T. R. Christensen, 2024: Vulnerability of Arctic-boreal methane emissions to climate change. *Front. Environ. Sci.*, **12**, 1460155, https://doi.org/10.3389/fenvs.2024.1460155.
Phoenix, G. K., and Coauthors, 2025: Browning events in Arctic ecosystems: Diverse causes with common consequences. *PLOS Climate*, **4**, e0000570, https://doi.org/10.1371/journal.pclm.0000570.
Pinzon, J. E., C. J. Tucker, U. S. Bhatt, G. V. Frost, and M. J. Macander, 2023: Global Vegetation Greenness (NDVI) from AVHRR GIMMS-3G+, 1981-2022. ORNL DAAC, accessed 31 March 2026, https://doi.org/10.3334/ORNLDAAC/2187.
Polyakov, I. V., and Coauthors, 2025: Atlantification advances into the Amerasian Basin of the Arctic Ocean. *Sci. Adv.*, **11**, eadq7580, https://doi.org/10.1126/sciadv.adq7580.
Ramage, J., and Coauthors, 2024: The net GHG balance and budget of the permafrost region (2000–2020) from ecosystem flux upscaling. *Global Biogeochem. Cycles*, **38**, e2023GB007953, https://doi.org/10.1029/2023GB007953.
Rantanen, M., A. Y. Karpechko, A. Lipponen, K. Nordling, O. Hyvärinen, K. Ruosteenoja, T. Vihma, and A. Laaksonen, 2022: The Arctic has warmed nearly four times faster than the globe since 1979. *Commun. Earth Environ.*, **3**, 168, https://doi.org/10.1038/s43247-022-00498-3.
Raynolds, M. K., and Coauthors, 2019: A raster version of the Circumpolar Arctic Vegetation Map (CAVM). *Remote Sens. Environ.*, **232**, 111297, https://doi.org/10.1016/j.rse.2019.111297.
RGI Consortium, 2023: Randolph Glacier Inventory - A dataset of global glacier outlines (NSIDC-0770, Version 7). National Snow and Ice Data Center, accessed 11 August 2023, https://doi.org/10.5067/f6jmovy5navz.
Ricker, R., S. Hendricks, L. Kaleschke, X. Tian-Kunze, J. King, and C. Haas, 2017: A weekly Arctic sea-ice thickness data record from merged CryoSat-2 and SMOS satellite data. *Cryosphere*, **11**, 1607–1623, https://doi.org/10.5194/tc-11-1607-2017.
Rivière, G., F. D'Andrea, D. I. V. Domeisen, and A. Portal, 2024: Opposite trends in the Northern Hemisphere stratosphere between mid?winter and early spring linked to surface temperature anomalies. *Geophys. Res. Lett.*, **51**, e2024GL109746, https://doi.org/10.1029/2024GL109746.
Robinson, D. A., T. W. Estilow, and NOAA CDR Program, 2012: NOAA Climate Data Record (CDR) of Northern Hemisphere (NH) Snow Cover Extent (SCE), Version 1 [r01]. NOAA National Centers for Environmental Information, accessed 12 August 2025, https://doi.org/10.7289/V5N014G9.
Román, M. O., and Coauthors, 2024: Continuity between NASA MODIS Collection 6.1 and VIIRS Collection 2 land products. *Remote Sens. Environ.*, **302**, 113963, https://doi.org/10.1016/j.rse.2023.113963.
Romanovsky, V. E., and Coauthors, 2017: Changing permafrost and its impacts. Snow, Water, Ice and Permafrost in the Arctic (SWIPA) 2017, Arctic Monitoring and Assessment Program, 65–102, https://www.amap.no/documents/doc/snow-water-ice-and-permafrost-in-the-arctic-swipa-2017/1610.
Santer, B. D., and Coauthors, 2023: Exceptional stratospheric contribution to human fingerprints on atmospheric temperature. *Proc. Natl. Acad. Sci. USA*, **120**, e2300758120, https://doi.org/10.1073/pnas.2300758120.
Saunois, M., and Coauthors, 2025: Global methane budget 2000–2020. *Earth Syst. Sci. Data*, **17**, 1873–1958, https://doi.org/10.5194/essd-17-1873-2025.
Schneider, U., P. Finger, E. Rustemeier, M. Ziese, and S. Hänsel, 2022: Global precipitation analysis products of the GPCC. Global Precipitation Climatology Centre, 17 pp., https://opendata.dwd.de/climate_environment/GPCC/PDF/GPCC_intro_products_v2022.pdf.

Schuler, T. V., R. E. Benestad, K. Isaksen, H. P. Kierulf, J. Kohler, G. Moholdt, and L. S. Schmidt, 2025: Svalbard's 2024 record summer: An early view of Arctic glacier meltdown? *Proc. Natl. Acad. Sci. USA*, **122**, e2503806122, https://doi.org/10.1073/pnas.2503806122.

Schuur, E. A. G., and Coauthors, 2015: Climate change and the permafrost carbon feedback. *Nature*, **520**, 171–179, https://doi.org/10.1038/nature14338.

——, and Coauthors, 2022: Permafrost and climate change: Carbon cycle feedbacks from the warming Arctic. *Annu. Rev. Environ. Resour.*, **47**, 343–371, https://doi.org/10.1146/annurev-environ-012220-011847.

——, C. Hicks Pries, M. Mauritz, E. Pegoraro, H. Rodenhizer, C. See, and C. Ebert, 2023: Ecosystem and soil respiration radiocarbon detects old carbon release as a fingerprint of warming and permafrost destabilization with climate change. *Philos. Trans. Roy. Soc.*, **A381**, 20220201, https://doi.org/10.1098/rsta.2022.0201.

See, C. R., and Coauthors, 2024: Decadal increases in carbon uptake offset by respiratory losses across northern permafrost ecosystems. *Nat. Climate Change*, **14**, 853–862, https://doi.org/10.1038/s41558-024-02057-4.

Serreze, M. C., and Coauthors, 2021: Arctic rain on snow events: Bridging observations to understand environmental and livelihood impacts. *Environ. Res. Lett.*, **16**, 105009, https://doi.org/10.1088/1748-9326/ac269b.

——., E. Cassano, A. Crawford, J. J. Cassano, and C. Zhang, 2026: The observed evolution of Arctic amplification over the past 45 years. *Cryosphere*, **20**, 411–425, https://doi.org/10.5194/tc-20-411-2026.

——, M. P. Clark, and D. H. Bromwich, 2003: Monitoring precipitation over the Arctic terrestrial drainage system: Data requirements, shortcomings, and applications of atmospheric reanalysis. *J. Hydrometeor.*, **4**, 387–407, https://doi.org/10.1175/1525-7541(2003)4<387:MPOTAT>2.0.CO;2.

Smith, B., 2023: Algorithm Theoretical Basis Document (ATBD) for Land-ice DEM (ATL14) and Land-ice height change (ATL15). Algorithm Theoretical Basis Doc., 71 pp., https://nsidc.org/sites/default/files/documents/technical-reference/icesat2_atl14_atl15_atbd_v003.pdf.

——, S. Dickinson, B. P. Jelley, T. A. Neumann, D. Hancock, J. Lee, and K. Harbeck, 2023: ATLAS/ICESat-2 L3B slope-corrected land ice height time series, Version 6. NASA National Snow and Ice Data Center Distributed Active Archive Center, accessed 25 January 2025, https://doi.org/10.5067/ATLAS/ATL11.006.

Smith, S. L., H. B. O'Neill, K. Isaksen, J. Noetzli, and V. E. Romanovsky, 2022: The changing thermal state of permafrost. *Nat. Rev. Earth Environ.*, **3**, 10–23, https://doi.org/10.1038/s43017-021-00240-1.

——, C. Duchesne, and H. B. O'Neill, 2024: Long-term permafrost monitoring in northern Canada – What have we learned? *12th Int. Conf. on Permafrost*, Whitehorse, YT, Canada, International Permafrost Association, 398–404, https://doi.org/10.52381/ICOP2024.84.1.

——, V. E. Romanovsky, K. Isaksen, K. E. Nyland, K. I. Shiklomanov, D. A. Streletskiy, and H. H. Christiansen, 2025: Permafrost [in "State of the Climate in 2024"]. *Bull. Amer. Meteor. Soc.*, **106** (8), S338–S341, https://doi.org/10.1175/BAMS-D-25-0104.1.

Streletskiy, D. A., and Coauthors, 2025: Thawing permafrost is subsiding in the Northern Hemisphere—Review and perspectives. *Environ. Res. Lett.*, **20**, 013006, https://doi.org/10.1088/1748-9326/ada2ff.

Stroeve, J. C., D. Notz, J. Dawson, E. A. G. Schuur, D. Dahl-Jensen, and C. Giesse, 2025: Disappearing landscapes: The Arctic at +2.7°C global warming. *Science*, **387**, 616–621, https://doi.org/10.1126/science.ads1549.

Sweeney, A. J., Q. Fu, S. Po-Chedley, H. Wang, and M. Wang, 2023: Internal variability increased Arctic amplification during 1980–2022. *Geophys. Res. Lett.*, **50**, e2023GL106060, https://doi.org/10.1029/2023GL106060.

Tapley, B. D., and Coauthors, 2019: Contributions of GRACE to understanding climate change. *Nat. Climate Change*, **5**, 358–369, https://doi.org/10.1038/s41558-019-0456-2.

The GlaMBIE Team, 2025: Community estimate of global glacier mass changes from 2000 to 2023. *Nature*, **639**, 382–388, https://doi.org/10.1038/s41586-024-08545-z.

Thoman, R., and H. R. McFarland, Eds., 2024: Alaska's Changing Environment 2.0. Alaska Center for Climate Assessment and Policy, International Arctic Research Center, University of Alaska Fairbanks, 32 pp., https://uaf-iarc.org/communicating-change.

Tschudi, M., W. N. Meier, J. S. Stewart, C. Fowler, and J. Maslanik, 2019a: EASE-grid sea ice age, Version 4. NASA National Snow and Ice Data Center Distributed Active Archive Center, accessed 5 September 2025, https://doi.org/10.5067/UTAV7490FEPB.

——, ——, and ——, 2019b: Quicklook Arctic weekly EASE-grid sea ice age, Version 1. NASA National Snow and Ice Data Center Distributed Active Archive Center, accessed 2 October 2025, https://doi.org/10.5067/2XXGZY3DUGNQ.

U.S. Geological Survey, 2025: 2025 Tracy Arm landslide-generated tsunami. U.S. Geological Survey, Landslide Hazards Program, accessed 14 August 2025, https://www.usgs.gov/programs/landslide-hazards/science/2025-tracy-arm-landslide-generated-tsunami#overview.

U.S. National Ice Center, 2008: IMS Daily Northern Hemisphere snow and ice analysis at 1 km, 4 km, and 24 km resolutions, Version 1. National Snow and Ice Data Center, accessed 31 January 2026, https://doi.org/10.7265/N52R3PMC.

Virkkala, A.-M., and Coauthors, 2025: Wildfires offset the increasing but spatially heterogeneous Arctic–boreal CO_2 uptake. *Nat. Climate Change*, **15**, 188–195, https://doi.org/10.1038/s41558-024-02234-5.

Vogt, J., and Coauthors, 2025: ARGO: ARctic greenhouse gas observation metadata version 1. *Earth Syst. Sci. Data*, **17**, 2553–2573, https://doi.org/10.5194/essd-17-2553-2025.

Wallenius, T., and Coauthors, 2025: Reconstructing the historical decline of lichen cover across the reindeer fence of the Finnish-Norwegian border. *Ambio*, **54**, 1683–1704, https://doi.org/10.1007/s13280-025-02171-3.

Walsh, J. E., T. J. Ballinger, E. S. Euskirchen, E. Hanna, J. Mård, J. E. Overland, H. Tangen, and T. Vihma, 2020: Extreme weather and climate events in northern areas: A review. *Earth Sci. Rev.*, **209**, 103324, https://doi.org/10.1016/j.earscirev.2020.103324.

——, S. Bigalke, S. A. McAfee, R. Lader, M. C. Serreze, and T. J. Ballinger, 2022: Precipitation. NOAA Tech. Rep. OAR ARC 22-03, 8 pp., https://doi.org/10.25923/yxs5-6c72.

Watkins, M. M., D. N. Wiese, D.-N. Yuan, C. Boening, and F. W. Landerer, 2015: Improved methods for observing Earth's time variable mass distribution with GRACE using spherical cap mascons. *J. Geophys. Res. Solid Earth*, **120**, 2648–2671, https://doi.org/10.1002/2014JB011547.

Weber, M., and Coauthors, 2022: Global total ozone recovery trends attributed to ozone-depleting substance (ODS) changes derived from five merged ozone datasets. *Atmos. Chem. Phys.*, **22**, 6843–6859, https://doi.org/10.5194/acp-22-6843-2022.

WGMS, 2025: Fluctuations of glaciers database. World Glacier Monitoring Service, accessed 3 June 2026, https://doi.org/10.5904/wgms-fog-2025-02b.

Wolken, G. J., and Coauthors, 2021: Glacier and permafrost hazards. NOAA Tech. Rep. OAR ARC 21-13, 9 pp., https://doi.org/10.25923/v40r-0956.

Wouters, B., A. Gardner, and G. Moholdt, 2019: Global glacier mass loss during the GRACE satellite mission (2002-2016). *Front. Earth Sci.*, **7**, 96, https://doi.org/10.3389/feart.2019.00096.

Ye, H., D. Yang, A. Behrangi, S. L. Stuefer, X. Pan, E. Mekis, Y. Dibike, and J. E. Walsh, 2021: Precipitation characteristics and changes. *Arctic Hydrology, Permafrost and Ecosystems*, D. Yang and D. L. Kane, Eds., Springer Nature, 25–59, https://doi.org/10.1007/978-3-030-50930-9_2.

Yu, L., and S. Zhong, 2021: Trends in Arctic seasonal and extreme precipitation in recent decades. *Theor. Appl. Climatol.*, **145**, 1541–1559, https://doi.org/10.1007/s00704-021-03717-7.

Zemp, M., and Coauthors, 2019: Global glacier mass changes and their contributions to sea-level rise from 1961 to 2016. *Nature*, **568**, 382–386, https://doi.org/10.1038/s41586-019-1071-0.

Zhou, W., L. R. Leung, and J. Lu, 2024: Steady threefold Arctic amplification of externally forced warming masked by natural variability. *Nat. Geosci.*, **17**, 508–515, https://doi.org/10.1038/s41561-024-01441-1.